STRUCTURE-BORNE ELASTIC WAVE ENERGY HARVESTING ENHANCED BY METAMATERIAL CONCEPTS

A Dissertation
Presented to
The Academic Faculty

by

Serife Tol

In Partial Fulfillment
of the Requirements for the Degree
Doctor of Philosophy in the
George W. Woodruff School of Mechanical Engineering

Georgia Institute of Technology
August 2017

STRUCTURE-BORNE ELASTIC WAVE ENERGY HARVESTING ENHANCED BY METAMATERIAL CONCEPTS

Approved by:

Dr. Alper Erturk, Advisor
School of Mechanical Engineering
Georgia Institute of Technology

Dr. F. Levent Degertekin, Advisor
School of Mechanical Engineering
Georgia Institute of Technology

Dr. Karim Sabra
School of Mechanical Engineering
Georgia Institute of Technology

Dr. Massimo Ruzzene
School of Aerospace Engineering
School of Mechanical Engineering
Georgia Institute of Technology

Dr. Min-Feng Yu
School of Aerospace Engineering
Georgia Institute of Technology

Date Approved: May 1, 2017

To Evren.

ACKNOWLEDGEMENTS

Contents

List of Figures

SUMMARY

Existing research on vibration-based energy harvesting has been mainly focused on the harvesting of deterministic or stochastic vibrational energy available at a fixed position in space. Such an approach is convenient for designing and employing linear and nonlinear vibration-based energy harvesters, such as base-excited cantilevers with piezoelectric laminates undergoing persistent excitation that yield modal vibrations. This theoretical and experimental research is centered on the harvesting of structure-borne propagating elastic waves in one-dimensional and two-dimensional settings, i.e. beam and plate configurations, respectively. Specifically, it is aimed to enhance the harvested elastic wave energy by exploiting concepts from metamaterials and phononic crystals. In the first part of this research, the focus is placed on a one-dimensional beam configuration for piezoelectric energy harvesting from bending waves through optimal resistive-reactive electrical loading, spatially localized obstacle for harvesting local reflections, and a multifunctional energy-harvesting electromechanical non-reflective boundary condition in a semi-infinite setting. Then, two-dimensional wave energy harvesting concepts are explored with an emphasis on wave focusing by tailoring reflection and refraction properties of elastic plates through elastic wave mirror and elastic wave lens concepts. Wave focusing is first studied thoroughly using mirror concepts (parabolic mirror for plane waves and elliptical mirror for point sources) with a focus on the design methodology and scattering characteristics. In this context, structurally embedded mirrors (SEM) and bandgap based mirrors are presented. As an alternative approach, the elastic wave lenses are designed by creating a gradient distribution of the refractive index of the phononic crystals (PC) and locally resonant (LR) unit cells to focus elastic plane waves that are in the form of the lowest asymmetric Lamb wave mode in the elastic plate. To this end, a Gradient-Index Phononic Crystal Lens (GRIN-PCL), a 3D printed GRIN-PCL, and an omnidirectional Luneburg lens are fabricated and experimentally validated for wave focusing and enhanced energy harvesting. In addition, wave focusing is explored

with GRIN lenses composed of locally resonant unit cells which is especially important for enabling enhanced energy harvesting in the low frequency range. Overall this work provides electroelastic models and novel approaches to efficient elastic wave energy harvesting in one-dimensional and two-dimensional structures. Beyond enhanced energy harvesting, ramifications of this work range from MEMS implementation to 3D printed platforms for structural integration in sensing applications and nondestructive testing.

This dissertation is outlined as follows: Chapter 1 provides an introduction into elastic wave energy harvesting via piezoelectric transduction and metamaterial concepts employed to focus elastic waves for enhanced energy harvesting. Chapter 2 focuses on the electroelastic modeling and validation of flexural (bending) wave energy harvesting in beams. Chapter 3 details design, analysis, and experimental validation of elastic wave mirrors for wave focusing and enhanced energy harvesting. Chapter 4 presents design and validation of elastic lens concepts with gradient index phononic crystal theory. Chapter 5 explores wave focusing with lens and bandgap-based mirrors composed of locally resonant unit cells. Chapter 6 concludes this dissertation by summarizing the contributions made to the field of structure-borne elastic wave energy harvesting with a focus on metamaterial concepts and opportunities for further work. A derivation of the equivalent representation for one-dimensional wave harvesting is included in Appendix A.

Chapter I

INTRODUCTION

1.1 Structure-Borne Elastic Wave Energy Harvesting via Piezoelectric Transduction

Over the last decade, several research groups have worked on energy harvesting with the motivation of powering small electronic components by scavenging ambient energy available in their environment. Ambient energy exists in various forms, such as waste heat, solar, vibration, and flow energy. While each of these sources of energy can be used to power small electronic devices, the harvesting of vibrational energy has been mostly studied as a viable alternative source [4, 81, 69, 50, 23, 68]. Various methods of vibration/motion energy harvesting have been researched toward enabling next-generation self-powered electronic devices for wireless applications ranging from structural health monitoring to wearable electronic components [73, 25, 21]. The energy conversion methods that have been used for transforming mechanical (mostly vibrational and kinetic) energy into electricity are the piezoelectric [73, 25], electromagnetic [97, 32], electrostatic [60, 94], and magnetostrictive [95] conversion techniques, as well as the use of electroactive polymers and ionic polymer-metal composites [84, 6]. Among these alternatives, piezoelectric transduction has received arguably the greatest attention due to the high power density and ease of application piezoelectric materials, and their relatively mature fabrication techniques at different geometric scales [16].

The harvesting of standing waves and vibrations has been extensively researched through the use of linear and nonlinear energy harvesters, such as cantilevers with piezoelectric layers undergoing base excitation illustrated in Figure 1. An alternating voltage output is obtained in response to vibration of the harvester, and maximum power is generated typically at the fundamental resonant frequency of the composite structure [22]. Although it is common practice to characterize the resonance behavior of a piezoelectric energy harvester with harmonic excitation, different models may be required for other loading conditions,
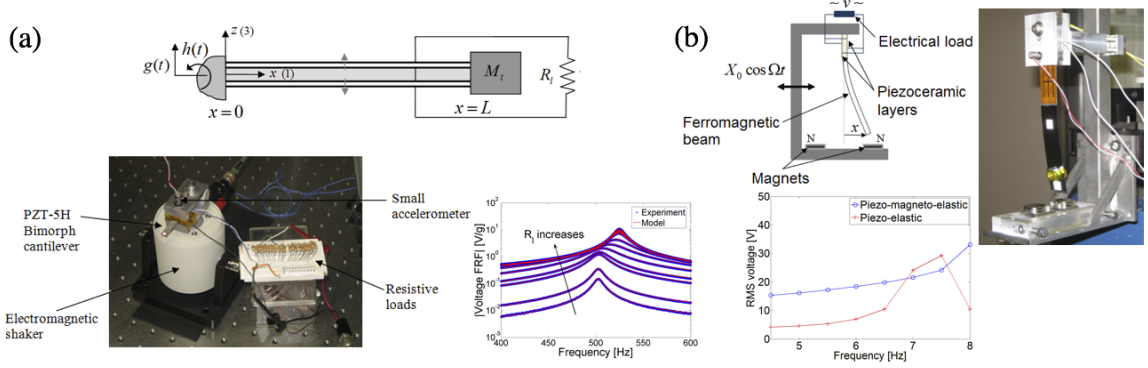
Figure 1: Vibration-based piezoelectric energy harvesters (a) Linear bimorph [22] and (b) Nonlinear bimorph [25].

especially in the absence of standing waves. For instance, scavenging energy from vibrations due to fluid-structure interaction requires a more complex analysis because of the coupling of piezoelastic structure with the surrounding airstream [25]. In the existing literature, flow energy harvesting through aeroelastic [7, 8, 19, 20, 26, 45, 17, 1] and hydroelastic [2, 64, 24] vibrations has been studied. However, the available energy of waves traveling in fluids and structures, i.e. propagating acoustic and elastic waves, and the overall wave propagation approach to energy harvesting problem has received much less attention, yielding rather limited literature. Few research groups have studied this area with a focus on polarization-patterned piezoelectric solids [74], quarter-wavelength resonators [47], Helmholtz resonators [37, 51, 13, 102], phononic crystals [13, 33, 96, 98], or elastic mirrors [9, 10].

On the other hand, various researchers combined the wave propagation theory with the piezoelectric sensing/actuating mechanisms to study passive and active structural health monitoring (SHM) systems [67, 14, 29, 62]. For instance, the electromechanical impedance technique for SHM utilizes travelling waves and the electrical impedance of a surface-bonded PZT transducer to obtain the change in the electromechanical impedance signature of the structure and detects the structural damage by monitoring this change [48, 30, 63, 80]. In various SHM applications, researchers utilized ultrasonic waves such as Rayleigh surface waves and Lamb modes [67, 31, 28]. In these studies, the focus has been either only on the forward problem to excite these waves more efficiently, or to sense with small size piezo patches where the important factor is signal to noise, not efficiency of energy transfer. In

those cases, for example, the effect of piezo patch electrical impedance and load termination on the propagating wave amplitudes through backward coupling are not considered. Hence, this work aims to fill in these gaps in literature by developing a fully coupled electroelastic model for harvesting propagating wave energy via piezoelectric transduction which can also find applications in the broad area of SHM.

1.2   *Metamaterial Enhanced Energy Harvesting Concepts*

Wave propagation approach to energy harvesting enables the possibility of extracting the maximum electrical power in propagating wave scenarios including transient excitations and offers an insight that is otherwise not easily available in standing wave or modal vibration methods [87]. Importantly, to improve the efficiency of electrical power generation it is required to develop proper strategies for spatial localization or focusing wave energy through the use of local obstacles [87] as well as concepts from metamaterials and phononic crystals [12, 102, 66, 10]. In this context, recently, elastic mirror designs [9, 10, 11] have been implemented for focusing and enhanced harvesting of structure-borne elastic waves (namely the lowest asymmetric Lamb wave mode). Specifically, the elastic mirrors employed in the first-generation configurations [9, 10, 11] as shown in Figure 2 were not only heuristic, but also their bulky stub extensions that form the mirror may not be applicable in many scenarios that require preserving the flat host structure. Furthermore, it was observed that the side lobes near the geometric focal spot contained significant energy levels. Consequently, patterned segmentation of the piezoelectric domain was employed [11] through a wavenumber transformation procedure to harvest the energy at the side lobes. One of the objective of this research is to design novel elastic mirrors which eliminates bulky stub extensions while preserving good reflection capability and to increase the performance of the mirrors by reducing the side lobes of the focus with proper design methodologies.

As an alternative approach, the harvested energy can also be enhanced by designing acoustic metamaterials which focus or properly localize the wave energy by tailoring wave propagation characteristics. Relatively few research efforts have explored energy harvesting with the use of phononic crystals [54, 96, 98, 33, 13] and locally resonant metamaterials
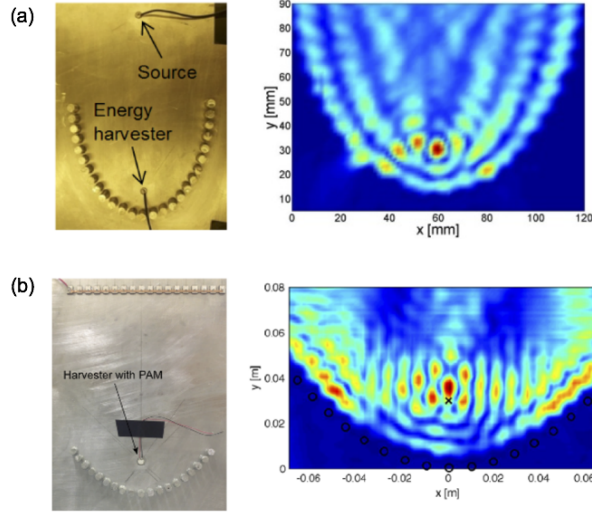
Figure 2: Wavefields exhibiting the focusing effect in the (a) elliptical elastic wave mirror [9] and (b) parabolic elastic wave mirror [10].

[58]. Growing interest has been devoted to studies on the elastic wave propagation in artificially structured materials comprising phononic crystals (PCs) inspired from their optical counterpart, photonic crystals [46]. These structures usually employ a periodic architecture of PCs with a modulation of elastic modulus and/or mass density on a scale comparable to the wavelength of elastic/acoustic waves. Due to their unique properties such as band gaps [54, 18, 79] and the ability to slow the velocity of waves [61], PC structures offer the potential for a variety of applications including vibration and noise attenuation [57, 75, 54], frequency filtering [74], subwavelength imaging [83, 104], among others. In addition, refractive acoustic devices (GRIN-PC lenses) [49, 99, 15, 103, 40] can be created by dispersion engineering to focus elastic wave energy as shown in Figure 3. These studies are mostly numerically demonstrated and outside the domain of energy harvesting literature. Hence, another objective of this research is to design and validate novel GRIN-PCL structures and couple them with piezoelectric transduction for enhanced elastic wave energy harvesting.

Similar to phononic crystals, metamaterials are periodic structures with resonant structural features which shows some novel and counterintuitive effects for wavelengths much greater than their periodicities. However, a universally accepted definition of metamaterials does not yet exist. Some researchers extend the concept of metamaterials to include
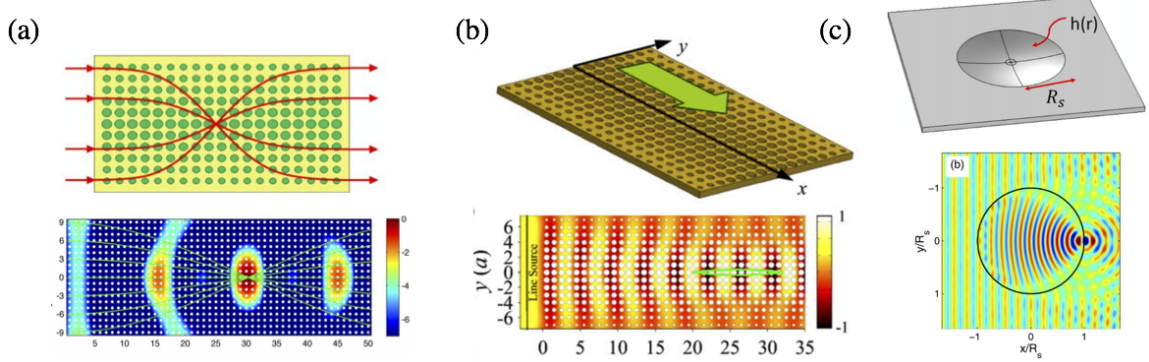
Figure 3: GRIN-PCLs designed by varying (a) stub thickness [49], (b) hole size in perforated plates [99], and (c) plate thickness locally[15].

PCs [53]. In this work, while the whole subject is covered under the metamaterial concepts, distinctions will be made clear by referring to them PC or locally resonant (LR) structures in the subsequent chapters. One distinct property between the PC and LR structures is on the formation of bandgaps which is governed by the destructive interference of the waves scattered from the periodic features of the PCs (also known as Bragg scattering [5]) and the resonance of the structural features of the LR unit cells that are coupled through the host material [38, 52], respectively as illustrated in Figure 4. In Bragg scattering, the bandgap frequency proportionally increases by shrinking the lattice constant and the geometric dimensions of the PC structure, while resonating structure determines the center frequency in LR structures [41]. Hence, in order to scale-down in the operation frequency which is essential for energy harvesting applications, LR unit cells can potentially eliminate the need to scale up the whole structure (as compared to PC structures) while providing the ability to engineer their operation frequency. This is especially important in tailoring the dispersion properties for the lens designs in low frequency applications (less than 1 kHz). In this context, designing GRIN lenses with LR unit cells towards enabling low frequency energy harvesting is another objective of this study, which has not done yet in literature. Also as another objective, the low frequency bandgap property of the LR unit cells is aimed to be employed in elastic mirror concepts to design bandgap based mirrors for focusing elastic waves in the low frequency region.
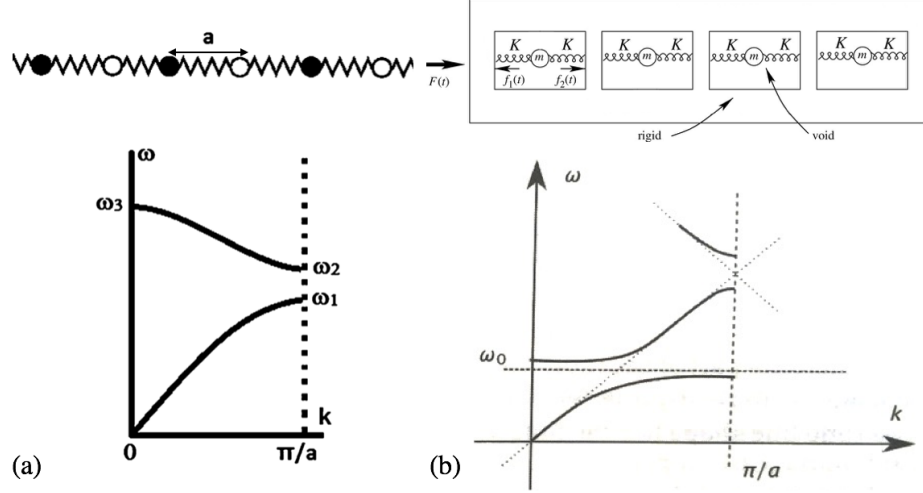
Figure 4: Periodic structures with (a) PCs [18] and (b) LR unit cells [46] and their corresponding bandgap formations.

1.3 Dissertation Outline

Having reviewed the piezoelectric energy harvesting literature from the electroelastic modeling standpoint, it is important to investigate power extraction from elastic waves propagating in host structures with a proper mathematical framework to gain a fundamental understanding of power flow and to best exploit not only standing but also traveling wave energy. The combination of the structural configurations with metamaterial concepts for elastic wave energy harvesting is essential for performance enhancement. Therefore, overall, the main goal of this dissertation is to provide electroelastic models and novel approaches to efficient elastic wave energy harvesting in one-dimensional and two-dimensional structures.

The following chapters are outlined as follows: Chapter 2 focuses on the electroelastic modeling and validation of flexural (bending) wave energy harvesting in beams. Chapter 3 details design, analysis, and experimental validation of elastic wave mirrors for wave focusing and enhanced energy harvesting. Chapter 4 presents design and validation of elastic lens concepts with gradient index phononic crystal theory. Chapter 5 explores wave focusing with lens and bandgap-based mirrors composed of locally resonant unit cells. Chapter 6 concludes this dissertation by summarizing the contributions made to the field of structure-borne elastic wave energy harvesting with a focus on metamaterial concepts and opportunities

6

for further work. A derivation of the equivalent representation for one-dimensional wave harvesting is included in Appendix A.

Chapter II

PIEZOELECTRIC POWER EXTRACTION FROM BENDING WAVES

2.1 Introduction

Existing research in the field of vibration-based energy harvesting has focused mostly on the harvesting of deterministic or stochastic vibrational energy available at a fixed position in space. Such an approach is convenient for designing and employing linear and nonlinear vibration-based energy harvesters, such as base-excited cantilevers with piezoelectric laminates. This chapter presents a mathematical framework for the harvesting of one-dimensional bending waves propagating in infinite and semi-infinite beams as an alternative [87, 90, 85]. For this purpose, electroelastic models are developed for the harvester bonded to infinite and semi-infinite beams by implementing the wave equation solution in the compatibility and equilibrium conditions at the harvester boundaries which are then solved simultaneously with the coupled electrical equation yielding the amplitudes of the traveling waves and the voltage response of the harvester. Hence, both electrical to mechanical and mechanical to electrical coupling problems are simultaneously solved. Incident wave energy is transformed into usable electricity while minimizing the traveling waves reflected and transmitted from the harvester domain. The analysis shows that the efficiency of power transfer from elastic waves can be significantly improved by wavelength matching, resistive-inductive circuits, and spatially localized obstacles. Additionally, an energy-harvesting end condition in a semi-infinite beam is introduced to minimize the reflection in the sense of creating ideally an anechoic boundary condition. The validity and application of the proposed model and the performance enhancement methods are demonstrated with several experimental studies by using piezoelectric patches bonded to a long slender beam.
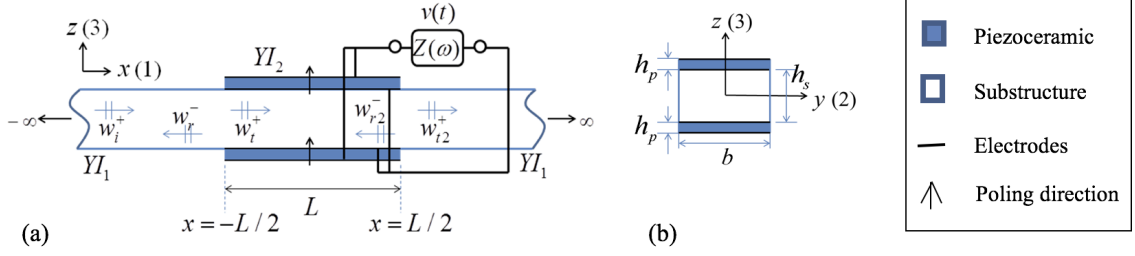
Figure 5: Incident, reflected, and transmitted waves at discontinuities: (a) Parallel connection and (b) composite cross-section in the harvester region.

2.2 Electroelastic Modeling

When a wave, propagating along a waveguide such as a beam, encounters discontinuity, it is reflected and transmitted across that discontinuity [55]. As shown in Figure 5, piezoelectric patches, symmetrically bonded to the top and bottom of a thin beam, are the sources of the discontinuity. The complex wave amplitudes are obtained by imposing the linear/angular displacement compatibility and force/moment equilibrium conditions at and solving the resulting equations simultaneously [27]. By combining the wave propagation theory with the piezoelectric energy harvester, the power flow to the electrical load through the piezoelectric patches is extracted as explained in Sections 2.2.1 and 2.2.2.

2.2.1 Bending Waves in an Infinite Euler-Bernoulli Beam

The unforced bending wave equation for one-dimensional thin beam with constant cross-sectional area can be written as

$$YI\frac{\partial^4 w(x,t)}{\partial x^4} + m\frac{\partial^2 w(x,t)}{\partial t^2} = 0 \tag{1}$$

where YI is the flexural rigidity of the beam, m is the mass per unit length, and $w(x,t)$ is the transverse displacement. This equation is based on the classical (Euler-Bernoulli) beam theory, which postulates that plane sections remain plane (by neglecting shear distortion) and also excludes the rotary inertia effects. The complete complex solution for the homogenous problem can be obtained as

$$w(x,t) = (Ae^{-jk_bx} + Be^{jk_bx} + Ce^{-k_bx} + De^{k_bx})e^{j\omega t} \tag{2}$$

9

where $k_b = (\omega^2 m/YI)^{1/4}$ is the bending wave number, ω is the frequency, and j is the unit imaginary number. The first two terms on the right-hand side of Equation 2 represent waves propagating in the positive and negative x directions at a phase velocity of $c_b = \omega/k_b$. The last two terms represent evanescent waves with exponentially decaying amplitudes with distance. Those waves do not individually transport energy, but can be effective and should be considered when the distance between discontinuities significantly smaller than the wavelength as this impacts the minimum patch size for practical optimization of power transfer.

In the energy harvesting problem, two identical piezoelectric patches of length L and thickness h_p are bonded (with a negligible bonding layer) to top and bottom surfaces of the thin beam for energy harvesting, forming a symmetric structure as shown in Figure 5. As a result, the incident wave (propagating from the left end of the beam) is scattered, generating various transmitted and reflected waves in three regions. Based on Figure 5, the incident, reflected and transmitted waves can be expressed as

$$w_i^+(x,t) = Ae^{-jk_{b1}x}e^{j\omega t}$$

$$w_r^-(x,t) = (B_1 e^{+jk_{b1}x} + B_2 e^{+k_{b1}x})e^{j\omega t}$$

$$w_t^+(x,t) = (C_1 e^{-jk_{b2}x} + C_2 e^{-k_{b2}x})e^{j\omega t}$$

$$w_r 2^-(x,t) = (D_1 e^{+jk_{b2}x} + D_2 e^{+k_{b2}x})e^{j\omega t}$$

$$w_t 2^+(x,t) = (E_1 e^{-jk_{b1}x} + E_2 e^{-k_{b1}x})e^{j\omega t} \tag{3}$$

where B_1, C_1, D_1, E_1 are the complex amplitudes of the propagating wave components while B_2, C_2, D_2, E_2 are the complex amplitudes of the evanescent counterparts, and the $+$ and x superscripts indicate propagation in the $+x$ and x directions, respectively. The shear force Q and bending moment M are

$$Q(x,t) = -YI\frac{\partial^3 w(x,t)}{\partial x^3} \quad M(x,t) = -YI\frac{\partial^2 w(x,t)}{\partial x^2} \tag{4}$$

The complex wave amplitudes are obtained by imposing the linear/angular displacement compatibility and force/moment equilibrium conditions at $x = -L/2$ and $x = L/2$ and solving the resulting equations simultaneously [27]. With the known complex wave amplitudes,

10

the time averaged power flow in the beam at any position can be calculated by using

$$P_{avg} = \frac{1}{2}\text{Re}(-w^*Q - \theta^*M) \tag{5}$$

where is w^* the complex conjugate of the velocity phasor and θ^* is the complex conjugate of the angular velocity phasor [59]. When the evanescent fields are ignored, this expression converges to simpler expressions obtained for bending waves in the literature [56].

Also note that, in order to account for the mechanical losses in the system, structural damping can be introduced in the model by attributing a complex elastic modulus to the material, $Y_s^* = Y_s(1 + j\eta)$, where η is the structural damping factor, which is generally much smaller than unity [27]. When this complex elastic modulus is substituted in Equation 1, the solution of the homogenous wave equation gives a complex bending wave number which can be approximated by $k_b^* = k_b(1 - j\eta/4)$.

2.2.2 Piezoelectric Energy Harvesting from One-Dimensional Bending Waves

Energy harvesting is accomplished when the piezoelectric patches with electrodes are connected to a finite, non-zero electrical load, $Z_l(\omega)$ (which may have purely resistive or resistive-reactive components [71, 43]). In this study, the harvesting model applies to both parallel and series connections of piezoceramic layers for the symmetric bimorph configuration. In Figure 5, the parallel connection is shown (see the Appendix A) for the equivalent representations of the series connection of piezoceramic layers). The x, y, and z directions are coincident with the 1, 2, and 3 directions (conventionally the poling direction is the 3-direction). The bending moment can be written for the piezoelectrically coupled configuration as [25]

$$M(x,t) = b\left(\int_{-h_p-h_s/2}^{-h_s/2} T_1^p z dz + \int_{-h_s/2}^{h_s/2} T_1^s z dz + \int_{h_s/2}^{h_p+h_s/2} T_1^p z dz\right) \tag{6}$$

where b is the width, and h_p and h_s are the thicknesses of the piezoceramic and substructure layer, respectively. Hereafter, the subscripts and superscripts p stands for the piezoceramic layers and s stands for the substructure layer. Furthermore, T_1^p and T_1^s are the stress components (in x-direction) in the piezoceramic and substructure layers, respectively. These

stress components can be written as follows:

$$T_1^p = \bar{c}_1 1^E S_1^p - \bar{e}_{31} E_3, \quad T_1^s = Y_s S_1^s \tag{7}$$

where $\bar{c}_1 1^E$ is the elastic modulus of piezoceramic at constant electric field, $\bar{e}_{31}$ is the effective piezoelectric stress constant, and Y_s is the elastic modulus of the substructure, S_1^p and S_1^s are the axial strain components $(S_1(x, z, t) = -z(\partial^2 w(x,t)/\partial x^2))$ and E_3 is the electric field component in z-direction. The piezoceramic layers are assumed to be identical; hence, the voltage across the electrodes of each piezoceramic layer is $v(t)$ in the parallel connection case. Since $\bar{e}_{31}$ has the same sign in both layers, the instantaneous electric fields are in opposite directions for the parallel connection (i.e., $E_3(t) = -v(t)/h_p$ in the top layer and $E_3(t) = v(t)/h_p$ in the bottom layer). Substituting Equation 7 into Equation 6, the bending moment for the composite cross-section is obtained as

$$M(x, t) = -YI_2 \frac{\partial^2 w(x, t)}{\partial x^2} + \chi v(t) \tag{8}$$

where YI is the flexural rigidity (bending stiffness) term of the composite cross-section under the short-circuit (or constant electric field) condition [3] and χ is the backward coupling term (that accounts for the feedback effect of electrical domain on the elastoacoustic domain), which can be defined as

$$\chi = \frac{b\bar{e}_{31}}{h_p} \left[\left(hp + \frac{h_s}{2} \right)^2 - \left(\frac{hs}{2} \right)^2 \right] = 2b\bar{e}_{31} h_{pc} \tag{9}$$

Here, h_{pc} is the distance between the neutral axis and the center of each piezoceramic layer in the harvester region $(h_{pc} = (h_p + h_s)/2)$.

For the composite cross-section, the moment equilibrium equations at the boundaries of the patch are modified according to the coupled mechanical equation, Equation 8.

$$-YI_1 \left(\frac{\partial^2 w_i^+}{\partial x^2} + \frac{\partial^2 w_r^-}{\partial x^2} \right) \bigg|_{x=-L/2} = -YI_2 \left(\frac{\partial^2 w_t^+}{\partial x^2} + \frac{\partial^2 w_{r2}^-}{\partial x^2} \right) \bigg|_{x=-L/2} + \chi v(t) \tag{10}$$

$$-YI_2 \left(\frac{\partial^2 w_t^+}{\partial x^2} + \frac{\partial^2 w_{r2}^-}{\partial x^2} \right) \bigg|_{x=-L/2} + \chi v(t) = -YI_1 \left(\frac{\partial^2 w_{t2}^+}{\partial x^2} \right) \bigg|_{x=L/2} \tag{11}$$

When the piezoelectric patches are connected to a load impedance $Z_l(\omega)$, which can consist of resistance and inductance, the system becomes electromechanically coupled, resulting in a ninth unknown term, $v(t) = V e^{j\omega t}$, voltage response of this coupled system.

The coupled electrical circuit equation (the ninth governing equation) for this system can be written as [25]

$$j\omega C_p^{eq} V + \frac{V}{Z_l(\omega)} - I_p = 0 \tag{12}$$

where C_p^{eq} is the equivalent capacitance of the piezoelectric patches in parallel connection due to two identical capacitors $(\bar{\varepsilon}_{33}^S bL/h_p)$ connected in parallel.

$$C_p^{eq} = 2\bar{\varepsilon}_{33}^S bL/h_p \tag{13}$$

Here, $\bar{\varepsilon}_{33}$ is the permittivity component at constant strain with the plane-stress assumption for the patch. In order to account for dielectric loss tangent $\tan\delta$, complex permittivity can be used conveniently to give $\bar{\varepsilon}_{33} = \bar{\varepsilon}_{33}(1 - j\tan\delta)$, yielding a complex capacitance expression. The dependent current source can be expressed as

$$i_p(t) = I_p e^{j\omega t} = -2\bar{e}_{31}h_{pc}b \int_{-L/2}^{L/2} \frac{\partial^3 w_2(x,t)}{\partial x^2 \partial t} dx \tag{14}$$

where $w_2(x,t) = w_t^+(x,t) + w_{r2}^-(x,t)$ is the total wave in the composite section. The amplitude of the current in Equation 12 can be obtained as $I_p = -j\omega\kappa$ with κ being the forward coupling term (that accounts for the excitation of electrical circuit by elastoacoustic waves), which can be extracted from Equation 14 as

$$\kappa = 4k_{b2}\bar{e}_{31}h_{pc}b\left[-(C_1+D_1)\sin\left(k_{b2}\frac{L}{2}\right) + (C_2+D_2)\sinh\left(k_{b2}\frac{L}{2}\right)\right] \tag{15}$$

Therefore this set of equations fully model the forward and backward coupling in this wave based electromechanical system. Note that ignoring backward coupling and evanescent waves, Equation 15 suggests that energy conversion will be effective at odd multiples of $\lambda/2$. This is an expected result as shown by others for A_0 mode Lamb waves, but as will be shown later both the backward coupling and evanescent waves are significant in determining optimal parameters for energy conversion [28].

After the complex wave amplitudes and voltage response are obtained by solving the coupled electroelastic system, the time averaged electrical power flow into the electrical load can be calculated as

$$P_{Eavg} = \frac{|V|^2}{2R_l} \tag{16}$$

13

This expression along with Equation 5 can be used to verify the power balance in the system, determine the power flow into the harvester, and hence evaluate the efficiency of the energy harvester from the known input mechanical power to the system.

2.2.3 Harvester with a Lumped Obstacle

Piezoelectric energy harvesting from propagating bending waves on beams with an integrated symmetrical obstacle can be modeled using the schematic shown in Figure 6. The goal of this approach is to recover and harvest part of the transmitted wave energy, which can also be interpreted as creating a spatially localized standing wave pattern. In the following, it is assumed that the lateral extent of the obstacle is much smaller than the wavelength, and thus a lumped modeling approach can be used.
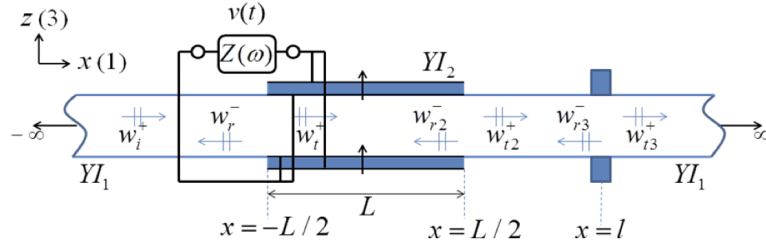
Figure 6: Piezoelectric energy harvesting from one-dimensional bending waves in the presence of a lumped obstacle.

When the transmitted wave (w_{t2}^+) from the harvester is incident upon the obstacle, it gives rise to reflected $(w_{r3}^-(x,t) = (F_1 e^{+jk_{b1}x} + F_2 e^{+k_{b1}x})e^{j\omega t})$ and transmitted waves $(w_{t3}^+(x,t) = (G_1 e^{-jk_{b1}x} + G_2 e^{-k_{b1}x})e^{j\omega t})$ for this additional discontinuity.

Wave amplitudes and the voltage response are obtained by imposing the linear/angular displacement compatibility and force/moment equilibrium conditions at $x = -L/2$, $x = L/2$ and $x = l$ and solving the resulting equations with the coupled electrical circuit equation simultaneously. The same equations at $x = -L/2$ are still valid, while at $x = L/2$ reflected wave from the obstacle (w_{r3}^-) is added to the compatibility and equilibrium equations.

14

The linear/angular displacement compatibility and force/moment equilibrium conditions at $x = l$ can be written as

$$w_{t2}^+(l) + w_{r3}^-(l) = w_{t3}^+(l)$$

$$\left(\frac{\partial w_{t2}^+}{\partial x} + \frac{\partial w_{r3}^-}{\partial x} \right)\Bigg|_{x=l} = \frac{\partial w_{t3}^+}{\partial x}\Bigg|_{x=l}$$

$$-YI_1 \left(\frac{\partial^3 w_{t2}^+}{\partial x^3} + \frac{\partial^3 w_{r3}^-}{\partial x^3} \right)\Bigg|_{x=l} = -YI_1 \frac{\partial^3 w_{t3}^+}{\partial x^3}\Bigg|_{x=l} + m_o \frac{\partial^2 w_{t3}^+}{\partial t^2}\Bigg|_{x=l}$$

$$-YI_1 \left(\frac{\partial^2 w_{t2}^+}{\partial x^2} + \frac{\partial^2 w_{r3}^-}{\partial x^2} \right)\Bigg|_{x=l} = -YI_1 \frac{\partial^2 w_{t3}^+}{\partial x^2}\Bigg|_{x=l} + I_o \frac{\partial^3 w_{t3}^+}{\partial x \partial t^2}\Bigg|_{x=l} \qquad (17)$$

where m_o is the total mass, and I_o is the total mass moment of inertia of the lumped obstacle.

2.2.4 Harvester at the Boundary of a Semi-Infinite Beam: Electromechanical Anechoic Boundary Condition

The possibility of an anechoic boundary condition transforming all the incident mechanical power into electrical power can also be investigated with the same approach. For this purpose, piezoelectric energy harvester is implemented at the boundary of a semi-infinite structure, and harvesting of the propagating bending waves are modeled using the schematic shown in Figure 7.
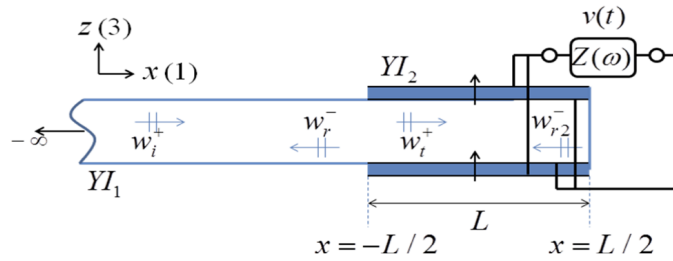
Figure 7: Piezoelectric energy harvesting from one-dimensional bending waves using a harvester at the boundary of a semi-infinite beam.

In this case the linear/angular displacement and force/moment equilibrium conditions at $x = -L/2$ are still valid; however, the conditions at $x = L/2$ are modified according to free end boundary conditions in which force and moment are equal to zero. Imposing

15

compatibility and equilibrium conditions at the boundaries in the mechanical domain and solving the coupled electromechanical equations, the time-averaged power flow in the beam and the time-averaged electrical power flowing to the electrical load of the harvester are calculated using Equations 5 and 16, respectively.

2.3   Simulation Results

In this section three case studies are given to illustrate the application of the model and discuss its salient results. In the simulations continuous harmonic wave analysis is performed on the infinite and semi-infinite beams. The structure is excited by an incident propagating wave with constant amplitude. The complex amplitudes of the transmitted and reflected waves and the output voltage are obtained under different electrical loading parameters. In all case studies, the system is assumed to be ideal, i.e. without any mechanical or electrical loss. For all the cases, a slender aluminum beam with 25.4 mm width and 1.6 mm thickness is used (ρ_s=2700 kg/m^3, Y_s=70 GPa). Note that the frequency range used is selected such that the Euler-Bernoulli beam theory yields accurate results by satisfying the condition $h/\lambda < 0.1$ [34].

2.3.1   Case Study I: Energy Harvesting on a Uniform Beam with Resistive and Resistive-Inductive Loading

In this case, a pair of piezoelectric patches with electrodes on each side of an infinite beam is connected to a complex electrical load for energy harvesting as shown in Figure 5(a). The piezoelectric energy harvester patches are made of PZT-5A and they are 0.267 mm thick and 50.8 mm long.

The bending wave energy harvester is first evaluated by using a resistive load connected to the piezoelectric patch terminals and the normalized output electrical power is calculated as a function of frequency for optimum resistive loads in the 0-30 kHz range. The normalization is done by dividing the output power to the square of the incident displacement amplitude (i.e. power output per meter squared). In 8(a), normalized electrical power is plotted against the wavelength normalized length, L/λ. Examining the graph along with the phase velocity calculations shows that the power output experiences a local minimum

16

when L is close to a multiple of the wavelength, as expected. Note that the behavior is not perfectly periodic in frequency due to the dispersive nature of the bending waves, i.e. the phase velocity being proportional to $\sqrt{\omega}$. The first peak, corresponding the $L \sim 3\lambda/4$ results in the local maximum power and power output exhibits local maxima at odd multiples of quarter wavelength, when $L \sim (2n+1)\lambda/4, n = 1, 2, ...$

As shown in Figure 8(a), for constant incident displacement wave amplitude, the maximum power increases with frequency under optimal resistive loading because the incident power increases. Another useful metric for comparing different load conditions is the efficiency of the energy harvester. In this case, the harvested power is normalized to the mechanical power of the incident wave (Equation 5). Figure 8(b) shows the efficiency of the harvester as a function of normalized length. In this case, the peaks occur when L is approximately an odd multiple of $\lambda/2$. This is expected as at higher frequencies where L is larger than the wavelength, only the mechanical energy in the last $\lambda/2$ length of the patch is efficiently converted to electrical domain, similar to the reduced coupling coefficient in higher order modes of piezoelectric resonators [42]. Also, it is seen that, with the non-dimensional representation of the patch length, the efficiency plot reduces to a unified curve for different patch lengths. Hence, once the frequency range for harvesting is determined, harvester dimensions can be chosen to work efficiently at those frequencies as long as the resistor value is also chosen optimally.

The optimal load resistance can be identified through 3D plots of harvested power and conversion efficiency as a function of resistance and normalized patch length. In Figures 9(a) and (b), harvested power and power conversion efficiency are plotted, respectively, in the 0-8 kHz range. In Figure 9(a) the local maximum is obtained around $R_l = 400\ \Omega$ at $L \sim 3\lambda/4$ with minima around frequencies where L is a multiple of wavelength. In Figure 9(b) the corresponding plot for conversion efficiency is shown, where the global maximum for efficiency is $\sim 4.6\%$ for $R_l = 900\ \Omega$ at $L \sim \lambda/2$. In comparing Figures 9(a) and (b), one realizes that the maximum power peak shifts toward higher frequencies where $L \sim \lambda$, since the input power increases with frequency. In contrast, the conversion efficiency peak is at a lower frequency, roughly corresponding to the half wavelength condition.
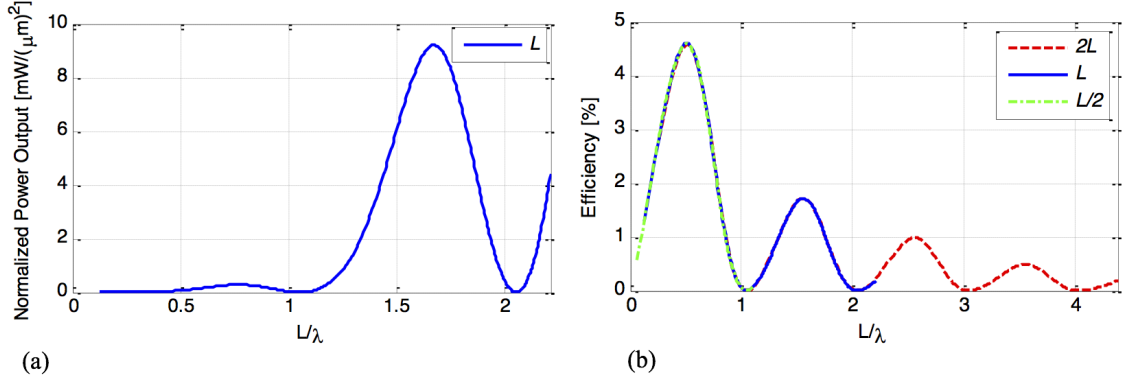
Figure 8: Variation of (a) the harvested power and (b) the power conversion efficiency with normalized patch length under optimal resistive loading.
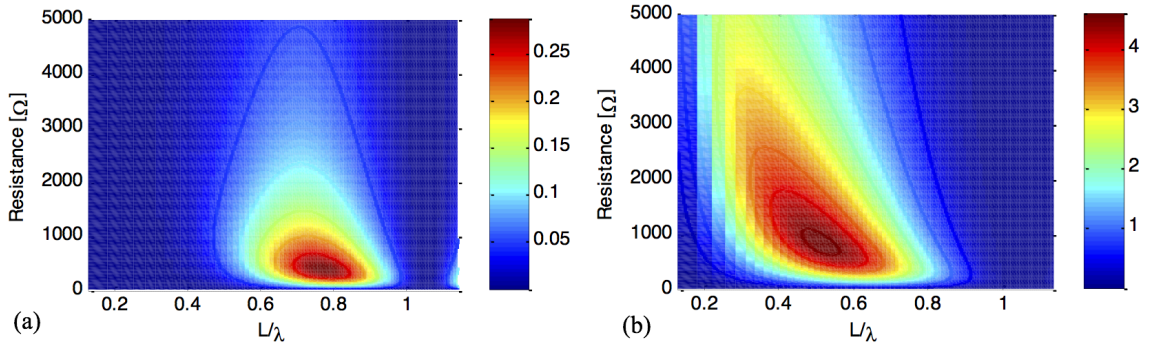
Figure 9: Variation of (a) the harvested power $(mW/\mu m^2)$ and (b) the power conversion efficiency (%) with load resistance and normalized patch length for resistive loading case.

These results, essentially based on wavelength matching, are obtained by others through analyses which ignored backward coupling (for example cf. Figure 10 in [28] for A_0 mode Lamb waves, which are similar to bending waves especially at low frequencies). The impact of a full model for optimizing the efficiency of energy harvesting is more clearly seen when complex conjugate electrical impedance matching is used [71, 43, 39]. For example, in the case of a capacitive source such as the piezoelectric patch, one can achieve electrical impedance matching using an inductance in parallel with the load resistance, so that the

load impedance becomes

$$Z_l(\omega) = \left(\frac{1}{R_l} + \frac{1}{j\omega L_l + R_{ind}} \right)^{-1} \tag{18}$$

where L_l is the inductance and R_{ind} is the internal resistance of the non-ideal inductor. Note that, in the simulations, all components are assumed to be lossless (i.e. $\eta = \tan\delta = R_{ind} = 0$), i.e. harvester characterization is performed under ideal conditions.

Typically for maximum power transfer at a particular frequency the inductance value is chosen as ($L_l = 1/(\omega^2 C_p^{eq})$) to eliminate the capacitive component of the impedance and the resistance value is varied as the free parameter. First set of results in Figure 10 shows the consequence of this approach, which provides 50% efficiency over a range of normalized patch lengths, a significant improvement over the resistive case. However, by choosing both the inductance and resistance values for complex conjugate matching of the impedance at the piezoelectric patch terminals, this range can be extended except for a narrow region around $L \sim \lambda$. This approach makes the optimal condition nearly independent of the patch length, and effectively frequency, which means that high conversion efficiencies can be obtained with small piezo patches by adjusting electrical load. The inductance values rendering the maximum efficiency at different frequencies are normalized by $1/(\omega^2 C_p^{eq})$ as illustrated in Figure 10(b). This graph shows that most probably the evanescent waves, especially effective at short patch lengths and multiples of λ, contribute to the imaginary part of the electrical impedance changing the optimal tuning inductance from $1/(\omega^2 C_p^{eq})$.

Following a similar analysis to the resistive load case, in Figure 11(a) the normalized power output is plotted as a function of resistance and non-dimensional wavelength under impedance matching conditions. It is seen that the peak frequency shifts to the higher end of the frequency band, limited by the $L \sim \lambda$ condition. Figure 11(b) shows conversion efficiency for the same loading condition in which the maximum efficiency is limited to 50%, as expected from a passive, reciprocal 3-port device with one conjugate matched port [65]. In this case, the impedance matched port is the piezoelectric patch terminals and the mechanical port terminations are symmetrical. A simple analysis of the scattering matrix for this case indicates that the rest of the mechanical power incident from the left side of the

beam is equally reflected back (25%) and transmitted (25%) to the other side of the patch.

(a)

(b)
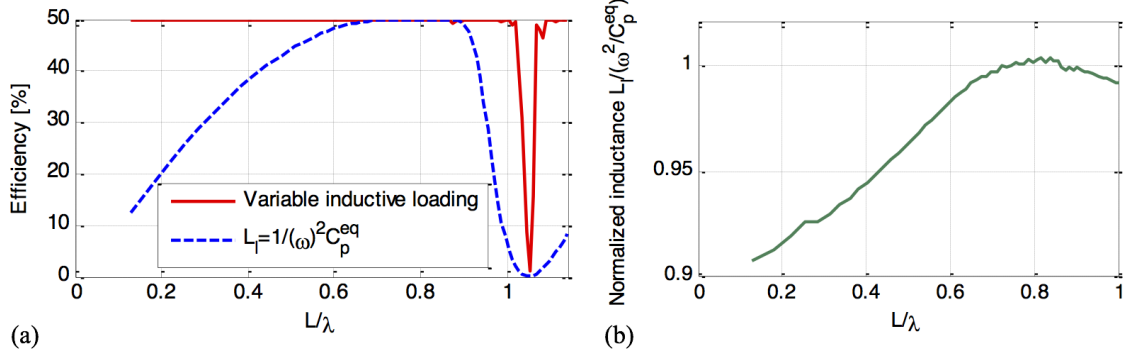
Figure 10: Variation of (a) the harvested power efficiency with normalized patch length under optimal resistive-inductive loading and (b) the corresponding normalized inductance.

(a)

(b)
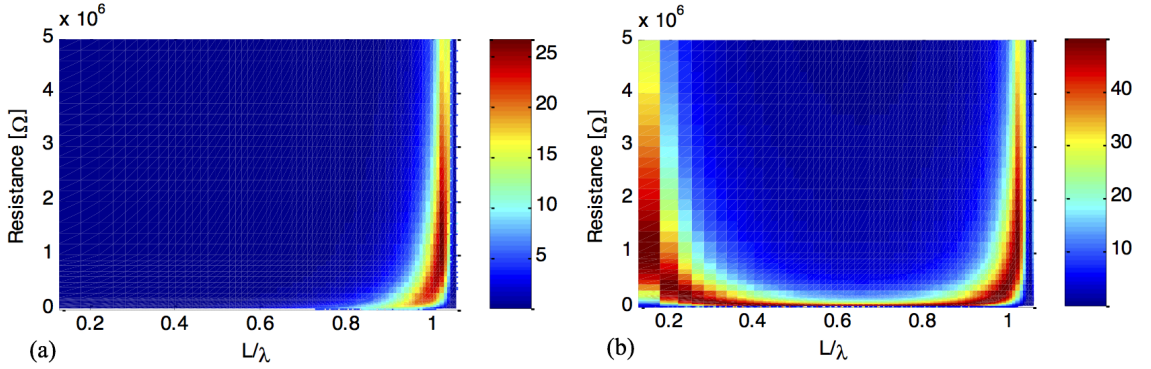
Figure 11: Variation of (a) the harvested power (mW/μm^2) and (b) the power conversion efficiency (%) with load resistance and normalized patch length for parallel resistive-inductive loading case.

It is noted that unlike energy harvesting applications from vibrations of finite structures with standing waves (i.e. modal vibrations) which can be modeled with a simpler formulation and lends itself to Den Hartogs invariant point concept to obtain optimal loading parameters, in the case of wave energy harvesting the complexity of the problem prevents closed form expressions for optimization even only bending waves are considered [36].

2.3.2 Case Study II: Energy Harvesting Enhancement by Using a Lumped Obstacle

As can be seen in Figure 6, when a lumped obstacle is introduced, part of the bending wave energy is trapped between the harvester and the lumped obstacle resulting in a variation of the harvested power. In this case study, a pair of rectangular steel pieces (with 12.7 mm height, 3.175 mm length and 25.4 mm width) is considered as lumped mass (16 grams) obstacle. The same piezoelectric patches are implemented as the energy harvesting interface connected to the complex electrical load with optimal parameters obtained for maximum efficiency.

Variation of the harvester efficiency by means of a lumped mass obstacle is simulated under resistive (at 2.5 kHz) and resistive-inductive loading (at 1.5 kHz) cases with changing obstacle location in the transmitted wave domain. Figures 12(a) and (b) show the calculated variation of the conversion efficiency under continuous wave excitation with lumped mass location normalized to wavelength λ at the excitation frequency for resistive and resistive-inductive loading, respectively. As expected from standing wave patterns, the variation of harvester efficiency has regular maxima and minima with $\lambda/2$ periodicity. The harvester efficiency without the obstacle is constant at this frequency, and this value is also included in the plots for comparison purposes. Hence, it can be concluded that the efficiency of the harvester can be increased dramatically with the addition of the symmetric lumped mass. The results also show that there is a distance limit below which the optimal conditions may not be achieved. This limit is $\sim \lambda/4$, where evanescent fields are significant as shown in Figure 12(c). The high efficiency values close to zero mass distance would not be practical due to limited mass dimensions.

2.3.3 Case Study III: Multifunctional Energy Harvester - Anechoic Boundary Condition

In this case study, the energy harvester patch is placed at one boundary of the semi-infinite structure to effectively implement a multifunctional energy harvester which also realizes an anechoic boundary condition. The same material and dimensional properties given in the previous case studies are used except for the length of the piezoelectric energy harvester.
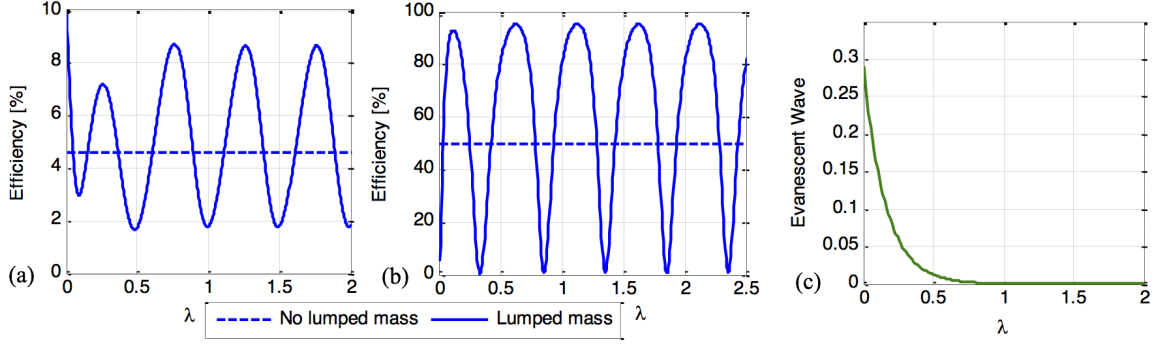
Figure 12: Change in harvester efficiency via lumped mass under (a) resistive loading at 1.5 kHz, (b) resistive-inductive loading at 2.5 kHz; (c) normalized evanescent wave amplitude versus wavelength.

In the simulations, 33 mm long patches are used as the energy harvesting interface bonded at the end of the beam. Thus, high frequency harvesting is enabled in order to eliminate the limitations of the experimental setup which will be explained in Section 2.4.3.

The efficiency of the multifunctional harvester is obtained for different frequencies between 0-15 kHz under optimal resistive-inductive loading based on conjugate impedance matching. The efficiency versus normalized patch length is shown in Figure 13(a). Optimal loading parameters are obtained through 3D plots of conversion efficiency as a function of resistance, inductance and normalized patch length, and plotted in Figure 13(b). It can be observed that theoretically 100% efficiency can be obtained at different frequencies by conjugate impedance matching. In practice the efficiency would decrease to some extent due to parasitic losses as will be seen in the experimental results.

2.4   Experimental Setup and Results

In the experiments a pair of piezoelectric patches is used as the energy harvesting interface connected to a complex electrical load (resistance and inductance). A long slender beam supported by soft foam at several locations is used as the bending wave propagation medium and Laser Doppler Vibrometers (LDVs) are used to measure the incident, transmitted, and reflected waves generated by a piezoelectric actuator as shown in Figure 14. The LDV close to the actuator measures both the incident and reflected waves from the harvester, while the second LDV measures transmitted waves passing through the harvester.

22
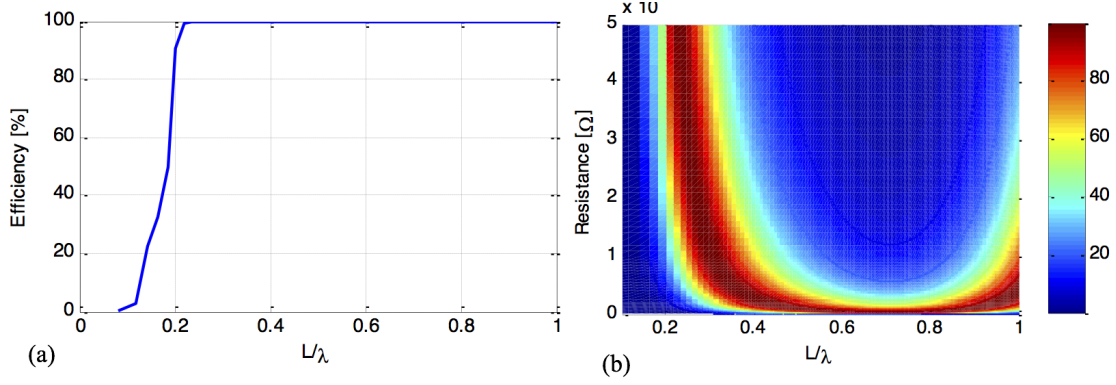
Figure 13: Variation of (a) the harvested power efficiency with normalized patch length under optimal resistive-inductive loading and (b) the power conversion efficiency with load resistance and normalized patch length for parallel resistive-inductive loading case.
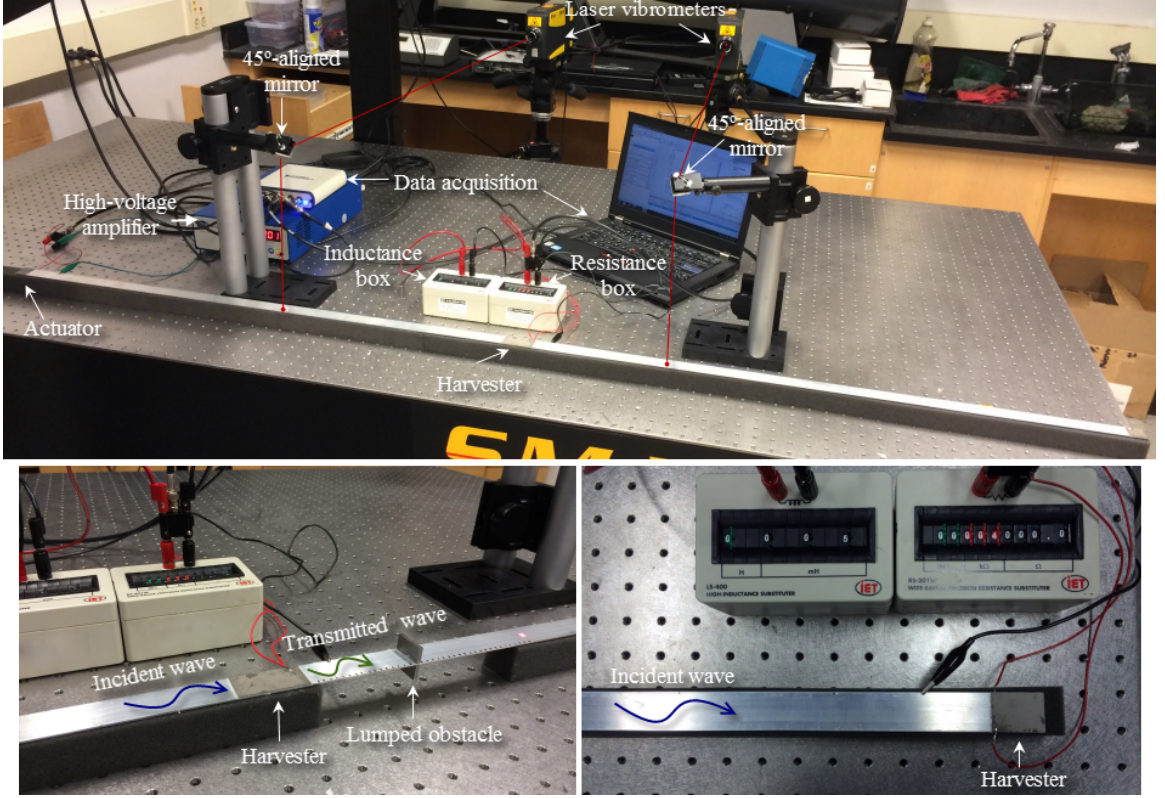
Figure 14: Experimental setups: (a) Case study I with no lumped obstacle, (b) case study II with lumped obstacle case, and (c) case study III with energy harvester at one boundary.

In order to prevent spurious interference between reflected waves from the end of the beam and the propagating waves in the harvester domain, the number of cycles of the input

excitation to the piezoelectric actuator is limited. Furthermore, the internal resistance of the inductance box, structural damping factor, and dielectric loss of the piezoelectric patches are included in the experimental analysis. The structural damping factor is identified for each frequency through separate experiments by taking two simultaneous LDV measurements at known distances of freely propagating waves and considering the power levels. A constant dielectric loss is extracted from the difference between the measured and calculated output voltage signals. As a result, the structural damping factor in the beam is taken as 0.0025 at 1.5 kHz and the dielectric loss in the piezoelectric patch is taken as 2% (accounting for the dielectric loss caused by the epoxy layers) in the calculations.

2.4.1 Case Study I: Resistive and Resistive-Inductive Loading with no Obstacle

The experimental setup shown in Figure 14(a) is first used to test the validity of the results from Section 2.3.1. Using the LDV signal for the incident wave, the waveforms for the output voltage, transmitted and reflected velocity are calculated via transient analysis with the theoretical frequency domain transfer function and compared with the measured waveforms. For instance, the voltage output is calculated by inserting the measured incident velocity in the following formula:

$$V(t) = \text{IFFT}\{\text{FFT}\{Velocity_{inc}(t)\}G(\omega)e^{-jk_{b1}(\omega)L_d}\} \tag{19}$$

where $G(\omega)$ is the theoretical transfer function between the incident velocity and the voltage response, k_{b1} is the theoretical wavenumber and L_d is the distance between the harvester and LDV location.

The center frequencies of the signals used for comparison are selected to correspond to the maximum power and efficiency based on Figures 8 and 9. For example, at 1.5 kHz where $L \sim 0.8\lambda$ 900 Ω resistance is found and used as the optimal resistive loading. Similarly, at 2.5 kHz where $L \sim 0.5\lambda$ 8 kΩ resistance and 35 mH inductance (with 13.2 Ω internal resistance) is used for optimal resistive-inductive loading. Figure 15 shows the results comparing measured and calculated results for the resistive and resistive-inductive loading case the left and right columns, respectively.

24
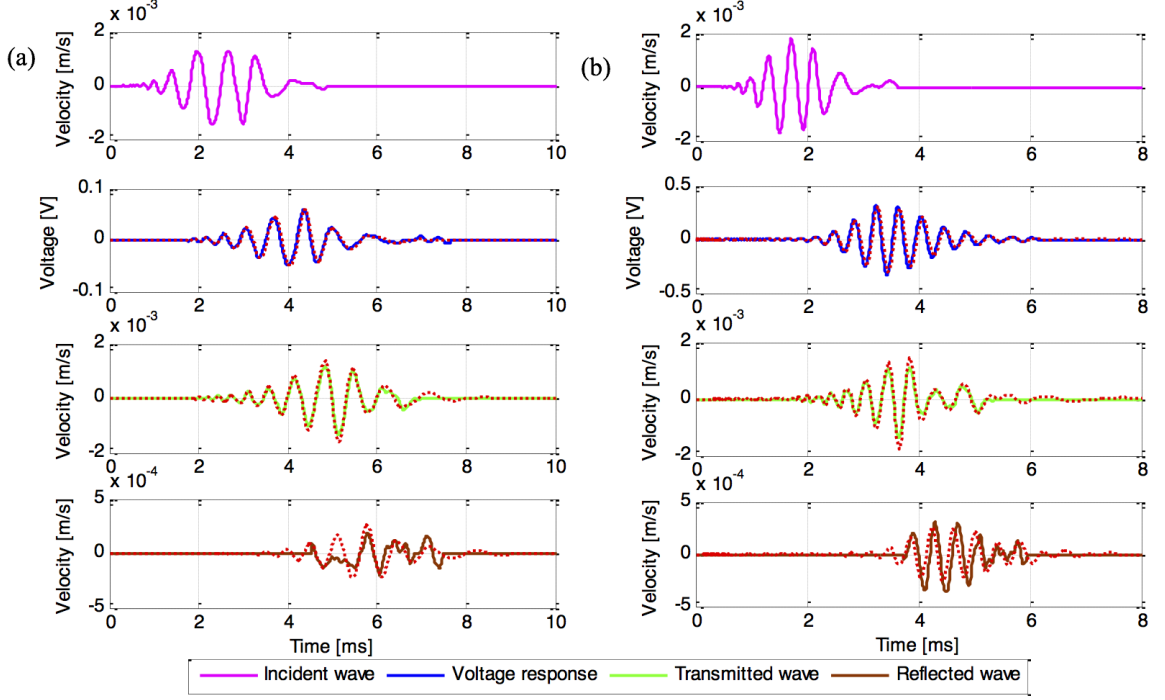
Figure 15: Comparison of the theoretical and experimental voltage response and transmitted and reflected wave behaviors along with the measured incident waves under (a) resistive loading at 1.5 kHz and (b) resistive-inductive loading at 2.5 kHz (solid curves: measured; dashed curves: calculated).

The top row of Figure 15 shows the measured incident wave LDV signals. The calculated output voltage waveforms (second from the top row) and transmitted waveforms perfectly match the measurements. Note that the voltage and power levels obtained for resistive-inductive loading are significantly higher than resistive loading as expected from the simulations. The reflected velocity waveforms agree reasonably well with the measurements considering the low signal levels as compared to transmitted waves.

For further validation, the experiments are repeated under optimal loading conditions for different frequencies between 500Hz-8 kHz. Harvested power is obtained by dividing the power spectral density (PSD) value of the piezoelectric voltage response at the harvesting frequency by the load resistance. Similarly, average power carried in the incident wave is calculated by multiplying the PSD of the incident wave packet with $YI_1 k_{b1}^3/\omega$ resulting from Equation 5. Figure 16 shows the comparisons of harvested power and efficiency under optimal resistive and resistive-inductive loading conditions. As can be seen in Figure

25
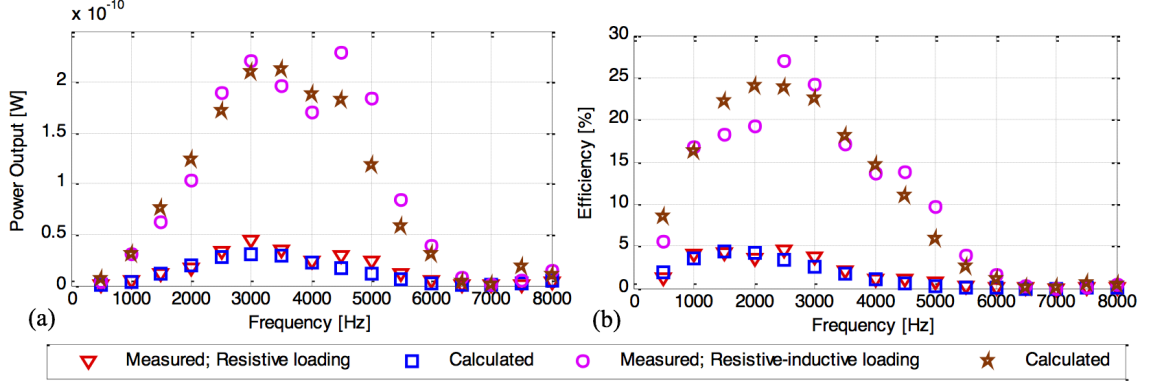
Figure 16: Comparison of the theoretical and experimental (a) maximum power and (b) maximum efficiency with the optimal parameters of resistive and resistive-inductive loading.

16(a), the experimental maximum power is around 3 kHz for resistive loading and 4.5 kHz for the resistive-inductive loading, similar to predictions. Furthermore, experimental maximum efficiency is 4.5% at 1.5 kHz and 26% at 2.5 kHz for resistive and resistive-inductive loading, respectively (Figure 16(b)). Note that the decrease in the maximum efficiency from 31% (including the inductance loss) to 26% is because of the effect of mechanical and dielectric losses in the system. Despite of the discrepancies in the measured and calculated efficiency and power output levels (arising from the slight differences in the wave packets), the experiments at different frequencies can be considered in satisfactory agreement with the simulations. These results along with the waveform comparisons validate the proposed bending wave energy harvester model.

2.4.2 Case Study II: Power Enhancement by Using a Lumped Obstacle

The setup in Figure 14(b) with the same piezoelectric energy harvester is used to test the validity of the theoretical model for energy harvesting improvement with lumped obstacles. In Figure 17, efficiency versus normalized lumped mass position is plotted for optimal resistive and resistive-inductive loading cases at 1.5 kHz, and 2.5 kHz, respectively. The lumped mass is located in 5 mm increments in the transmitted wave domain. Note that the appearance of maximum peaks with $\lambda/2$ periodicity, the significant difference in efficiency with inductive-resistive loading and the asymmetric variation of the efficiency as compared to no-obstacle case all agree very well qualitatively with the predictions in Figure 12.
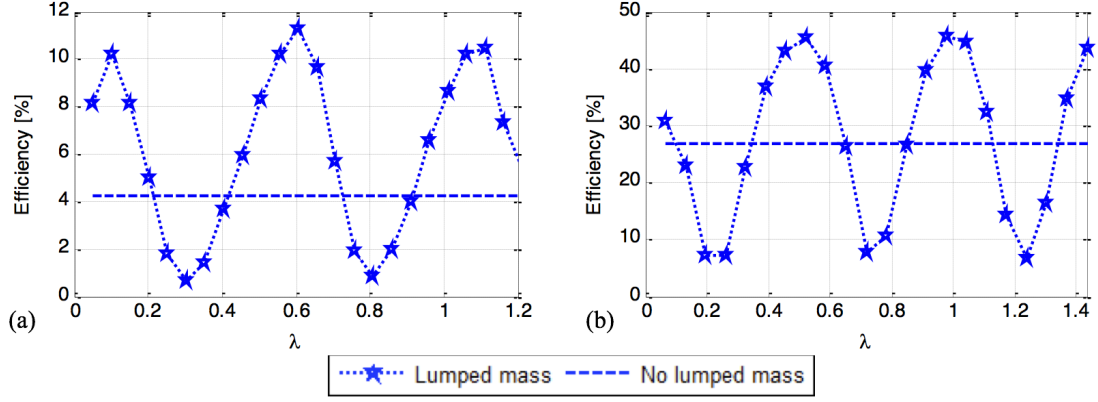
Figure 17: Experimental power enhancement via lumped mass under, (a) resistive loading at 1.5 kHz, (b) resistive-inductive loading at 2.5 kHz.

Transient analysis comparisons in Figure 18 also show excellent agreement with respect to the shape of the waveforms and signal levels. The effect of evanescent waves for small normalized mass obstacle distances are also observed qualitatively as the periodic curves are distorted as the distance is reduced below 0.2λ.
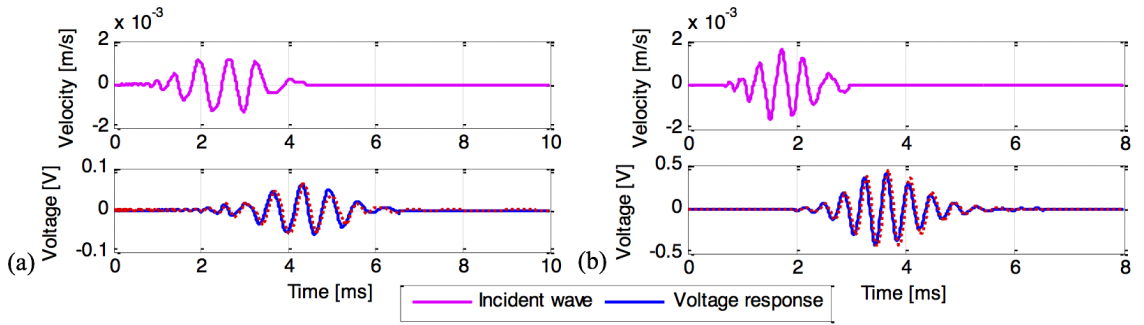
Figure 18: Comparison of the theoretical and experimental voltage response along with the measured incident waves under (a) resistive loading at 1.5 kHz, (b) resistive-inductive loading at 2.5 kHz (solid curves: measured; dashed curves: calculated).

2.4.3 Case Study III: Multifunctional Energy-Harvesting Quasi-Anechoic Boundary Condition

The multifunctional energy harvester concept (Figure 14(c)) analyzed in Section 2.3.3 is also experimentally tested. In contrast with the ideal lossless case leading to 100% harvester efficiency, a lower figure is expected due to losses such as the internal resistance of the inductance box, mechanical loss in the system and the dielectric losses in the harvester. Therefore, instead of a 100% efficient anechoic boundary condition, a quasi-anechoic boundary condition performance is expected. In order to avoid the interference of the incident wave with the reflected wave, the harvester is tested at a higher frequency (at 7.95 kHz) with 5 cycles of burst excitation. For electrical loading, the optimal parameters for this particular frequency is used ($R_l = 4$ kΩ, $L = 5$ mH and $R_i nd = 3.4$ Ω), and LDV measurement at a single location is used to record the incident and reflected waves. Figure 19(a) shows the comparison of the calculated and measured incident wave amplitude, the harvester output voltage and the reflected wave amplitude. In addition to showing excellent agreement, the notch in the reflected waveform shows that the harvester is effectively anechoic at a certain frequency contained in this wavepacket.

The particular anechoic frequency is much better delineated by the PSD analysis shown in Figure 19(b). The incident wave hasa range of frequencies in the 7-9 kHz range due to the tone-burst excitation. As a result, the reflected wave includes those frequencies. However, the reflection is clearly minimized at the targeted frequency of 7.95 kHz with optimal loading conditions. Calculations including the losses in the system predict a power reflection coefficient of 5.7% at this frequency, which agrees very well with the measured 6%. In terms of harvester performance, calculations show that at this frequency, the addition of the internal loss of the inductor reduces the efficiency to 82%. Inclusion of mechanical and dielectric losses in the system further reduces the efficiency to 36% which compares very well to the measured efficiency of 32%.
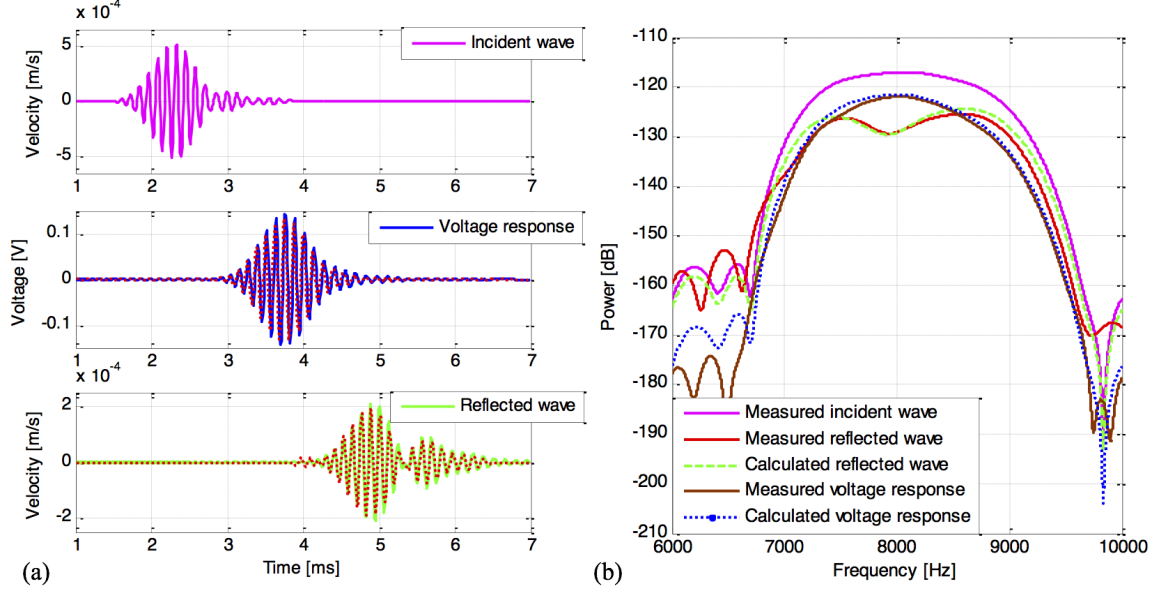
Figure 19: Comparison of the theoretical and experimental voltage response and reflected wave behaviors along with the measured incident waves: (a) Transient analysis and (b) PSD analysis (solid curves: measured; dashed curves: calculated).

2.5   Conclusions

In this chapter an electroelastic modeling framework is proposed for a piezoelectric energy harvester exploiting one-dimensional bending waves propagating in infinite and semi-infinite beams [87, 90, 85]. The fully coupled model that accounts for piezoelectric structure and complex electrical load is based on the wave equation solution and the piezoelectric constitutive relations coupled in the equilibrium and compatibility conditions at the harvester boundaries and the electrical circuit equation. The model is used to obtain the time averaged power flow in the beam and the time-averaged electrical power flowing to the harvester as well as the efficiency of the harvester. With the simulation case studies, wavelength matching, resistive and resistive-inductive circuits, and performance enhancement by a localized obstacle are explored. A substantial performance enhancement is observed in ideal conditions by resistive-inductive loading as compared to the resistive loading case with more than an order of magnitude increase in the maximum power output and 4.5% to 50% improvement in the maximum efficiency over a larger frequency range. In the case of power enhancement method with spatially localization of a lumped obstacle, the harvested power

is almost doubled by properly locating the obstacle with respect to the harvester and the maximum efficiency of 95% is obtained under resistive-inductive loading. Additionally, a multifunctional piezoelectric energy harvester anechoic boundary condition is proposed, in which nearly all the energy in a propagating bending wave can be extracted using piezoelectric patches at the free end of a beam. The harvester is tested under these different configurations, and the proposed work is validated with the experiments. Through transient and power analyses, the experimental and theoretical results are compared and an excellent agreement is observed. Due to the losses in the system, harvester efficiency decreases to 26% for resistive-inductive loading and 45% efficiency is obtained with the lumped mass addition. On the other hand, in the anechoic boundary condition experiments, a 6% power reflection ratio is obtained, resulting in quasi-anechoic behavior, which is very promising for achieving an energy-harvesting boundary condition that minimizes the reflections. These enhancement methods are most effective and practical when piezoelectric patch lengths and obstacle to patch distances are $\sim \lambda/4$, where evanescent fields become insignificant, while the model can readily accommodate the presence of evanescent waves for arbitrary patch lengths. While the present effort explored electroelastic dynamics of bending waves in an infinite/semi-infinite beam shunted to an AC circuit (with linear resistive and reactive components for linear impedance matching), future work may investigate nonlinear energy harvesting circuits with standard AC-DC conversion [77, 74], switching circuits [35, 78] for boosted power output in case of weak electromechanical coupling, as well as nonlinear impedance matching circuits [43].

<center>**Chapter III**</center>

<center>**STRUCTURALLY-EMBEDDED MIRRORS FOR ELASTIC WAVE**

FOCUSING AND HARVESTING</center>

3.1 *Introduction*

The wave approach provides new insights and opens new avenues for the enhancement of mechanical-to-electrical energy conversion efficiency by spatial localization through the use of local obstacles as presented in Chapter 2 [87]. The harvesting of elastic waves propagating in 2D structures can be enhanced dramatically via focusing wave energy using mirror concepts. Limited research has explored elastic wave mirror design in terms of mirror geometry and reflector configurations. Cylindrical stubs that form elliptical [9] and parabolic geometries [10] have been used to focus structure-borne waves originating from a point source and incident plane waves, respectively, as shown in Figure 2. In these first-generation heuristic efforts, the bulky stub extensions (10 times thicker than the host plate) served as effective reflectors while drastically altering the thin host structures. These first-generation mirror configurations may not be applicable in many scenarios that require preserving the flat host structure. Furthermore, it was observed [9, 10, 11] that the side lobes near the geometric focal spot contained significant energy levels. Consequently, patterned segmentation of the piezoelectric domain was employed [11] through a wavenumber transformation procedure to harvest the energy at the side lobes.

In order to enable mirror structures beyond heuristic designs that avoid substantial modification of the host structure and complex segmented harvesters, it is required to have a detailed understanding of the elastic wave focusing performance of the mirror geometry as well as the dynamics of the structurally-embedded reflectors used to form the structurally embedded mirror (SEM) [93]. In this chapter, first we unveil a basic relationship between the mirror geometry and wavelength of the lowest asymmetric Lamb wave mode (A_0 mode) in a plate with respect to formation and minimization of the near side lobes observed in

<center>31</center>

earlier work [9, 10, 11]. A detailed investigation on the reflection coefficient for these waves for reflectors formed by inserting metallic spheres (e.g. tungsten, lead, steel) into blind holes in a flat aluminum plate domain is presented. The frequency dependence of reflection coefficient for spherical inclusions of tungsten, lead, and steel in aluminum is determined and its impact on SEM performance is discussed. Finally, experiments are performed on an elliptical SEM using tungsten inclusions to verify the simulations and explore the energy harvesting performance enhancement. The perforated mirror scenario (mass subtraction rather than inclusion) via through holes is also addressed briefly.

3.2 *Mirror Geometry and Wavelength Considerations*

The impact of mirror geometry on focusing performance, hence the harvester design is investigated through finite element analysis (in COMSOL) of both elliptical and parabolic mirrors. The results, summarized in Figures 20 and 21, reveal a simple recipe for design of elliptical and parabolic elastic wave mirrors, respectively. Figure 20(a) shows the elliptical mirror design, where a is the major axis, b is the minor axis and f is the distance to the focal point from the center of the semi-ellipse (hence $f^2 = a^2 - b^2$). It is useful to define another geometric parameter, $d = a - f$, which is the distance between the focus and the edge of the mirror in Figure 20(a). Figures 20(b)-(d) show the out-of-plane RMS (root-mean-square) velocity wave field when elastic waves are generated by a point source at the other focus of the semi-ellipse (not shown in the figure) are concentrated at the focus of SEMs with same aperture but different focal points, namely $d = 3\lambda/4$, $d = \lambda$ and $d = 5\lambda/4$ cases. In the simulations, an aluminum plate of 3.175 mm thickness with 3 mm diameter tungsten inclusions is considered with a boundary load with burst sinusoidal (Gaussian pulse) forcing with a center frequency of 50 kHz. As can be observed in Figures 20(b)-(d) the side lobes near the focal point have significant energy when the distance d is greater or smaller than wavelength λ. On the other hand the side lobes become negligible when the mirror is designed to have a d value that is equal to λ. This observation, supported by simulations over a range of d values, leads to a criterion that the ideal elastic wave mirror with the minimal (or negligible) side lobes should have $d \sim \lambda$ (roughly $d = \lambda \pm 0.1\lambda$). Remarkably, other

than the elliptical mirror scenario (which is the main focus of this chapter), Figure 21 shows similar results for the parabolic mirror case as well. Therefore, when designing a parabolic SEM to focus incident elastic plane waves at a given frequency, one should again choose $d \sim \lambda$ (as the geometry-wavelength design criterion) in order to reduce the energy of side lobes. This criterion has a direct impact on the harvester design as a smaller piezoelectric patch with a single electrode can be used instead of a larger transducer with a complex harvester/electrode pattern and wiring [11]. This criterion can be also be interpreted in the reverse sense to choose the frequency in case the mirror is already fabricated, but the excitation frequency is a rather flexible system parameter to choose (e.g. in wireless power transfer problems [72, 76, 89]).

3.3   Reflection Coefficient and Frequency Considerations

Elastic wave reflection from the inclusions forming the mirror is another critical factor in SEM performance. In addition to the material property mismatch, one should also consider the finite size of the inclusions leading to frequency dependent reflectivity. This is investigated through finite-element simulation of A_0 mode Lamb wave reflection and transmission in a simplified aluminum waveguide where the reflector is formed by spherical inclusions (shrink fit) in cylindrical blind holes (Figure 22(a)). This structure is periodic in the lateral dimension, essentially simulating the reflection of a plane elastic wave incident in a laterally infinite plate. Figure 22(b) shows the calculated reflection coefficient for a 3 mm diameter spherical inclusion with 3.5 mm lateral periodicity in 3.175 mm thick aluminum plate simulated by time-domain analysis for tungsten, steel and lead spheres embedded in otherwise epoxy filled blind holes. It is observed that, at very low frequencies, the reflection coefficient is very low since the wavelength is much larger than the inclusion size. The trends in the reflection coefficient with increased frequency is not monotonic. For the frequency range shown in Figure 22(b), tungsten and steel inclusions result in single frequency of almost zero reflection, while the lead inclusion yields multiple such frequencies. A careful investigation reveals that these are the transmission resonances (TR) of the inclusions that lead to almost perfect wave transmission, compatible with the flexural nature of the A_0 mode Lamb
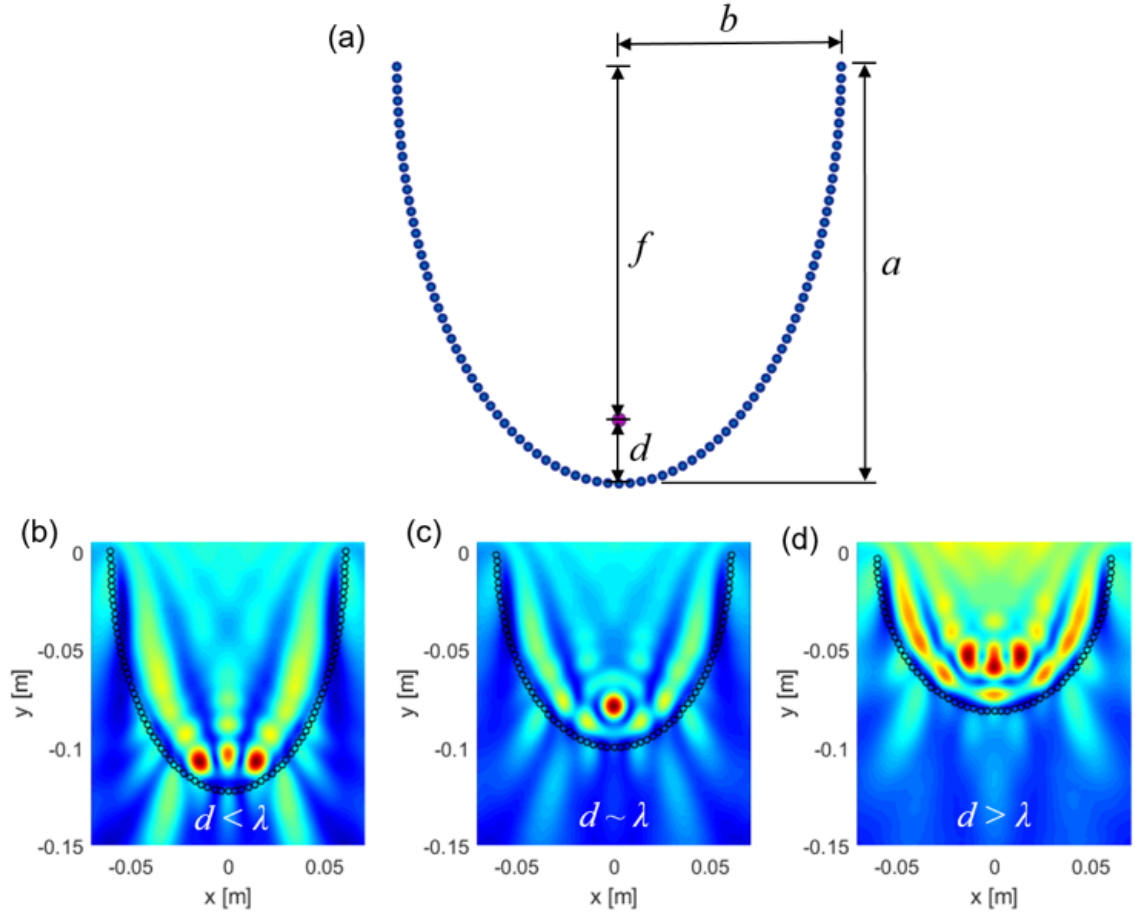
Figure 20: (a) Schematic and geometric parameters of the elliptical SEM design made from spherical inclusions and (b)-(d) wavelength-geometry relationship revealing ideal focusing for $d \sim \lambda$. Numerical simulation of the out-of-plane RMS velocity wave field for (b) $d = 3\lambda/4$, (c) $d \sim \lambda$, and (d) $d = 5\lambda/4$.
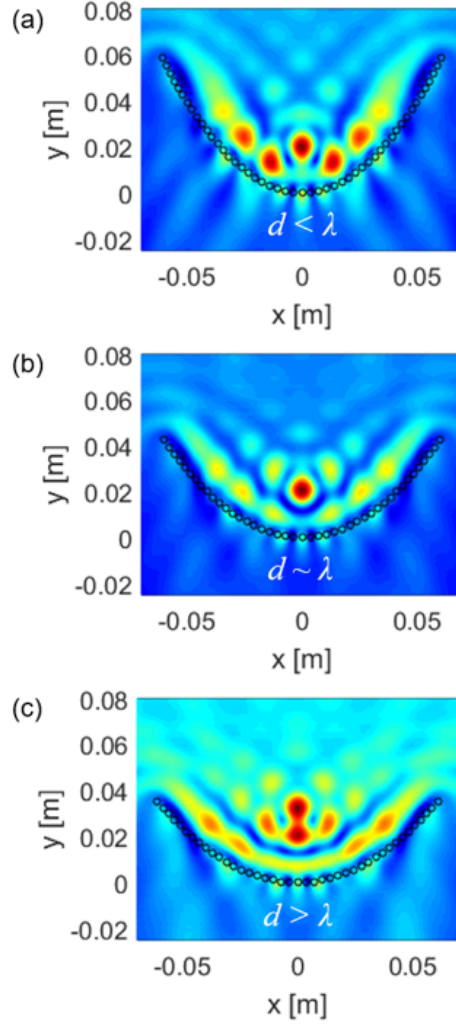
Figure 21: Parabolic SEM wavelength-geometry relationship revealing ideal focusing for d
. Numerical simulation of the out-of-plane RMS wave field for (a) $d = 3\lambda/4$, (b) $d \sim \lambda$, and (c) $d = 5\lambda/4$.

wave (see the arrows indicating the rotation of the tungsten sphere at 137 kHz in Figure 22(c)). The first resonances of these spherical inclusions occur at 137 kHz, 162 kHz, and 175 kHz for tungsten, steel and lead, respectively, indicating that one should avoid transmission resonances for SEM implementation as the mirror reflection is poor. Instead, consider the first peak neighborhood of all inclusion materials, which is around 50 kHz (where the reflection levels are dominated by mass effect of inclusions). If one makes geometrically identical mirrors using identical inclusions of these materials in an aluminum plate, it can be expected that the intensity should scale with the reflection coefficient. This is explored through finite-element simulations of the transient wave field with parameters similar to that of Figure 20(c).
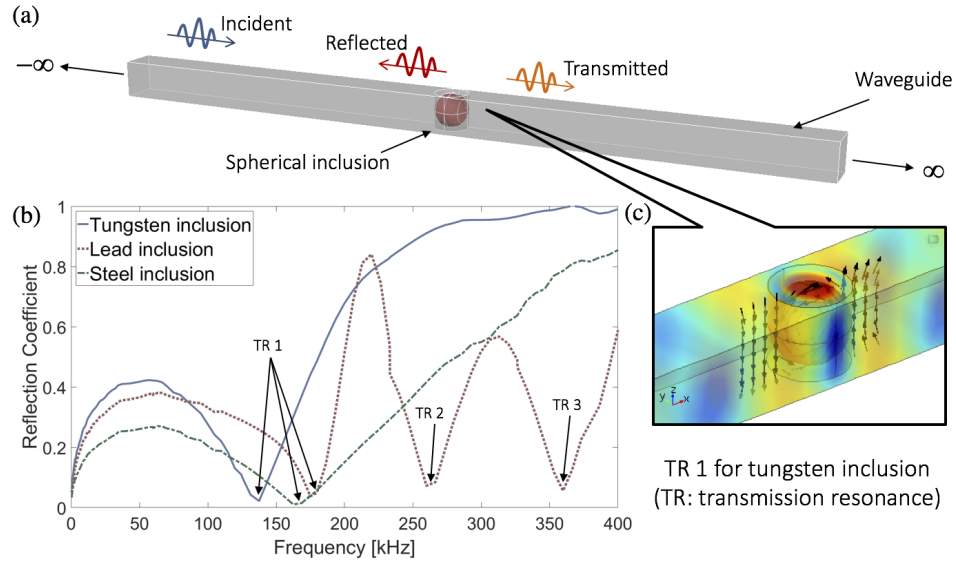
Figure 22: (a) Waveguide with a spherical inclusion showing the incident, transmitted, and reflected wave components (the waveguide is aluminum while the inclusion in the cylindrical blind hole is shrink-fit tungsten, lead, or steel); (b) Reflection coefficient for different materials embedded in aluminum exhibiting ltransmission resonances (denoted by TR) yielding almost zero reflection (which must be avoided in mirror design); (c) Close-up view of the first transmission resonance for a tungsten inclusion (arrows indicate the direction of motion compatible with the lowest asymmetric Lamb wave mode).

Figure 23 shows the RMS wave fields of geometrically identical SEM configurations made from spherical tungsten, lead, and steel inclusions of aforementioned dimensions embedded

in aluminum. The mirrors for all cases have $d \sim \lambda$ (Figure 20(a)) to reduce side lobes. As expected, the peak amplitude at focus scales linearly with the mass density of the inclusion, which in turn is proportional to the reflection coefficient at this frequency (cf. Figure 22(b) for 50 kHz).
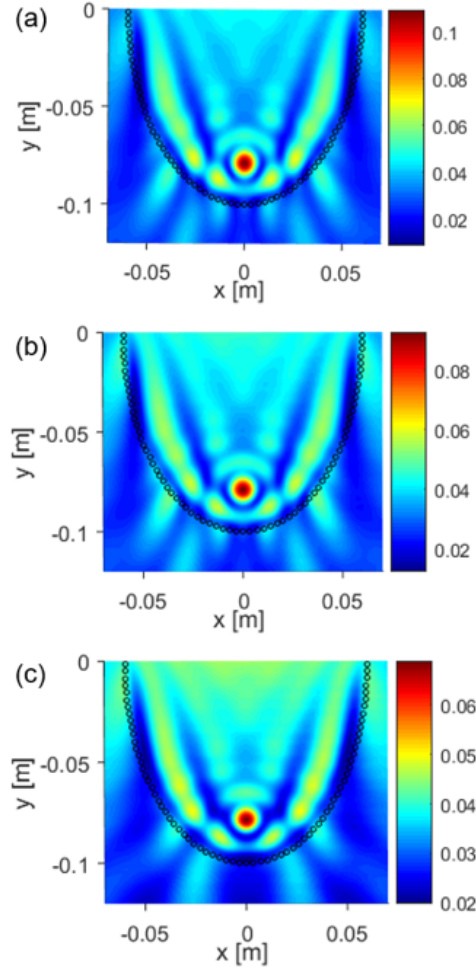
Figure 23: RMS wave fields of geometrically identical SEM configurations with spherical inclusions made of (a) tungsten (17800 kg/m^3, 360 GPa), (b) lead (11340 kg/m^3, 16.1 GPa), and (c) steel (7810 kg/m^3, 210 GPa) embedded with epoxy filling (1150 kg/m^3, 2 GPa) into the blind holes in the aluminum plate (2700 kg/m^3, 70 GPa).

3.4 Experimental Validation and Energy Harvesting Results

Experimental validation of SEM simulations is performed using the setup shown in Figure 24. The close-up in Figure 24 shows the fabricated SEM and three piezoelectric attachments

(two harvesters baseline and SEM and one source). The source piezoelectric patch was excited by 4 cycles of sinusoidal burst at desired frequencies using a function generator and a voltage amplifier. A scanning Laser Doppler Vibrometer (LDV) was used to measure the resulting wave field by recording the out-of-plane component of the velocity of the plate over a grid of points covering the mirror domain (back of the view shown in Figure 24 inset). With proper triggering of the LDV measurements, the wave field was reconstructed. The RMS values were obtained by integrating the measured response over time.
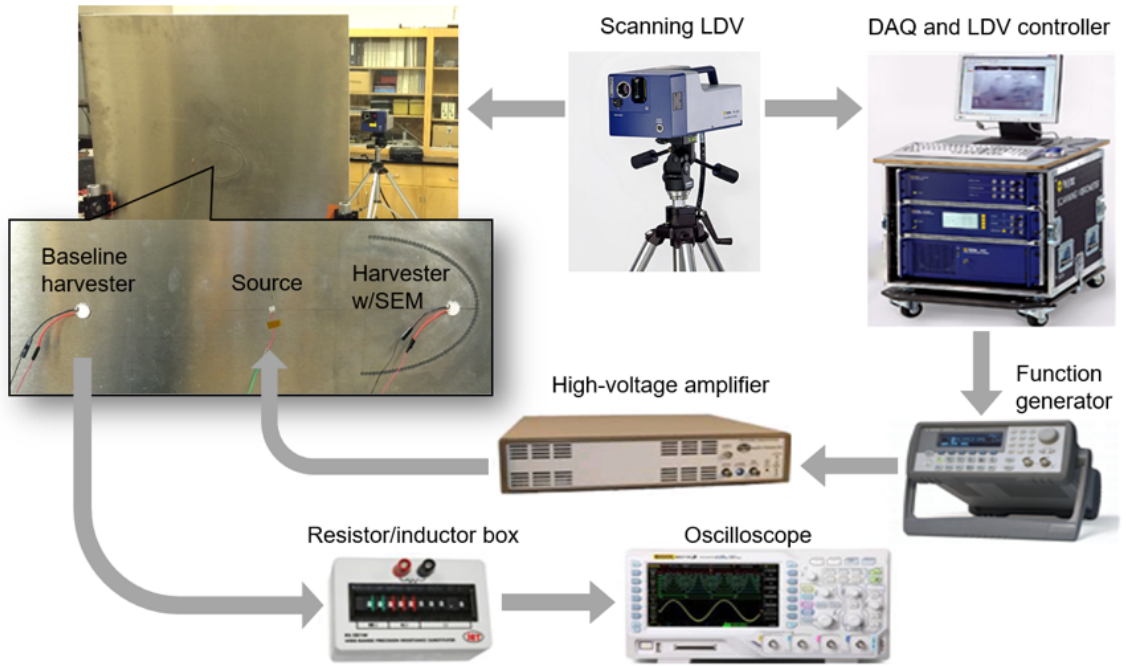
Figure 24: Experimental setup and individual components showing a close-up view of the harvester with SEM along with the point source (for excitation) at a specific distance and the base line harvester that is located at the same distance from the source on the opposite side.

3.4.1   Wave Field Validation

First, in the absence of piezoelectric energy harvester patches, overall out-of-plane velocity field was measured to explore the frequency dependence of the RMS wave field. Since the SEM in Figure 24 was designed for a specific frequency (50 kHz), side lobes are expected as one deviates from this excitation frequency. Figure 25 shows experimental RMS out-of-plane

velocity field for excitation at various frequencies (from 30-70 kHz) centered around the design frequency of 50 kHz and reveals excellent agreement with finite-element simulations. Because the wavelength criterion for ideal focusing ($d \sim \lambda$ in Figure 20(a)) is not satisfied at frequencies other than the design frequency of 50 kHz, significant side lobes are observed away from this frequency, especially at 30 kHz ($d/\lambda = 0.73$) and 70 kHz ($d/\lambda = 1.15$).
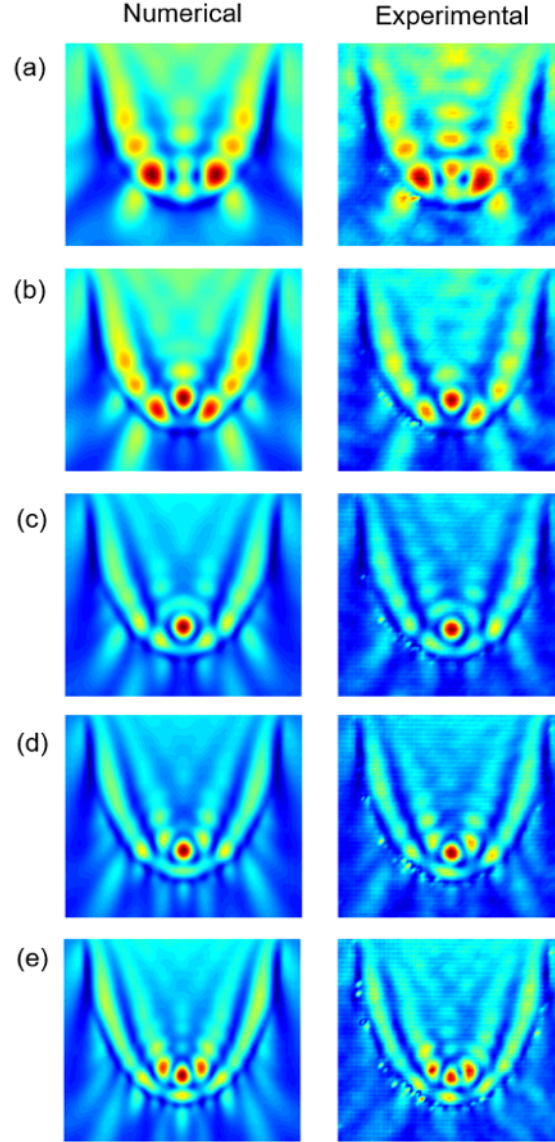
Figure 25: Numerical and experimental RMS wave fields for excitations at various frequencies: (a) 30 kHz; (b) 40 kHz; (c) 50 kHz; (d) 60 kHz; and (e) 70 kHz.

3.4.2 Energy Harvesting Results

Having successfully validated the fabricated SEM design and its focusing performance experimentally, energy harvesting performance enhancement associated with the SEM concept is discussed next. As shown in Figure 24, identical piezoelectric energy harvester disks were bonded at the focus of the SEM and also in a baseline setting at the same distance from the excitation source in the uniform plate region. These two 0.6-mm-thick piezoelectric disks with the half-wavelength diameter (for the design frequency of 50 kHz) are attached to the aluminum plate by means of a vacuum bonding technique using high-shear strength epoxy. Energy harvesting experiments were performed via resistor sweep tests by shunting the bottom and top electrodes of the piezoelectric harvesters to a decade box for range of resistive electrical loads covering the optimal conditions of both the harvester with SEM and the baseline harvester. The average power outputs of the harvesters were calculated from the voltage measurements across the resistor with an oscilloscope. For purely resistive loading, voltage response waveforms under the 1250 Ω optimal load resistance (which is roughly $1/(\omega C_p)$ where C_p is the piezoelectric capacitance) are displayed in Figure 26(a). Average power harvester from the wave packet was calculated from the RMS of the voltage waveforms as illustrated in Figure 26(c). Under the same excitation applied to both harvesters, the harvested power is increased by an order of magnitude (11 times) by focusing the elastic waves in the SEM domain as compared to the baseline case of harvesting incident plane waves using an identical piezoelectric disk. The order of magnitude increase in the power output via SEM (with tungsten inclusion) is also confirmed numerically by comparing the respective SEM finite-element simulation (Figure 23(a)) with the RMS wave field simulation for the baseline flat plate (not shown here) at the same distance from the source. The square of the RMS wave intensity at the harvester location is found to be 11 times that of the baseline case, in excellent agreement with the results of energy harvesting experiments.

The electrical power output can be improved by complex load impedance matching methods [87]. For instance, under resistive-inductive loading with the optimal resistor and inductor combination (8 kΩ and 4 mH), the harvester voltage is increased substantially (by

a factor of 4) as compared to purely resistive loading (Figure 26(c)).
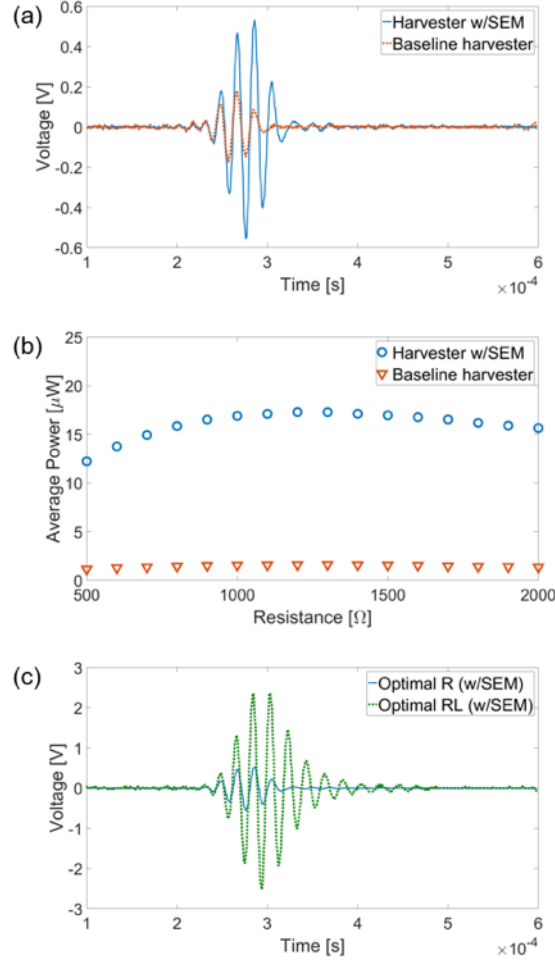
Figure 26: Samples of voltage response histories of the mirror harvester and the baseline harvester at 50 kHz (a) under optimal resistive loading (1250 Ω) and (b) under optimal resistive-inductive loading (8 kΩ, 4 mH); (c) RMS voltage and average power output performance curves in response to a 4-cycle 50 kHz sine burst excitation for a set of resistive loads revealing more than an order of magnitude increase in the harvested power with the elastic mirror.

3.5   Perforated Mirror Case

An intriguing scenario is to create a large impedance mismatch to improve reflection by using through holes instead of blind holes with metallic inclusions to form the mirror. When a one-dimensional reflection coefficient analysis is performed for an array of through holes

(as previously described with Figure 22) one obtains the solid black curve in Figure 27(a), where SEM with metallic inclusion cases are also shown for comparison. The reflection coefficient makes a peak at a relatively low frequency (around 10-15 kHz), which could be of interest to enable low-frequency mirrors to match the frequency content of typical ambient energy. However, the reflection coefficient resulting from the through hole is rather low; as a result, a perforated mirror made using through holes yields much lower intensity (at the focus point as shown in Figure 27(b)). There will always be a gain in the presence of a properly designed mirror setting (as compared to the baseline case of a flat plate); however, the gain strongly depends on the reflection coefficient of the inclusion.
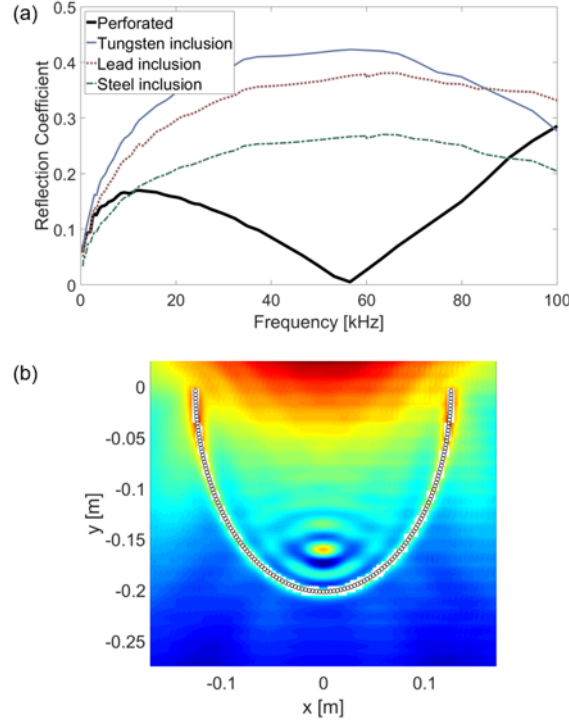
Figure 27: (a) Reflection coefficient frequency response for through hole (perforated) inclusion in a one-dimensional waveguide compared with SEM cases (previously described with Figure 22); and (b) RMS wave field for a perforated mirror at 15 kHz (which is the vicinity of optimal reflection according to (a)) yielding focusing with very low intensity (cf. Figure 23 cases of SEM).

42

3.6 Conclusions

An experimentally validated structurally-embedded mirror (SEM) design methodology is presented for enhanced elastic wave energy focusing and harvesting, among other applications that can benefit from spatially focused wave intensity. The SEM configuration proposed in this effort is enabled by inserting metallic spheres (heavier than host structure) into blind holes that form the mirror geometry in the flat plate domain [93]. The relationship between SEM geometry and wavelength is unveiled in order to eliminate or minimize the formation of side lobes near the focus so that a small-sized harvester can be used conveniently at the focus (without harvester/electrode segmentation and complex wiring to incorporate side lobes). The correlation between SEM focusing performance and the reflection coefficient of embedded spherical inclusions is shown, and the importance of inclusion-related transmission resonances is discussed (such frequencies have to be avoided for enhanced reflection). Dramatic enhancement of the harvested power by more than an order of magnitude (as compared to the baseline case) is also demonstrated experimentally by using an elliptical SEM that employs spherical tungsten inclusions in an aluminum plate. Finite-element simulations show excellent agreement with experimental measurements, validating the SEM design criterion and focusing performance.

The case of a perforated mirror was also addressed by replacing the inclusions with through holes (in the sense of mass subtraction to create a large impedance mismatch). A low-frequency, low-intensity peak was observed in the reflection coefficient of the through hole case, yielding a low gain in the focused energy. While there will always be a gain in the presence of a properly designed mirror setting (as compared to the baseline case of a flat plate), the gain strongly depends on the reflection coefficient of the inclusion. Therefore, it is suggested that a more plausible way to enable low-frequency mirrors could be to exploit bandgap formation via locally resonant metamaterials, which will be explored in Chapter 5.

Chapter IV

GRADIENT INDEX PHONONIC CRYSTAL LENSES FOR ELASTIC WAVE FOCUSING AND HARVESTING

4.1 Introduction

As an alternative to elastic mirrors presented in Chapter 3, the harvested energy can be enhanced by designing elastic lenses which focus the wave energy at a desired spot by tailoring wave propagation characteristics. Elastic lenses are designed by creating a gradient distribution of the refractive index of the unit cells (specifically PCs in this section) comprising the lens domain. To this end, a Gradient-Index Phononic Crystal Lens (GRIN-PCL), a 3D printed GRIN-PCL, and an omnidirectional Luneburg lens are designed, fabricated, and numerically and experimentally validated. Overall, the goal is to implement a metamaterial design that can focus the incident plate wave energy at a focal spot where the piezoelectric energy harvester is located to maximize the electrical power output with a small-size harvester.

4.2 Gradient-Index Phononic Crystal Lens

Gradient-Index Phononic Crystal Lens (GRIN-PCL) first proposed by Lin et al [49] was designed with solid cylinders embedded in an epoxy medium such that the refractive index along the direction transverse to the phononic wave propagation had a hyperbolic secant gradient distribution. Hence the incident waves were bent gradually toward the center axis where the refractive index was highest (or the wave speed was lowest), resulting in convergence at a focal spot. Later, focusing of the A_0 mode Lamb wave in a perforated silicon GRIN-PCL plate was demonstrated numerically by Wu et al. [99] and further explored both numerically and experimentally by Zhao et al. [103] In both studies GRIN-PCL was designed for high frequency Lamb waves on the order of 7-10 MHz.

In this section, a detailed experimental and numerical investigation of a blind hole-based GRIN-PCL structure [86, 91] and its coupling with piezoelectric transduction for

dramatically enhanced elastic wave energy harvesting is presented. First, the focusing of the A_0 Lamb wave mode in an aluminum plate is shown by implementing a GRIN-PCL with a blind hole-based unit cell design. The hyperbolic secant gradient distribution is obtained by tailoring the unit cell diameter of the blind holes. Then, the resulting GRIN-PCL is employed for performance enhancement in structure-borne elastic energy harvesting from the A_0 mode Lamb waves originating from a line source.

4.2.1 Design of the GRIN-PCL

In the existing literature, GRIN-PCLs have been demonstrated (mostly numerically) by means of material[49], diameter[40], and height[101] variations of the periodically arranged stubs, or hole size variation of the perforated plates [103, 100] or local variations of plate thickness [15]. In the present work, we extend the elastic wave GRIN-PCL concept to a blind hole crystal structure setting (rather than perforated) which is critical for practical implementations, and then we implement the design in the context of energy harvesting from elastic waves. The GRIN-PCL based on the blind hole unit cell structure of different diameters used in this work can be more advantageous as compared to complete perforation and external stubs in practical applications since mass addition (of bulky stubs) is avoided while structural integrity (unlike though hole scenarios) is better preserved.

The blind hole distribution is based on the hyperbolic secant gradient profile, which was calculated from dispersion curves. Finite element analysis (COMSOL Multiphysics) is performed to calculate band structures of A_0 mode propagating along the ΓX orientation in PCs for various filling factors ($ff = \pi d^2/4a^2$) with an aluminum plate thickness of $h = 3.175$ mm, blind hole depth of $h_b = 2.175$ mm, and unit cell size of $a = 8$ mm (as illustrated by Figure 28(a)). Figure 28(b) shows that the frequency band of the A_0 mode drops and the wave velocity decreases with increased ff at the design frequency (50 kHz). Note that this frequency is chosen merely to demonstrate and validate the concept using a GRIN-PCL setup with compact dimensions and is not intended for a specific application. As is common practice in energy harvesting, the design frequency (and therefore the resulting GRIN-PCL dimensions) would be dictated by the given excitation spectrum.
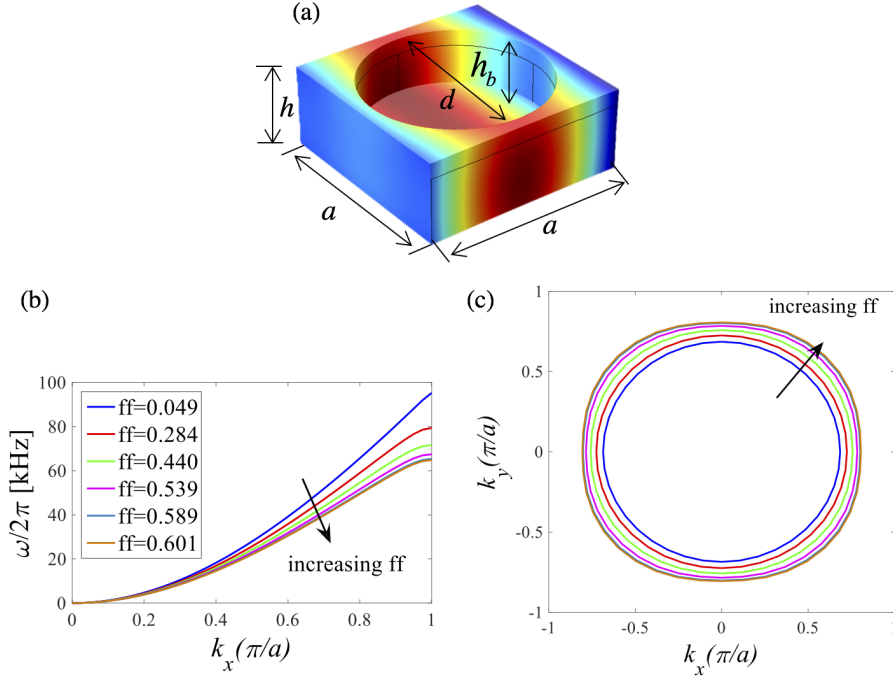
Figure 28: (a) Schematic of the square unit cell structure of the GRIN-PCL plate with blind holes; (b) Band structure of the A_0 mode for various filling factors ($ff = \pi d^2/4a^2$); (c) Equal frequency contours of the A_0 mode Lamb wave at 50 kHz.

The refractive index profile of a two dimensional, continuous GRIN medium along the transverse direction (y-axis) can be defined as [49]

$$n(y) = n_0 \mathrm{sech}(\alpha y) \tag{20}$$

where n_0 is the refractive index along the center axis and α is the gradient coefficient. For small anisotropy as displayed in Figure 28(c) and waves propagating predominantly along x-direction, the refractive index of the A_0 mode can be approximated by the refractive index along the ΓX direction as

$$n(y) = \frac{\upsilon}{\upsilon_{\Gamma X}} \tag{21}$$

where $\upsilon_{\Gamma X}$ is the phase velocity along the ΓX direction in the PC and υ is the reference phase velocity of the A_0 mode in a homogenous aluminum plate of the same thickness (evaluated at 50 kHz). Based on the concept described by Wu et al.[99], we optimized the GRIN-PCL design to obtain the refractive index profile shown in Figure 29(a). The

refractive index values were calculated as $n = [1.186, 1.178, 1.155, 1.117, 1.068, 1.010]$ for filling factor values of $ff = [0.601, 0.589, 0.539, 0.440, 0.284, 0.049]$ corresponding to 2.175 mm blind hole depth with diameter $d = [7.000, 6.930, 6.630, 5.990, 4.810, 2.000]$ mm, at $y = [0, \pm 1a, \pm 2a, \pm 3a, \pm 4a, \pm 5a]$, respectively.
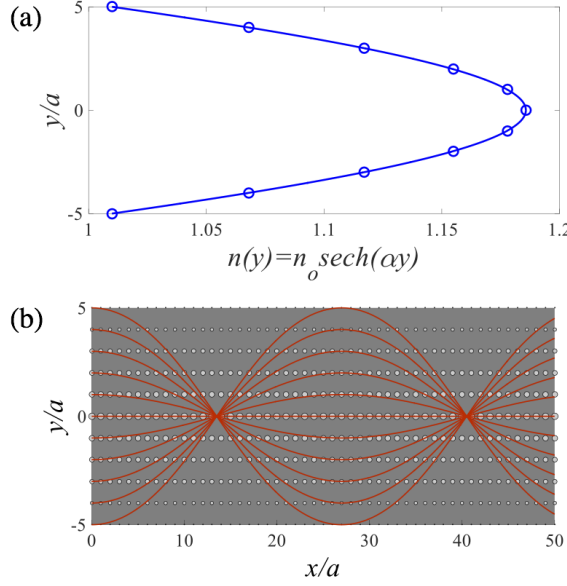
Figure 29: (a) Hyperbolic secant profile (curve fit) and the effective refractive indices for each row (circles) at 50 kHz; (b) Beam trajectory in the proposed GRIN-PCL design hosted by an aluminum plate.

From the hyperbolic secant profile, the gradient coefficient was determined as $\alpha = 0.1164$, resulting in the first focal point at $13.5a$ (i.e. $\pi/2\alpha$). As a preliminary test of the GRIN-PCL, we can also derive the beam trajectory within the GRIN-PCL using the analytical solution for the ray trajectory in a waveguide [49, 70]. Accordingly, the beam profile can be calculated from

$$y(x) = \frac{1}{\alpha} \sin^{-}1(u_0 H_f(x) + \dot{u}_0 H_a(x)) \tag{22}$$

where u_0 is the ray position and $\dot{u}_0$ is the slope of the ray at x $= 0$, and $H_f(x)$ and $H_a(x)$

are the positions of the field and axial rays, respectively.

$$H_f(x) = \cos(\alpha x)$$
$$H_a(x) = \frac{\sin(\alpha x)}{(\alpha)} \tag{23}$$

It is observed from the beam trajectory that the designed GRIN-PCL has the first focal point at $13.5a$ and second focal point at $40.5a$ as shown in Figure 29(b).

4.2.2 Numerical Simulations

After finalizing the 11 unit cell wide GRIN-PCL design with 51 unit cells along the propagation direction of the A_0 mode Lamb wave as shown in Figure 30, COMSOL Multiphysics simulations were performed in order to verify the wave focusing in the GRIN-PCL. The performance of the GRIN-PCL was simulated with time-dependent analysis. The aluminum plate was excited by a line source which acts as a boundary load with burst sinusoidal (Gaussian pulse) forcing with a center frequency of 50 kHz. As a rule of thumb in time-dependent numerical simulations, mesh size was set to satisfy 7 mesh elements per wavelength so that the wave was equally resolved in space. Using the relationship between the mesh size and time step length (a.k.a. CFL number~0.2), time stepping was set so that the optimal solution was obtained.
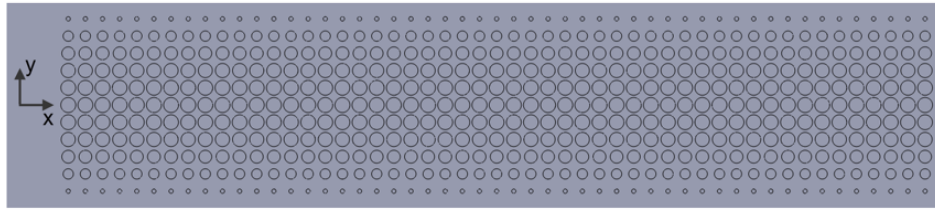
Figure 30: 11 unit cell wide GRIN-PCL design with 51 unit cells along the propagation direction of the A_0 mode Lamb wave.

Figure 31 illustrates that when the plane wave is incident upon the GRIN-PCL, the wave travels faster at the edges and slower in the center as it propagates in the lens. One can clearly observe that the plane wave beam first converges, then diverges, then converges,

and then diverges again, which agrees well with the phenomena expected for GRIN-PCL.
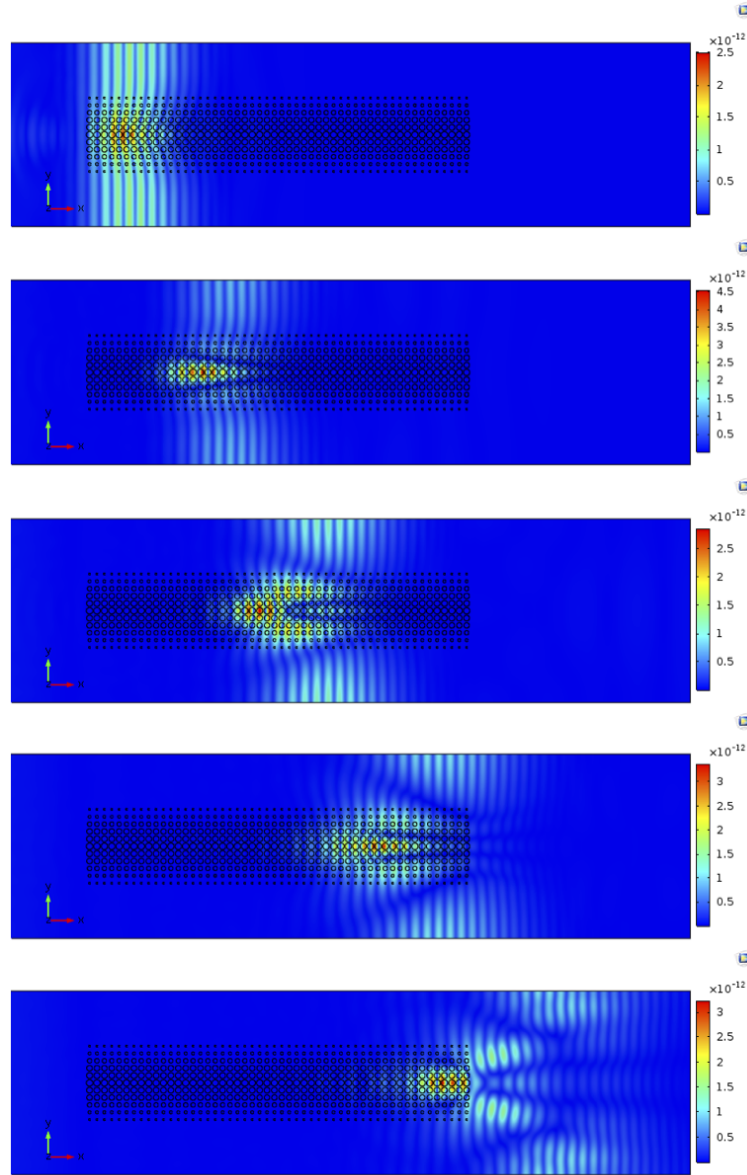
Figure 31: Simulated elastic wave propagation (from left to right) in the GRIN-PCL at 50 kHz in COMSOL Multiphysics.

Then, the root-mean-square (RMS) values were obtained by integrating the out-of-plane velocity response over time. As can be seen in Figure 32, the focal points are in agreement with the beam trajectory results.
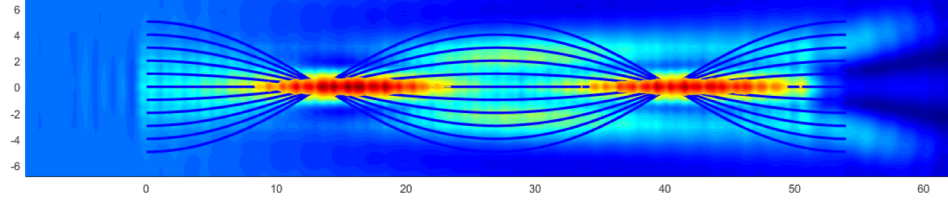
Figure 32: Comparison of the RMS wave field (COMSOL) and the beam trajectory solution.

4.2.3   Experimental Validation

In this section, wave focusing of the GRIN-PCL is first validated experimentally. Then, a piezoelectric energy harvester disk is located at the first focus and its performance is compared with the baseline case of energy harvesting without the GRIN-PCL on the uniform plate counterpart. Figure 33 shows the fabricated GRIN-PCL plate including 51 blind holes along the propagation direction of the A_0 mode Lamb waves originating from a line source. This particular size GRIN-PCL plate was chosen to show focusing and defocusing of flexural waves at two focal points. Plane wave-like wave front was generated by an array of 7 mm x 7 mm x 0.2 mm piezoelectric transducers (from STEMiNC Corp.) bonded to the aluminum plate with 8 mm spacing. These transducers were excited by 4 cycles of sinusoidal burst at desired frequencies using a function generator (Agilent 33220A) and a voltage amplifier (Trek Model PZD350). Polytec PSV-400 scanning laser vibrometer was used to measure the resulting wave field by recording the out-of-plane component of the velocity of the plate over a grid of points covering the GRIN-PCL domain in a similar setting as shown in Figure 24. With proper triggering of the laser measurements, the wave field was reconstructed.

Figure 34(a) shows experimental RMS distribution of the velocity field for excitation at various frequencies (in 30-70 kHz range) around the target (design) frequency of 50 kHz and reveals excellent agreement with the beam trajectory predictions and the numerical elastic wave simulations at the target frequency (cf. Figure 29(b) and Figure 31).

The incident wave energy is focused with the maximum intensity at $x = 13.7a$ and $x = 41.2a$ along the propagation direction in the GRIN-PCL domain, which is consistent with the first two analytical focal points evaluated at $x = 13.5a$ and $x = 40.5a$, respectively.
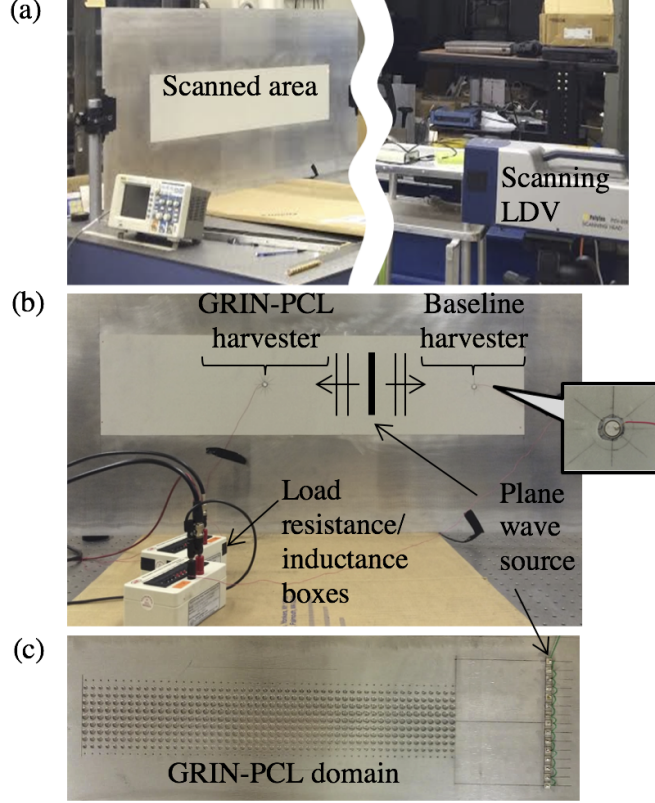
Figure 33: Experimental setup: (a) Scanning LDV is employed for out-of-plate velocity field measurement; (b) Wave propagation domain showing the plane wave source along with the two harvesters, one at the GRIN-PCL focus and the other at the same distance from the source in the flat plate domain (as a baseline) a close-up view of one of the identical harvester disks and resistance/inductance boxes are also shown; (c) Close-up view of the fabricated GRIN-PCL domain on the other face of the aluminum plate is displayed along with the plane wave source (made from a piezoelectric line array actuated in phase).

The maximum wave amplitude at the focus was measured to be 3.7 times of the amplitude near the source. Although the GRIN-PCL was designed to work at 50 kHz, frequency dependence of its focusing characteristics is investigated by performing experiments over the 30-70 kHz range as shown in Figure 34a). It is observed that the focusing neck becomes longer and the first focal points shift away from the source as the excitation frequency decreases. This can be explained by the redistribution of the refractive index of the PC layers due to the sensitivity of the gradient coefficient to frequency [100]. As illustrated in Figure 34(b), the gradient coefficient decreases for frequencies lower than the designed one resulting in a larger focal distance. Similarly, the gradient coefficient α increases with
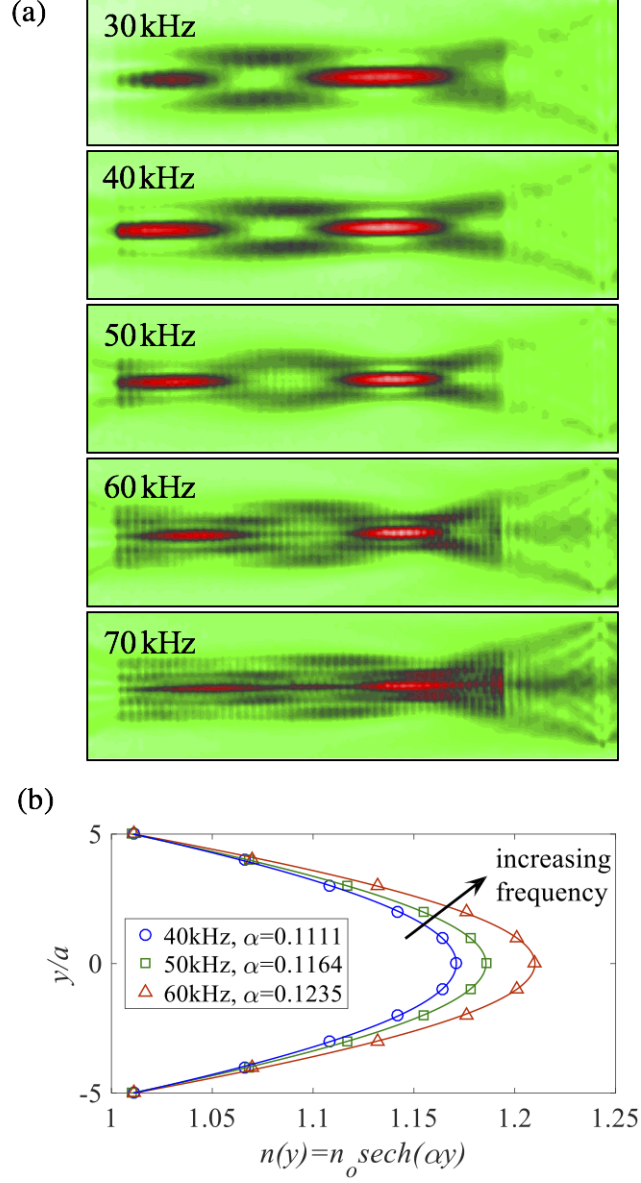
Figure 34: (a) Experimental RMS wave field for excitations at various frequencies: 30 kHz, 40 kHz, 50 kHz, 60 kHz, and 70 kHz. The first two focal points are clearly visible at $x \sim 13.5a$ and $x \sim 40.5a$ in good agreement with the beam trajectory predictions at 50 kHz; (b) Hyperbolic secant profile curves for different excitation frequencies. Note that the gradient coefficient (α) increases/decreases with increased/decreased frequency (relative to the design frequency), yielding shorter/longer focal distance.

increased frequency, resulting in a smaller focal distance. On the other hand, above 60 kHz the group velocity almost vanishes for the greatest filling factor corresponding to the central unit cells of the GRIN-PCL and the wave field may be distorted due to the dominance of the

52

evanescent waves. Instantaneous wave fields under 50 kHz sine burst excitation captured at different time instances as shown in Figure 35 further demonstrate the functionality of the GRIN-PCL, and provide information on the GRIN-PCL performance [103, 44] and harvester optimization. For example, measurements of the reflected wave fronts show that the reflections from the GRIN lens are very small (7%), so that the incident field is focused to the harvester without significant loss.
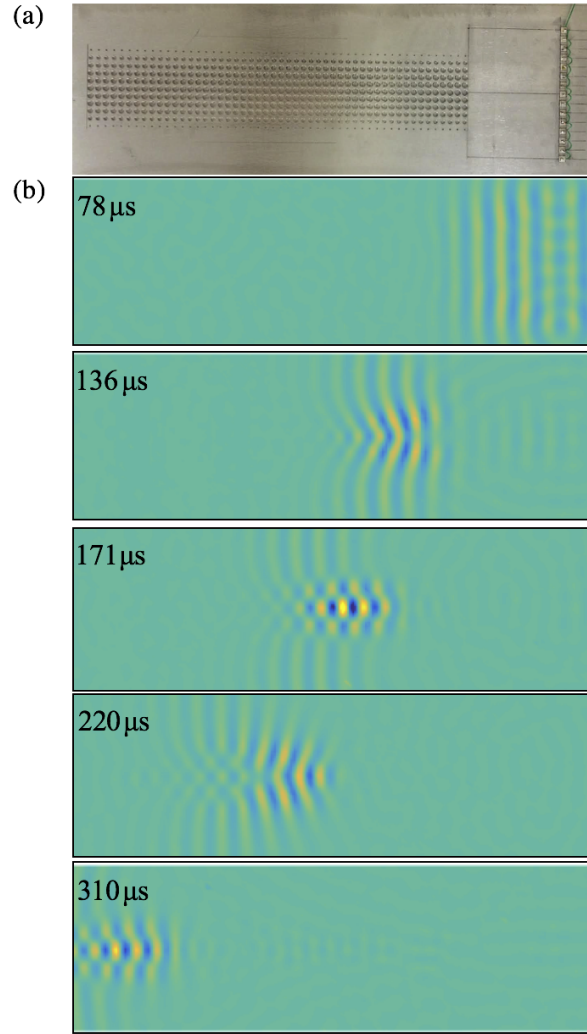
Figure 35:   (a) GRIN-PCL domain in the experimental setup and (b) out-of-plane wave field under 50 kHz burst excitation at five different time instances confirming the focusing behavior.

Having successfully validated the fabricated GRIN-PCL design and its focusing performance experimentally, energy harvesting performance enhancement associated with the GRIN concept is explored next. The harvester dimensions were determined according to wave propagation characteristics in the focal region. As shown in Figure 33(a), identical piezoelectric energy harvester disks were bonded at the first focal point in GRIN-PCL domain and also in a baseline setting at the same distance from the excitation source in the uniform plate region. The two 0.4-mm-thick piezoelectric disks (STEMINC Corp.) with the half-wavelength diameter (for the design frequency of 50 kHz) were attached to the aluminum plate by means of a vacuum bonding technique that was described elsewhere [3]. Energy harvesting experiments were performed with resistor sweep tests by shunting the bottom and top electrodes of the piezoelectric harvesters to a range of resistive electrical loads (1.8 kΩ - 4 kΩ) covering the optimal conditions of both the GRIN-PCL-enhanced harvester and the baseline harvester simultaneously. The average power outputs of the harvesters were calculated from the voltage measurements across the resistor with an oscilloscope (Tektronix TDS2024). Voltage response waveforms under the 2200 Ω optimal load resistance ($\sim 1/(\omega C_p)$) where C_p is the piezoelectric capacitance) are displayed in Figure 36(a). Harvested power was calculated from the RMS of the voltage waveforms and illustrated for the case of resistive loading in Figure 36(c). Under the same excitation applied to both harvesters, the efficiency is increased by 13 times by focusing the elastic waves in the GRIN-PCL as compared the baseline case of harvesting incident plane waves using the same piezoelectric disk as the harvester. Hence, the GRIN-PCL concept integrated with piezoelectric energy harvester results in enhanced structure-borne wave energy harvesting. Furthermore, the electrical power output can be boosted by improving the electrical circuit with complex load impedance matching methods [87]. Accordingly, under the resistive inductive loading with the optimal resistive and inductive load combination of 20 kΩ and 6 mH, the harvester voltage is increased by 5 times compared to purely resistive loading (Figure 36(b)). The harvested power can be further enhanced by properly patterned electrodes [11] matching the field distribution shown in Figure 35(b) into account.
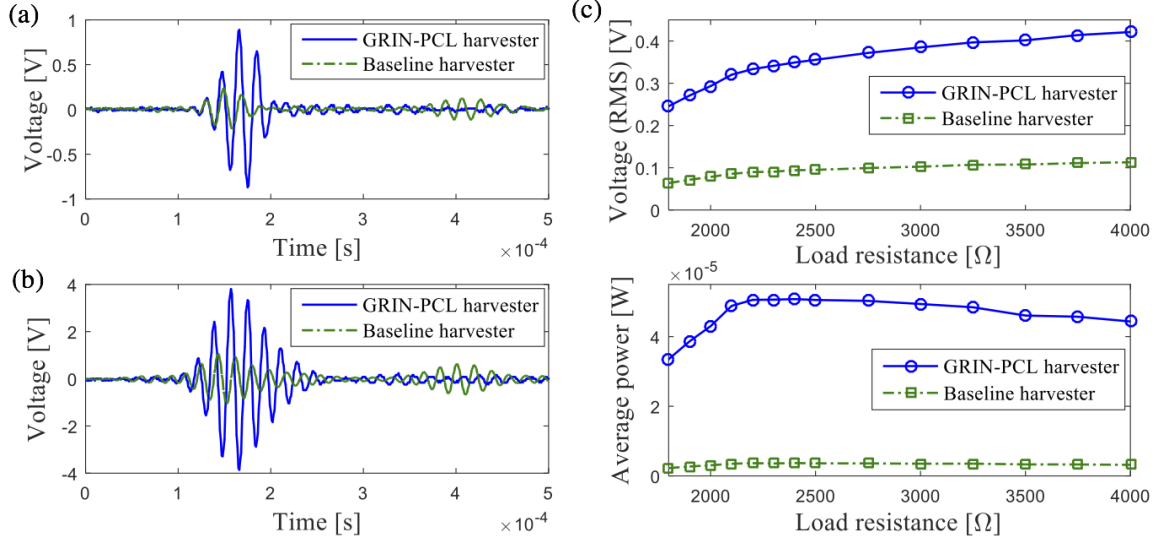
Figure 36: Samples of voltage response histories of the GRIN-PCL harvester and the baseline harvester at 50 kHz (a) under optimal resistive loading (2200 Ω) and (b) under optimal resistive-inductive loading (20 kΩ, 6 mH); (c) RMS voltage and average power output performance curves in response to a 4-cycle 50 kHz sine burst excitation for a set of resistive loads varying from 1800 Ω to 4 kΩ.

4.2.4   Conclusions

In this section, elastic wave energy harvesting is enhanced by focusing the lowest asymmetric mode Lamb wave in a GRIN-PCL. A GRIN-PCL-enhanced elastic wave energy harvester [86, 91] that is composed of blind holes as unit cells with varying diameters combined with a piezoelectric disk located at its first focal point is designed, fabricated, and both numerically and experimentally validated. The blind hole-based design of the GRIN-PCL (with unit cells of different diameters to have a hyperbolic secant profile of the refractive index) eliminates mass addition (unlike GRIN-PCLs with stub attachments) and offers better structural integrity (as compared to perforated GRIN-PCLs with through holes) while enhancing the harvested power output by an order of magnitude as compared to a baseline harvester in the uniform plate domain.

4.3   3D Printed Gradient-Index Phononic Crystal Lens

Next, novel GRIN-PCLs by 3D printing are explored which would allow more practical and light weight structures easily integrated with the host structure. The particular 3D printed

lens [92] discussed here consists of an array of nylon stubs with different heights. The fabricated lens is bonded to an aluminum plate to focus the propagating plane wave energy in the structure. The orientation and height of the stubs are determined to have a hyperbolic secant gradient distribution of refractive index similar to the GRIN-PCL concept and wave focusing is validated both numerically and experimentally. Energy harvesting performance enhancement associated with the 3D-printed lens is investigated with a piezoelectric energy harvester attached to the focus of the lens.

4.3.1 Design of the 3D Printed GRIN-PCL

The elastic properties of the plate is changed by the varying the height of 3D printed stubs in the unit cell (Figure 37(a)) in the transverse direction (y-axis) of the lens which is then periodically repeated in the propagation direction (x-axis). The orientation and thickness of the stubs are tailored according to a hyperbolic refractive index distribution given in Equation 20. The refractive index is calculated using Equation 20 from the band structure of A_0 mode in the unit cell which is obtained from unit cell simulations as shown in Figure 37(b). The bi-layer unit cell is composed of a host structure (aluminum plate) with thickness of $h = 1$ mm and 3D printed structure (PA 2200) with a base layer of $h_n = 0.8$ mm and a stub diameter of $d_s = 4.375$ mm in 5 mm unit cell (a). After obtaining the correlation between the stub heights and the refractive indices of the unit cells (Figure 37(c)) we designed the 3D printed GRIN-PCL design according to the refractive index profile at 40 kHz shown in Figure 38(a). Note that, with the 3D printing material, PA2200, used in this study the stub height is limited at 2mm because of the bandgap formation starting at 55 kHz (Figure 37(b)). In addition, the minimum stub height is limited to 0.25 mm due to the 3D printing embossed detail resolution. In the final design with 35 unit cells in the propagation direction and 11 unit cells in the transverse direction (175 mm x 55mm lens dimensions), the refractive index values were calculated as $n = [1.115, 1.111, 1.098, 1.076, 1.048, 1.013]$ for stub heights $h_s = [2, 1.96, 1.86, 1.66, 1.26, 0.25]$ mm, at $y = [0, 1a, 2a, 3a, 4a, 5a]$, respectively.
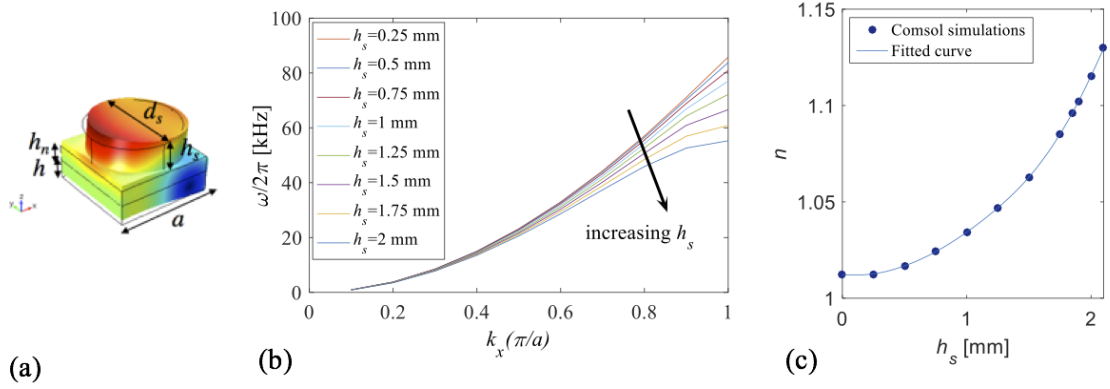
Figure 37: Unit cell (a), band structures of A_0 mode propagating along the ΓX orientation in phononic crystals (b), and correlation between the stub heights and the refractive index of the unit cells (c)

From the hyperbolic secant profile, the gradient coefficient was determined as $\alpha = 0.0893$, resulting in the first focal point at $17.6a$. It is observed from the beam trajectory that 3D GRIN-PCL design (Figure 38(b)) has the first focal point at $17.6a$ as shown in Figure 38(c).
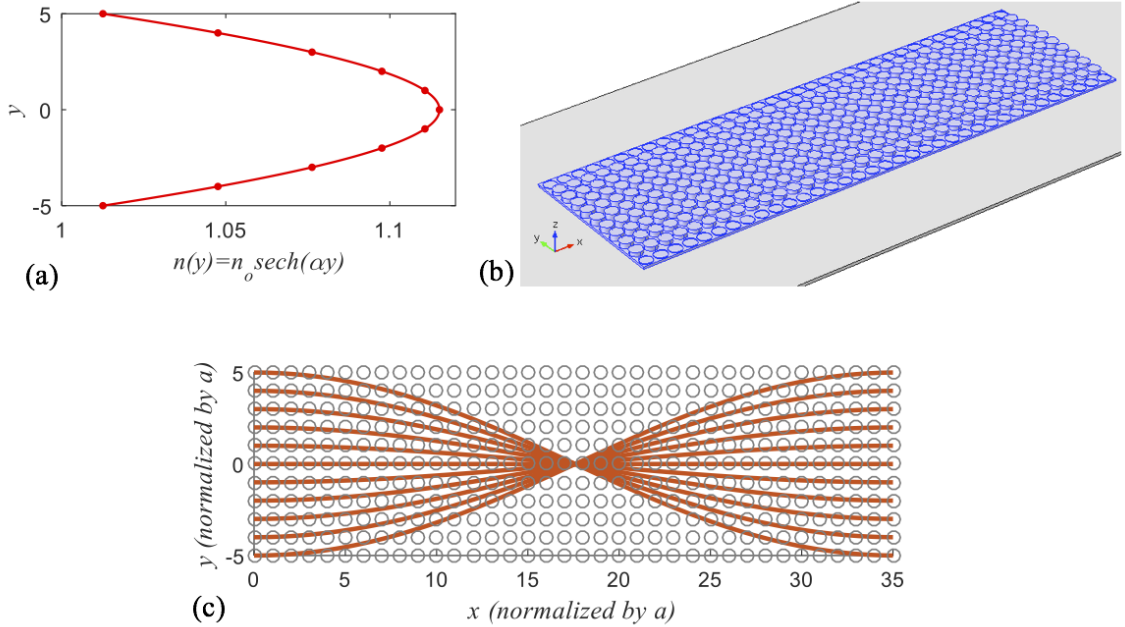
Figure 38: Hyperbolic refractive index profile of the refractive index distribution (a), 3D printed GRIN-PCL designed with varying stub heights (b) and Analytical beam trajectory (c)

4.3.2 Numerical Simulations

Time dependent analysis was performed numerically in order to obtain the out-of-plane velocity field and verify the wave focusing in the 3D printed GRIN-PCL. The aluminum plate was excited by a line source which acts as a boundary load with 7 cycles of sine burst with a Gaussian pulse envelope forcing at a center frequency of 40 kHz (at the design frequency) with 20 kHz bandwidth, hence the bandgap frequencies are avoided. Instantaneous velocity fields are shown in Figure 39 clearly exhibiting wave focusing pattern expected from a GRIN-PCL. Also, measurements of the reflected wave fronts show that the reflections from the 3D printed GRIN-PCL are small ($\sim$10%), so that the incident field is focused to the harvester without significant reflection from the lens domain.
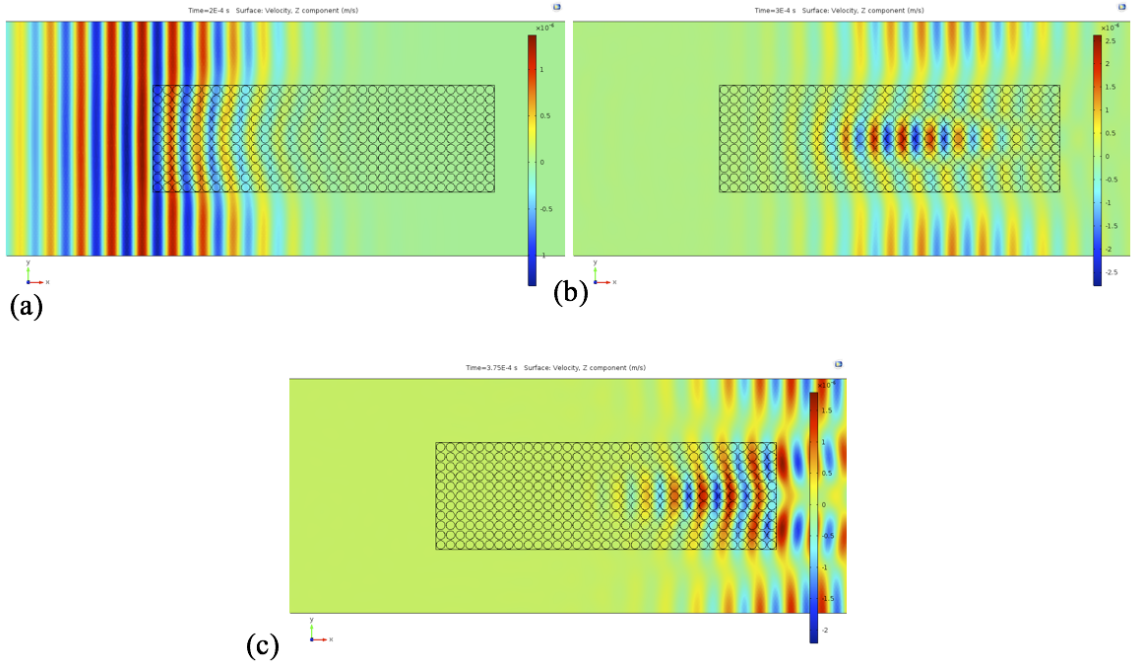

Figure 39: Numerical simulations, Instantaneous wave fields at 200 μs (a), 300 μs (b) and 375 μs (c)

Additionally, from the comparison of the RMS wave field and the analytical ray trajectories as illustrated in Figure 40, the focal point is obtained at 20.6a, which is slightly larger than the beam trajectory results at 17.6a which can be due to the diffraction effects

not completely modeled by analytical ray tracing. With the current lens design the RMS intensity of the sum of the velocity field centered in the focal point within a half-wavelength sized circular region is calculated to be 1.7 times larger than the RMS intensity of the sum of the incident wave velocity in a similar area on the pure plate domain, showing improvement due to focusing. Next, different lens designs are explored in terms of controlling the focal distance and aperture size at the same design frequency (using the same materials) and examine their effect on the wave focusing performance of the GRIN-PCL.
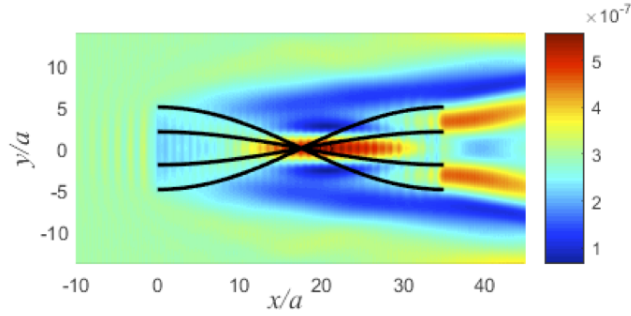
Figure 40: RMS wave field from the numerical simulations

In the first case study, we designed three different lenses by changing the stub height distributions within the same aperture size (11 unit cell wide). The refractive index distributions and their corresponding stub height variations are illustrated in Figure 41. For instance, for smaller gradient coefficients (larger focal depths) height of the center stubs are decreased to 1.52 mm and 1.1 mm while the height of the edge stubs are kept same at 0.25 mm (the refractive index variation is plotted in blue and red, respectively). According to these refractive index variations, the gradient coefficients are 0.08393, 0.0638, and 0.0446 resulting in the focal depth predictions of $17.6a$, $24.6a$ and $35.2a$. Then, these designs are simulated to assess their wave focusing performances. As illustrated in Figure 42, we observe that the focusing neck and thickness increases as the focal depth increases. Also, as the focusing neck increases we see that the maximum wave intensity point in the focal region shifts away from the predicted values due to the dispersive nature of the flexural waves (17%, 20%, 21% deviation from the beam trajectory prediction). Hence, if focusing depth

59

is critical in terms of wave focusing, then the GRIN-PCL with a larger gradient coefficient should be preferred. On the other hand, for all cases with the same lens aperture, similar wave focusing amplitudes are obtained in terms of the RMS wave field comparisons.
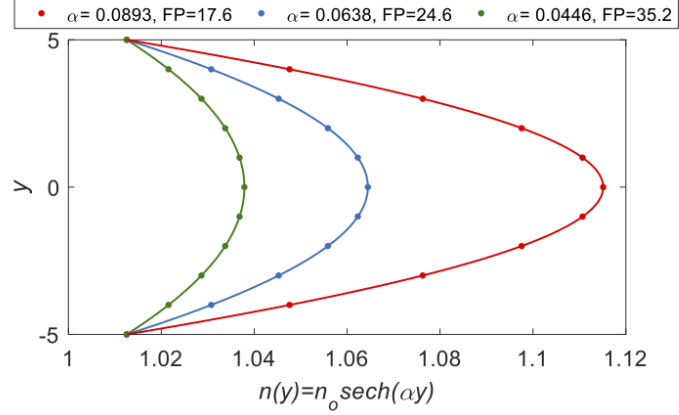
Figure 41: Refractive index distributions for 11 unit cell wide lenses with different focal points (FPs)
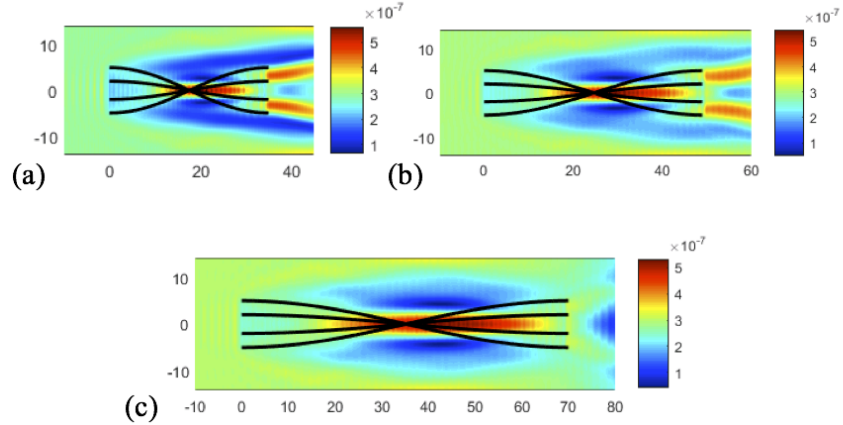
Figure 42: RMS wave fields for the 11 unit cell wide lenses with focal points at: $17.6a$ (a), $24.6a$ (b) and $35.2a$ (c)

In the second case study, we designed two GRIN-PCLs with different aperture sizes (11 and 15 unit cells wide) while keeping the same gradient coefficient hence same focal depth. The refractive index distributions of the lenses are shown in Figure 43. According to these refractive index variations, the gradient coefficient is 0.0638 resulting in the focal depth

60

prediction of 24.6a. The 11 and 15 cells wide design consists of stubs with height variations between 1.5 mm - 0.25 mm and 2 mm - 0.25 mm, respectively. Again, these designs are simulated numerically to assess their wave focusing performances. We can observe from the RMS velocity wave fields of both lenses that, as the aperture size increases, the focusing intensity increases from 1.7 to 1.9 (Figure 44). Due to the larger aperture, the focus neck and thickness decreases which results in a better agreement in terms of predicting the focal depth with the analytical beam solution (deviation from the beam trajectory prediction decreases from 20% to 12%). Hence, we can conclude that in order to have short focus necks and better wave focusing performance, the wider lenses should be preferred. Furthermore, in order to design wide aperture lenses with shorter focal depths, the variation in the refractive index should be significant; however, with PA2200 material used in this study the maximum stub height is limited to 2 mm (due to bandgap formation). Hence, different materials can be used to create wide aperture lenses with shorter focal depths which agree well with the analytical ray trajectory results. Otherwise, numerical wave field simulations gives more accurate information on the focusing results. Here we investigate the performance of different lens designs within the limitations of the 3D printing material.
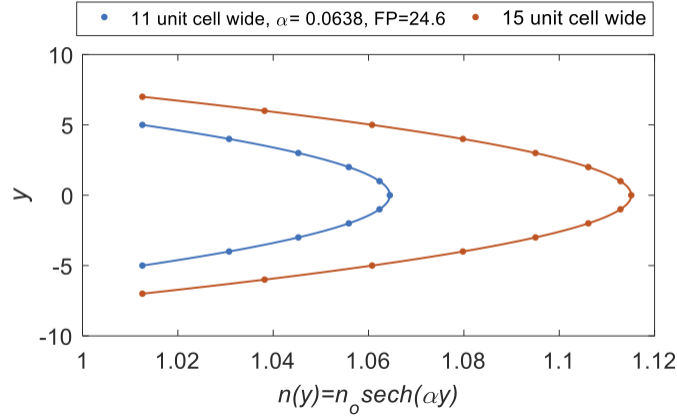
Figure 43: Refractive index distributions for 11 and 15 unit cell wide lenses with same focal points
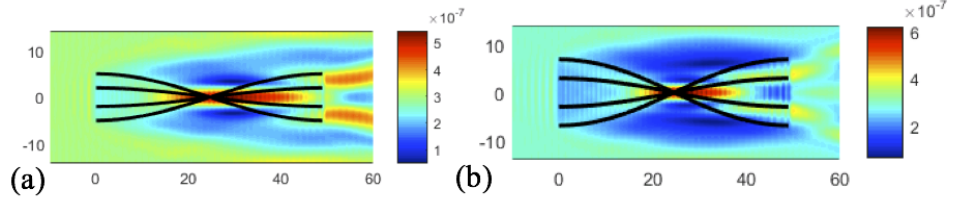
Figure 44: RMS wave fields for the 11 unit cell wide (a) and 15 unit cell wide (b) lenses

4.3.3 Experimental Validation

To demonstrate experimental feasibility of 3D printed GRIN-PCL the particular compact design (175mm x 55mm, 11 unit cells wide lens with FP at 17.6a) described in Figure 39-40 is fabricated and then bonded to the aluminum plate with vacuum bonding technique as shown in Figure 45. The experiments are performed with a scanning laser Doppler vibrometer (LDV) and the out-of-plane component of the velocity is measured over a grid of points covering the GRIN-PCL domain with a similar setup illustrated in Figure 24.

Figure 46 shows experimental RMS distribution of the velocity field at different excitation frequencies (40 - 70 kHz). We can clearly see the wave focusing in the lens domain, however the experimental wave field obtained at 40 kHz (design frequency) does not exactly match with the finite element simulations at that frequency (it rather agrees with 55 kHz). It can be due to the imperfections in the experimental setup. For instance, limitations of the 3D printing fabrication process (resolution, minimum layer thickness, etc.) and the nylon material used, resulted in a thicker base, leading to higher reflection and imperfections in the geometry of the stubs. Overall, these factors result in a different refractive index distribution as compared to the original design. Combined with the effect of thin epoxy bonding layer, the effect of this relatively thick (0.8 mm) layer and stubs on the refractive index distribution are more pronounced for the thin (1 mm) aluminum host structure.

In order to explore the energy harvesting performance enhancement capability through wave focusing in the 3D printed GRIN-PCL, identical half-wavelength piezoelectric energy harvester disks were bonded at the focal region of the lens and also in a baseline setting at the same distance from the excitation source in the uniform plate region as shown in Figure
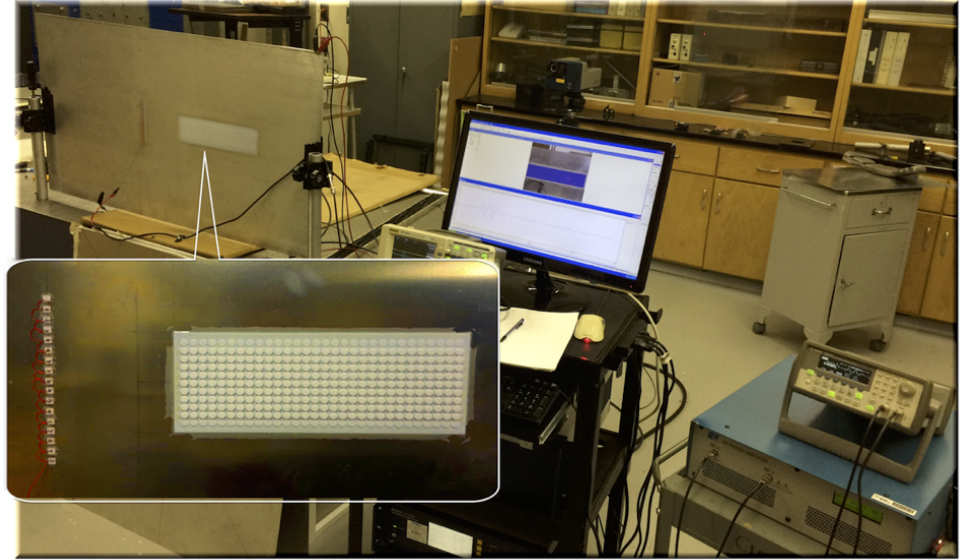
Figure 45: Experimental setup and close-up view of the 3D printed GRIN-PCL structure
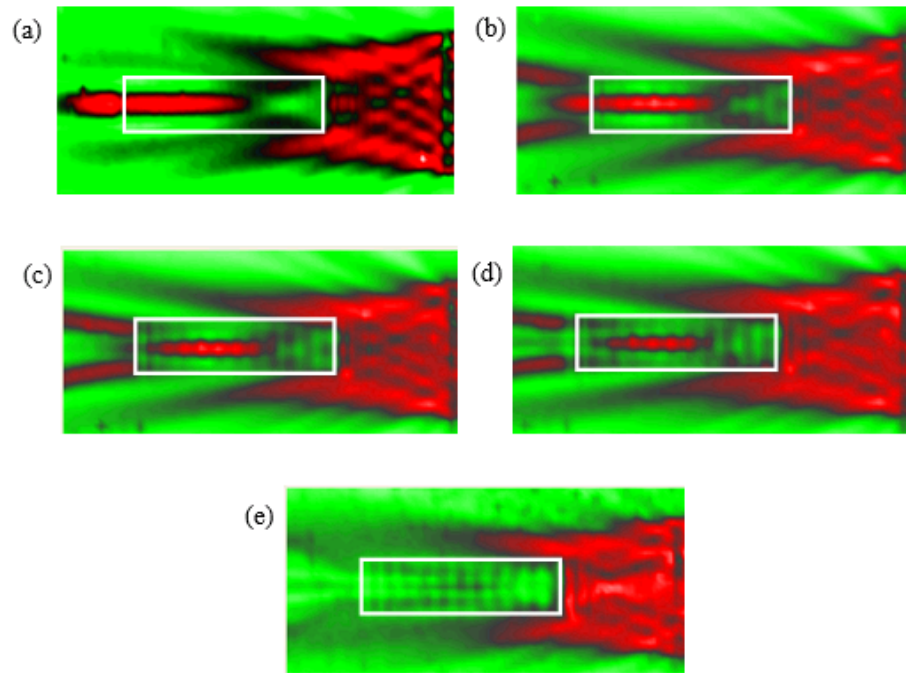
Figure 46: Experimental RMS wave fields: 40 kHz (a), 50 kHz (b), 55 kHz (c), 60 kHz (d) and 70 kHz (e)

47. Energy harvesting experiments were performed with resistor sweep tests by shunting

the bottom and top electrodes of the piezoelectric harvesters to a range of resistive electrical loads (2 kΩ - 7 kΩ) covering the optimal conditions of both the GRIN-PCL-enhanced harvester and the baseline harvester simultaneously under the plane wave excitation with 7 cycles of sine burst at 55 kHz. The voltages across the resistors are measured simultaneously with an oscilloscope (Tektronic TDS5034) and the average power outputs of the harvesters were calculated from the RMS of the voltage waveforms.
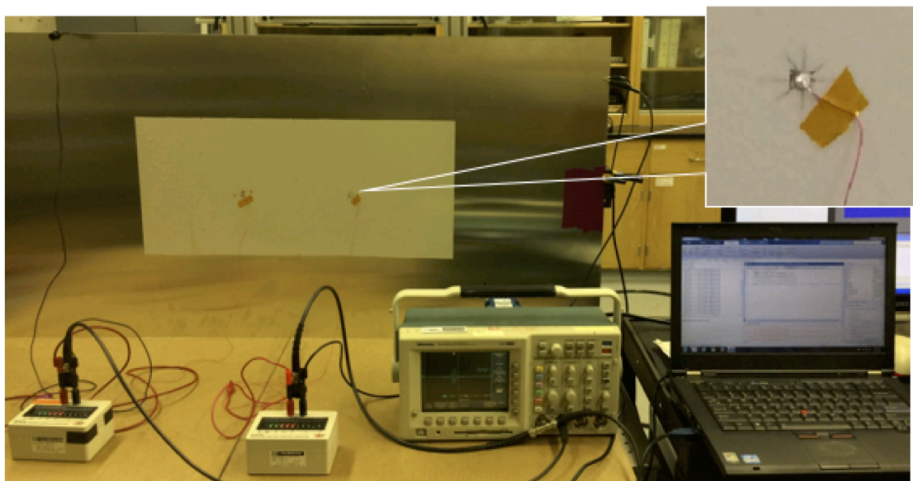
Figure 47: Experimental setup for energy harvesting

Figure 48(a) shows the measured voltage output time series for the baseline and GRIN-PCL harvesters under optimal resistive loads of 4.8 kΩ and 4.6 kΩ, respectively. According to harvested power comparison shown in Figure 48(b) and the harvested power is increased by 2.84 times by focusing the elastic waves in the 3D printed GRIN-PCL as compared to the baseline case of harvesting incident plane waves using the same piezoelectric disk as the harvester. This is in line with the estimated 1.7 fold increase in the velocity field amplitude. Hence, the 3D printed GRIN-PCL integrated with piezoelectric energy harvester results in enhanced structure-borne wave energy harvesting.
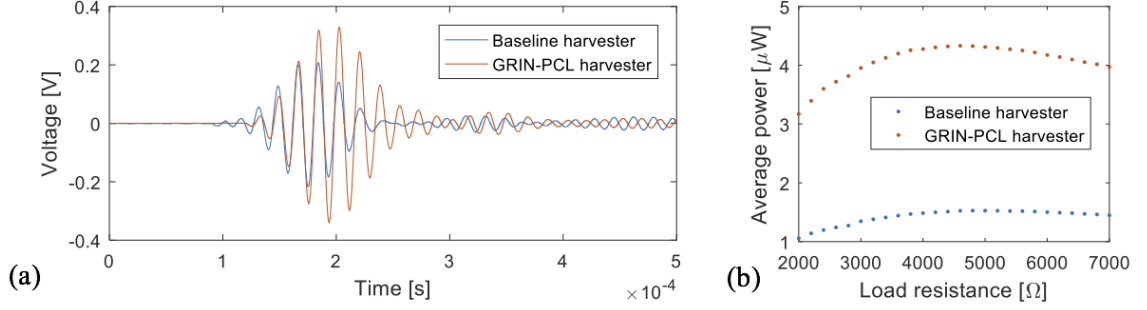
Figure 48: Voltage output under optimal resistive loading (a) and average power output (b)

4.3.4 Conclusions

In this chapter, a 3D printed GRIN-PCL [92] is studied as an alternative and more practical option for implementing conventional GRIN-PCLs as compared to perforated plates or individual stub extensions on the host structure. The proposed lens region is composed of bi-layer unit cells including the aluminum structure and the 3D printed material (PA2200) bonded to it having a hyperbolic secant profile distribution of the refractive index. The limitations of this approach is investigated for given materials used in different lens designs. The wider aperture lens focuses more energy, as expected, and gives better agreement between the beam trajectory method and the numerical wave simulations in predicting the focal distance. On the other hand, as the gradient coefficient increases within the same aperture size lenses, the focusing neck and thickness is observed to be narrower resulting in a better prediction results from the beam trajectory solution. The lens focuses A0 mode Lamb waves leading to enhanced energy harvesting. A 3D printed GRIN-PCL-based harvester is designed, fabricated, and both numerically and experimentally presented. The harvested power output is enhanced nearly 3 times as compared to a baseline harvester in the uniform plate domain. Energy harvesting can be further enhanced by designing 3D printed lenses with better focusing using different 3D printing materials and unit cells in different aperture sized lenses. In addition to avoiding major structural changes in the host structure (perforated or stubbed) for GRIN-PCL implementation, 3D printing can offer enhanced functionality by enabling embedded harvester/sensor designs.

4.4 Luneburg Lens

While the GRIN-PC lens is an extremely effective design implemented to focus propagating flexural waves (A_0 mode Lamb wave) for enhanced piezoelectric energy harvesting, its performance is very susceptible to the orientation of the incident plane wave. Hence, in this section the goal is to alleviate the directivity issue by designing and creating a Luneburg PC lens [88] due to its omnidirectional focusing characteristics. Outside the domain of energy harvesting literature, Climente et al. [15] designed a Luneburg lens for flexural plate waves by locally varying the plate thickness in the circular lens region and numerically shown that under plane wave excitation from a line source, wave focusing is observed at the opposite border of the lens with respect to the incoming wave direction. In the following, Luneburg lens concept is extended to a practical PC design with blind hole-based unit cells, experimental validations for omnidirectional focusing are provided, and energy harvesting performance enhancement is explored.

4.4.1 Design of the Luneburg Lens

The Luneburg lens proposed in this chapter is based on blind hole hexagonal unit cell structure of different diameters since it offers uniform distribution in the circular domain and can be more advantageous as compared to complete perforation and external stubs in practical applications (by better preserving structural integrity and avoiding mass addition). The orientation and size of the blind holes are based on the Luneburg gradient distribution which is calculated from dispersion curves of the A_0 mode Lamb wave. The refractive index profile of a Luneburg lens is defined as

$$n(r) = \sqrt{1 - \frac{r^2}{R_c^2}} \tag{24}$$

where n is the refractive index as a function of r, which is the radial position of the unit cell from the center, and R_c is the lens radius. The refractive index can be calculated using $\upsilon_{\Gamma M}$ (the phase velocity along the ΓM direction in the PC) in Equation 21. Band structures of A_0 mode propagating along the ΓM orientation in phononic crystals was calculated for various hole diameters (d) with an aluminum plate thickness of $h = 3.175$ mm, blind hole

depth of $h_b = 2.175$ mm, and unit cell size of $a = 8$ mm (as shown in Figure 49). Based on the Luneburg concept, the circular lens design is optimized to obtain the refractive index profile shown in Figure 49(c) at 50 kHz.
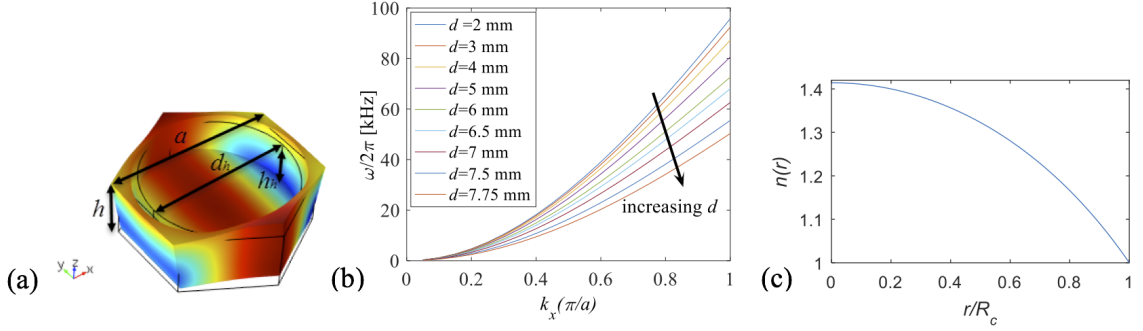
Figure 49: Unit cell (a), Band structure of the A_0 mode for various blind hole diameters (b), and Refractive index profile as a function of r (c)

The final lens design has a radius of 176 mm formed by 433 hexagonal unit cells as shown in Figure 50 where the blind-hole unit cells with the largest diameters were located in the center while the ones with the smallest diameters were located towards the edges as illustrated. This is due to the fact that the frequency band of the A_0 mode drops and the wave velocity decreases with increased d. As a result, when a plane wave is incident upon the Luneburg lens, the wavefront moves increasingly slower with vertical position as it approaches to the center of the lens and converges at the focal spot on the circular lens boundary on the opposite side.
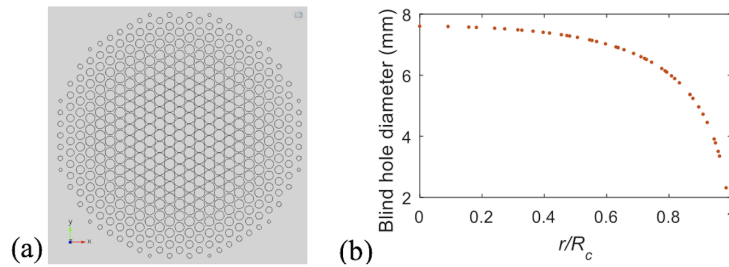
Figure 50: Luneburg lens (a) and the blind hole diameters as a function of r in accordance with the refractive index distribution (b)

67

4.4.2 Numerical Simulations

In order to validate wave focusing capability of the Luneburg lens designed using the outlined PC approach finite element simulations are performed. Figures 51(a)-(b) illustrate that when the plane wave is incident upon the Luneburg lens, the wave travels faster close to the borders and slower in the center as it propagates in the lens. Then, root-mean-square (RMS) values were obtained by integrating the measured response over time. From the instantaneous and RMS wave fields (Figure 51(c)) it is clearly seen that the plane wave focuses at the opposite border. To confirm omnidirectional focusing performance, the simulations are repeated for 30° incidence angle as shown in Figure 52. This particular angle is chosen as it represents incidence from a corner of the hexagonal approximation of the circular Luneburg lens with hexagonal unit cells. The results in Figure 52, shows that similar focusing performance is achieved even for this incidence angle, demonstrating that the desired omnidirectional characteristics is achieved.

(a)   (b)   (c)
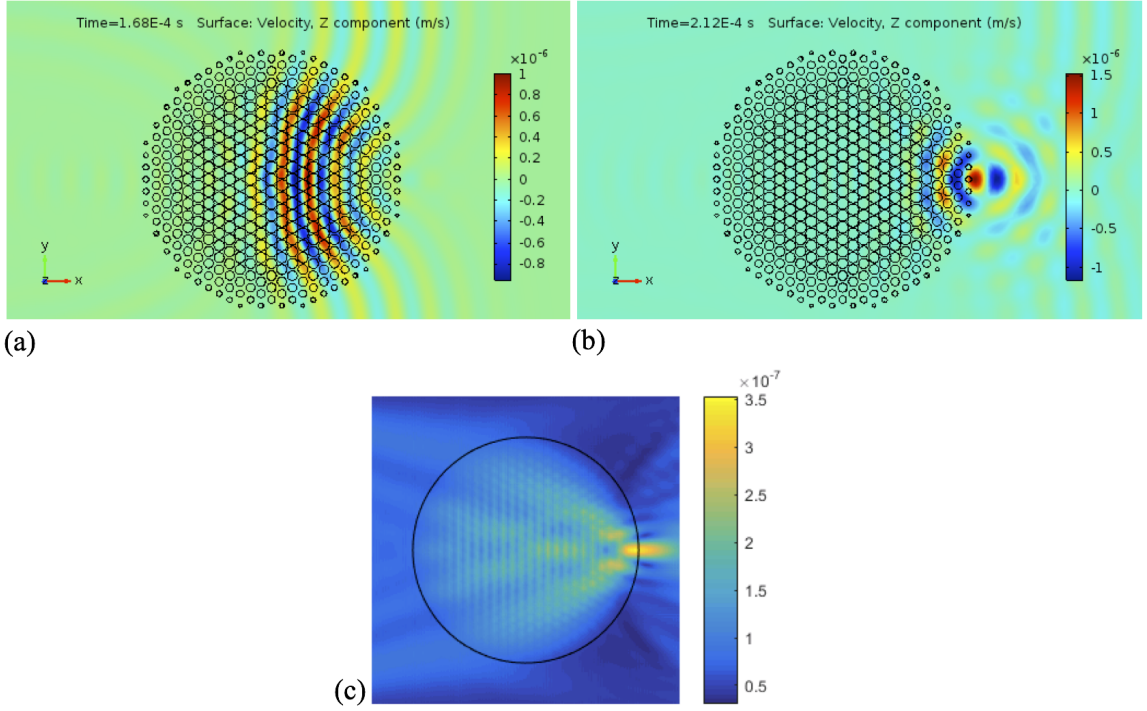
Figure 51: Numerical simulations, 0° incident wave: Instantaneous wave field at 184 μs (a) and 222 μs (b) and the RMS wave field (c)
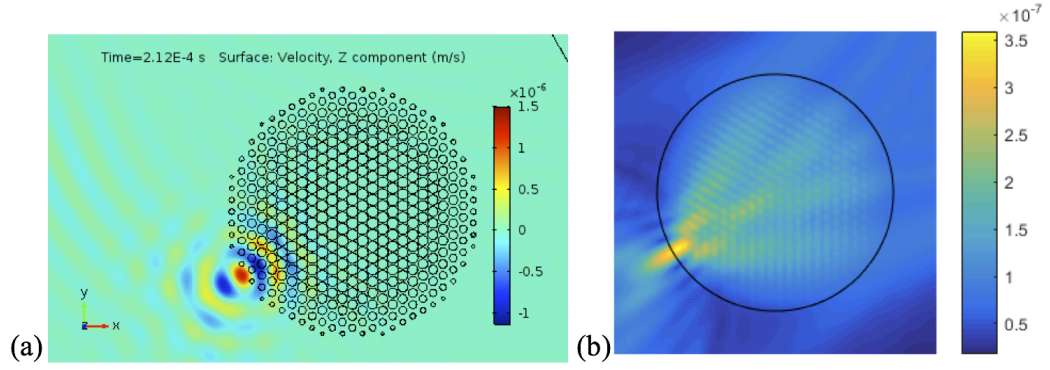
Figure 52: Numerical simulations, 30° incident wave: Instantaneous wave field at 222 μs (a) and the RMS wave field (b)

4.4.3 Experimental Validation

Figure 53 shows the fabricated Luneburg lens plate and the experimental setup. Plane wave-like wave-fronts were generated at 0° and 30° relative to the x-axis in Figure 51(a) by two arrays of piezoelectric disc transducers (5mm in diameter and 0.4mm in thickness from STEMiNC Corp.) bonded to the aluminum plate with 10 mm spacing. Using the equipment explained in Section 4.2.3, the wave field was reconstructed with proper triggering of the laser measurements.
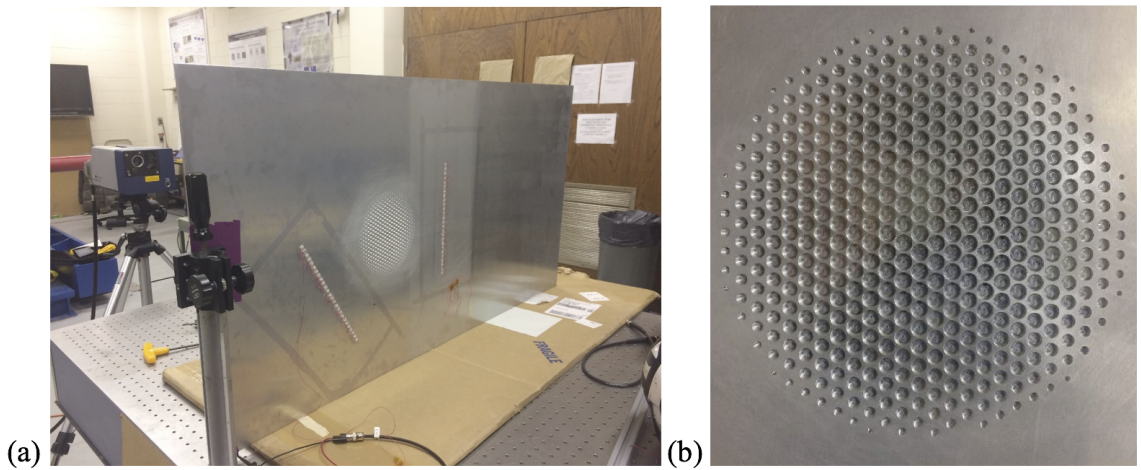
Figure 53: Experimental setup (a) and Close-up view of the fabricated Luneburg lens (b)

Figures 54(a)-(b) show the measured RMS distribution of the velocity fields for 0° and 30° respectively, and reveal excellent agreement with the numerical elastic wave simulations at the design frequency while also validating the omnidirectional aspect of focusing using the Luneburg lens: The incident plane wave always focuses at the opposite border with a very similar focusing pattern.
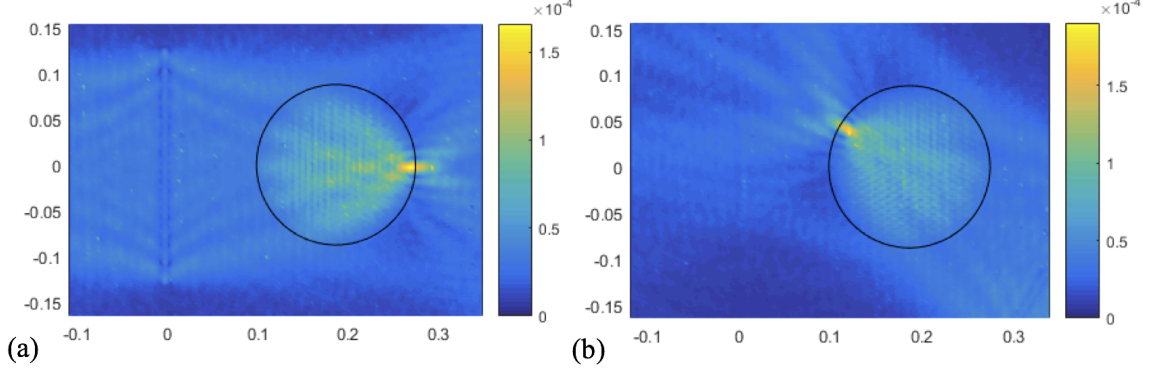
Figure 54: Experimental RMS wave fields: 0° incident wave (a) and 30° incident wave (b)

Having validated the fabricated Luneburg design and its focusing performance experimentally, omnidirectional energy harvesting performance enhancement associated with the Luneburg concept is explored next. Identical half-wavelength piezoelectric energy harvester disks were bonded at the edges of the lens domain (focal regions for 0° and 30° excitation) and also in a baseline setting at the same distance from the excitation source in the uniform plate region by means of a vacuum bonding technique (on the back side of the plate in Figure 53). Energy harvesting experiments were performed with resistor sweep tests by shunting the bottom and top electrodes of the piezoelectric harvesters to a range of resistive electrical loads (500 Ω - 2 kΩ) covering the optimal conditions of both the Luneburg-enhanced harvester and the baseline harvester simultaneously under the plane wave excitation by the 0° line array. Average power outputs of the harvesters were calculated from the voltage measurements across the resistor with an oscilloscope (Tektronix TDS2024). Similarly, the voltage output of other Luneburg-enhanced harvester is measured under the plane wave excitation by the 30° line array.

Figure 55(a) shows the measured voltage output signals under the optimal resistive loading of 1.2 kΩ and the harvested power was calculated from the RMS of the voltage waveforms (Figure 55(b)). Under the same excitation applied to both harvesters, the efficiency is increased by 13.1 times by focusing the elastic waves in the Luneburg lens as compared the baseline case of harvesting incident plane waves using the same piezoelectric disk as the harvester. Hence, the Luneburg concept integrated with piezoelectric energy harvester results in enhanced structure-borne wave energy harvesting. As expected, the 30° harvester yields comparable power levels to the 0° harvester. Hence, omnidirectional plane wave energy harvesting concept is also validated experimentally.
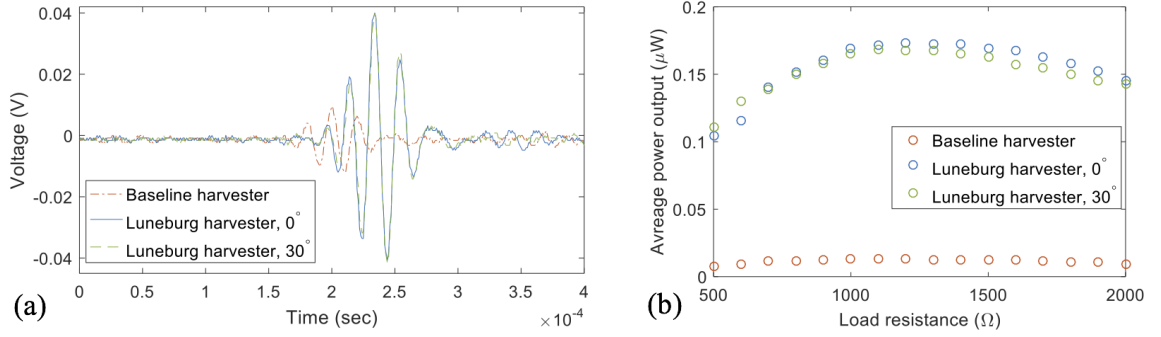
Figure 55: Measured voltage output signals under the optimal resistive loading of 1.2 kΩ (a) and harvested power (b)

4.4.4 Conclusions

In summary, a phononic crystal-based Luneburg lens employing an axisymmetric gradient index distribution is presented which offers dramatic enhancement of elastic wave energy harvesting by omnidirectional wave focusing. A Luneburg lens-based elastic wave energy harvester [88] is designed, fabricated, and numerically and experimentally validated. The omnidirectionality of the Luneburg lens is tested and validated under the excitation of two plane wave sources at 0° and 30° incident angles. The harvested power output is enhanced by an order of magnitude as compared to a baseline harvester in the uniform plate domain. Hence, the omnidirectional focusing capability of the Luneburg lens can potentially alleviate

the directional sensitivity of existing focusing concepts for enhanced elastic wave energy harvesting by locating multiple energy harvesters over the periphery of the lens domain with separately processed and rectified outputs.

Chapter V

LOW-FREQUENCY ELASTIC WAVE FOCUSING AND
HARVESTING VIA LOCALLY RESONANT METAMATERIALS

5.1 Introduction

Elastic lens and mirror concepts that have been explored to date for enhanced structure-borne wave energy harvesting are suitable for relatively high-frequency waves (e.g. tens of kHz), which are very much outside the typical ambient energy spectrum. One direct way of reducing the design frequency of such phononic crystal-based lens designs and reflectors/mirrors is to increase their size, which would yield very high dimensions to operate at ambient vibration frequencies (∼hundreds of Hz). In this chapter, locally resonant (LR) metamaterials are exploitted to enable low-frequency elastic wave focusing via LR lens and mirror concepts. LR lens is designed in a similar way to its phononic crystal counterpart by tailoring the refractive index profile of the LR unit cells. LR approach enables altering the dispersion characteristics, and thereby the phase velocity distribution, at much lower frequencies right below the local resonance frequency. Other than the local resonance frequency of the unit cells, the key factor in design is the mass ratio of the resonators to achieve the desired refractive index profile and focusing. LR mirror uses the low-frequency bandgap which is right above the local resonance frequency of the unit cells. LR unit cells arranged in the form of a parabola, for instance, makes a low-frequency LR mirror that operates in the bandgap for plane wave focusing. These LR focusing concepts can be used in vibration civil, aerospace, and mechanical systems to localize and harvest structure-borne wave energy.

5.2 Locally Resonant GRIN Lens

5.2.1 Design

In the present work, LR unit cells as shown in Figure 56(a) are employed in the design of GRIN lenses. Similar to the PC analysis, by applying periodic boundary condition to the

sides of the LR unit cell band structure in the x direction is obtained from finite element simulations. Then, the refractive index is calculated using Equation 21. In order to obtain the hyperbolic secant profile refractive index distribution given in Equation 20 the stiffness and mass of the resonators are varied proportionally, so that the bandgap formation is obtained around the same target frequency for all unit cells. For instance, for the following unit cell parameters: aluminum plate thickness $h = 2$ mm, acrylic plastic pillar radius r_p $= 2.5$ mm and height $h_p = 15$ mm, tip mass $m = 6.8$ g and unit cell size $a = 25$ mm, the bandgap is expected to around 554 Hz (which is obtained from modal analysis on the resonator portion by applying a fixed boundary condition on the base surface of the pillar). Note that, from the analytical calculations by solving the root of the following characteristic equation (continuous rod model with a tip mass attached), the first resonant frequency is obtained at 567 Hz, which verifies the numerical simulations with a 2.2 % difference.

$$1 + cos\lambda_n cosh\lambda_n + \frac{\lambda_n m}{\rho A h_p}(cos\lambda_n sinh\lambda_n - sin\lambda_n cosh\lambda_n) = 0$$

$$\omega_n = \lambda_n^2 \sqrt{\frac{EI}{\rho A h_p^4}} \tag{25}$$

where ω_n is the nth resonant frequency, λ_n is the nth root of the characteristic equation, m is the tip mass, ρ is the density, EI is the flexural stiffness, A is the cross-sectional area and h_p is the height of the pillar.

In the unit cell simulations, it is seen that the bandgap formation starts at 523 Hz for the given parameters as shown in Figure 56(b). As the tip mass and the pillar radius are increased, the bandgap becomes wider and the phase velocity decreases (Figure 56(c)), as expected [82, 86].

Then, the refractive index is calculated at 400 Hz which is set as the design frequency for the GRIN lens by avoiding the bandgap frequencies where reflections are high as will be discussed in Section 5.3. Figure 57(a) shows the refractive index distribution for the current LR lens design obtained with the variation in the pillar radius and tip mass. Based on the GRIN concept, the LR lens design is optimized to obtain the refractive index profile shown in Figure 57(a). The refractive index values were calculated as n=[1.86, 1.82, 1.71, 1.55. 1.36, 1.17] for tip mass of m=[13.6, 12.8, 10.5, 7.4, 4.3, 1.7] g and pillar radius of r_c=[3,
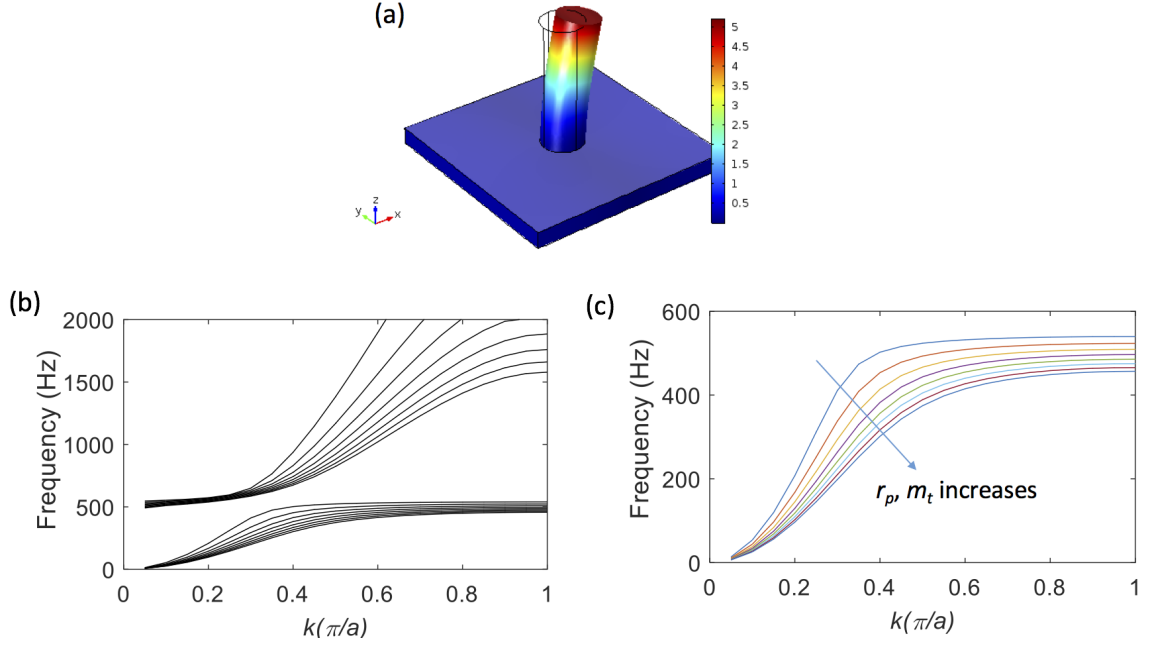
Figure 56: (a) Schematic of the LR unit cell structure; (b) Band structure and (c) first band of the A_0 mode for various mass ratios.

2.9, 2.8, 2.6, 2.2, 1.8] mm corresponding to pillar height of 15mm, at $y=[0, 1a, 2a, 3a, 4a, 5a]$, respectively. The gradient coefficient was determined as $\alpha=0.213$, resulting in the first focal point at 7.5 a (i.e. $\pi/2\alpha$) which can be observed from the analytically obtained beam trajectory shown in Figure 57(b).
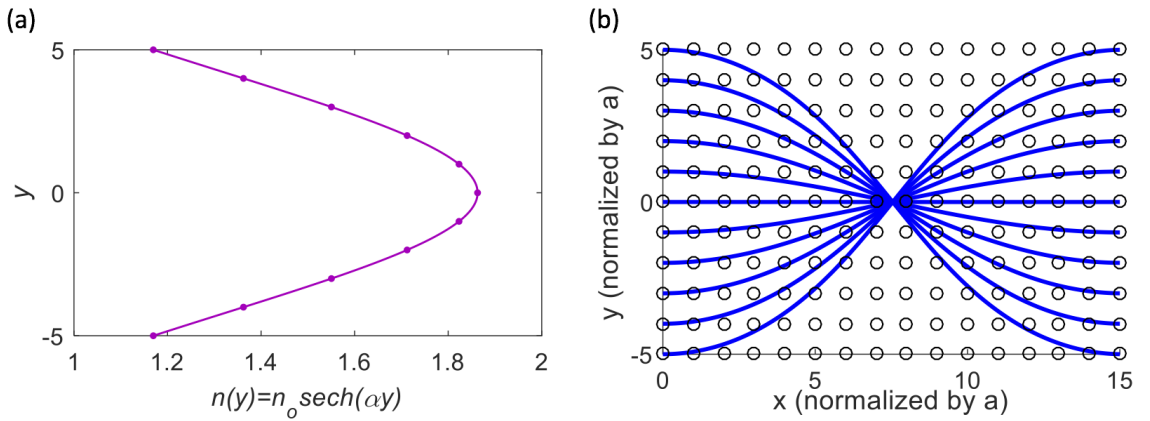
Figure 57: (a) Hyperbolic secant profile (curve fit) and the effective refractive indices for each row (dots) at 400 Hz, (b) Beam trajectory in the proposed LR lens design hosted by an aluminum plate.

5.2.2 Numerical Simulations

Time dependent analysis in COMSOL Multiphysics were performed in order to obtain the velocity field and verify the wave focusing in the LR lens. The aluminum plate was excited by a line source which acts as a boundary load with 10 cycles of sine burst with a Gaussian pulse envelope forcing at a center frequency of 400 Hz (at the design frequency) with 200 Hz bandwidth. We can see from the instantaneous velocity fields shown in Figure 58 that when the plane wave is incident upon the LR GRIN lens, the wave travels faster at the edges and slower in the center as it propagates in the lens. The converging and diverging pattern of the plane wave observed agrees well with the phenomena GRIN-PCL focusing pattern explained in Chapter 4. Note that, the wavelength of the waves propagating in an 2 mm aluminum plate at 400 Hz is 220 mm and wave focusing is achieved through the LR lens composed of subwavelength periodic LR structures with 25 mm unit cell dimensions.

Figure 59(a) shows the RMS (root-mean-square) velocity field obtained by integrating the response over time. In addition to the clear focusing pattern, the RMS wave field agrees well with the analytical ray trajectories resulting in a focal point at 7.5 a.

5.2.3 Conclusions

In summary, a LR GRIN lens is designed and numerically analyzed for low frequency A_0 mode Lamb wave focusing. The design is composed of LR unit cells with resonators targeted to create a bandgap around 550 Hz. By tailoring the dispersion curves right below the bandgap, gradient distribution is obtained by employing local resonators with different mass ratios (targeting the same local resonance frequency). The numerical simulations performed at 400 Hz shows that wave focusing is achieved with the LR GRIN lens consisting subwavelength structures ($\sim \lambda/9$) which is very promising towards enabling enhanced energy harvesting at low frequency region with small sized lenses (compared to GRIN-PCLs).
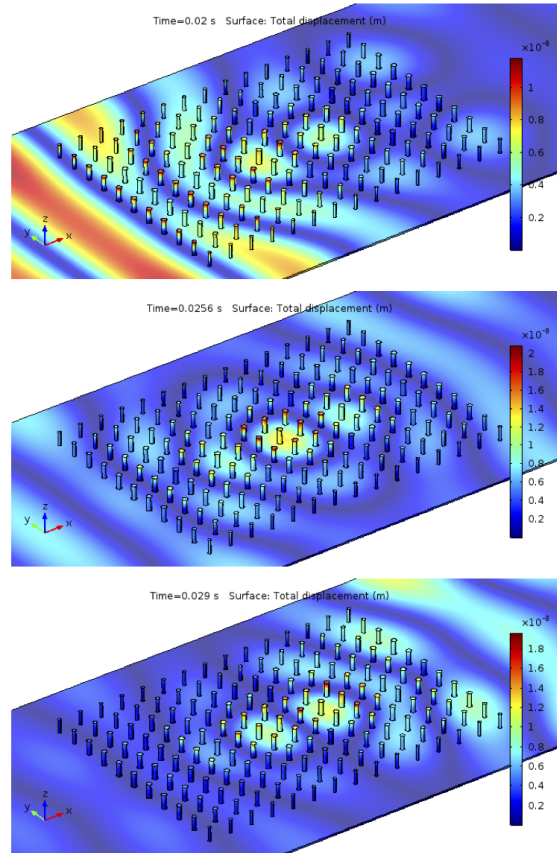
Figure 58: Simulated elastic wave propagation (from left to right) in the LR lens at 400 Hz in COMSOL Multiphysics.
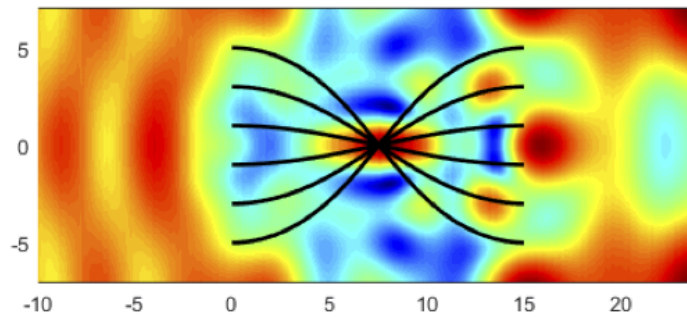
Figure 59: RMS wave field

5.3 Bandgap-based Elastic Mirror

5.3.1 Design

LR mirror concept is based on the low-frequency bandgap which is right above the local resonance frequency of the unit cells. In this work, the LR mirror is designed with LR unit cells arranged in the form of a parabola creating a low-frequency LR mirror that operates in the bandgap for plane wave focusing. Figure 60 shows the band structure of the LR unit cell with an aluminum plate thickness of $h=1$ mm, acrylic plastic pillar radius of $r_p = 3.5$ mm and height of $h_p = 15$ mm, tip mass of $m = 27$ g and unit cell size of $a = 20$ mm. The A_0 mode Lamb waves propagating in the plate is coupled with the shear oscillations of the resonator resulting in a bandgap formation between 283 Hz and 414 Hz. In order to fully utilize this bandgap in which propagation of elastic waves becomes forbidden for any incident angle, the design frequency is set to 350 Hz.
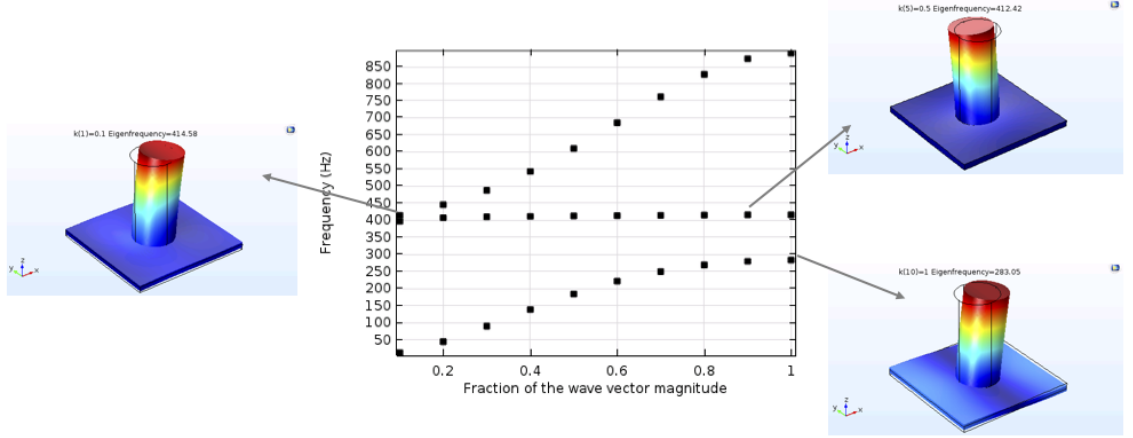
Figure 60: Band structure of the A_0 mode for the LR unit cell in the elastic mirror design.

In order to investigate the A_0 mode Lamb wave reflection at the design frequency (350 Hz), finite-element simulations are performed in an aluminum waveguide including 15 LR unit cells. This structure is periodic in the lateral dimension (which is equal to the unit cell size 20 mm), essentially simulating the reflection of a plane elastic wave incident in a laterally infinite plate. Figure 61(a) shows the incident and reflected waves and their corresponding frequency content. The reflection coefficient is almost 1 inside the band gap

78

frequencies which is a desired condition for elastic mirror designs. Also, one can observe in Figure 61(b) that the LR unit cells does not transmit the incident wave propagating in the waveguide.
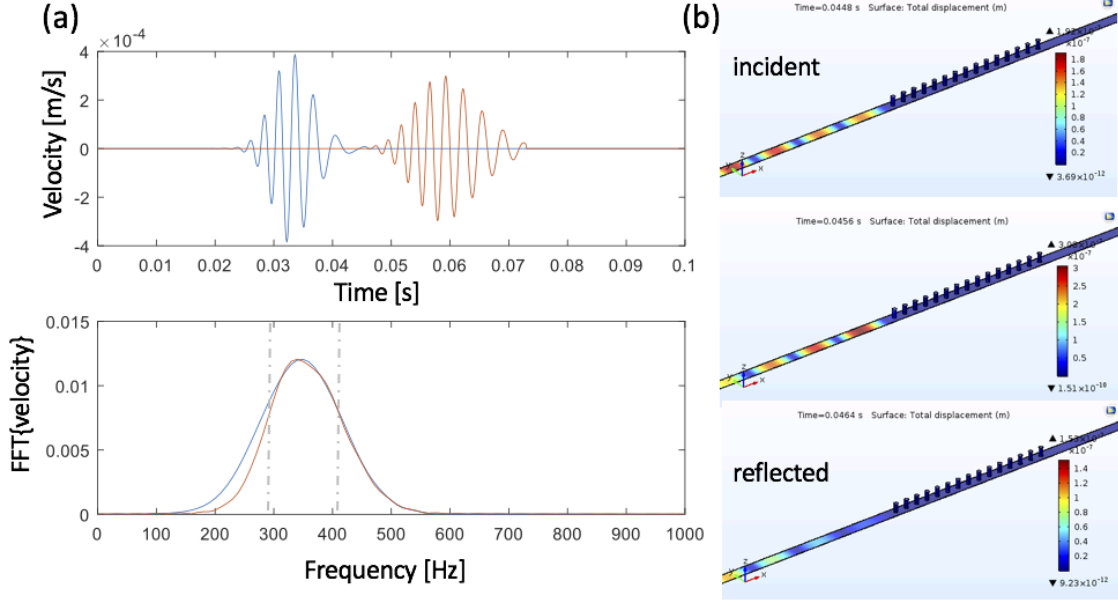
Figure 61: (a) Wave reflection from the LR unit cell array under excitations at 350 Hz center frequency and its frequency content and (b) instantaneous wave propagation in the aluminum waveguide.

Furthermore, the same waveguide is simulated under 10 cycles of tone-burst signal with a center frequency at 250 Hz. As can be seen in Figure 62 below the bandgap less reflections occur and LR unit cell array lets transmission of waves. Hence, the design frequency set to 350 Hz is a good selection for this case with the given unit cell parameters.

Next, the parabolic mirror geometry is constructed using the design methodology developed in Section 3.2. According to this recipe $(d \sim \lambda)$ for the reduced side lobes the focal distance is defined at the wavelength which is 165 mm for waves propagating at 350 Hz. The mirror is composed of three rows of LR arrays which are spaced at the unit cell distance of 20 mm from each other (Figure 63). Note that, the reflection coefficient is calculated as 0.94 in the one dimensional wave simulations with three unit cells.
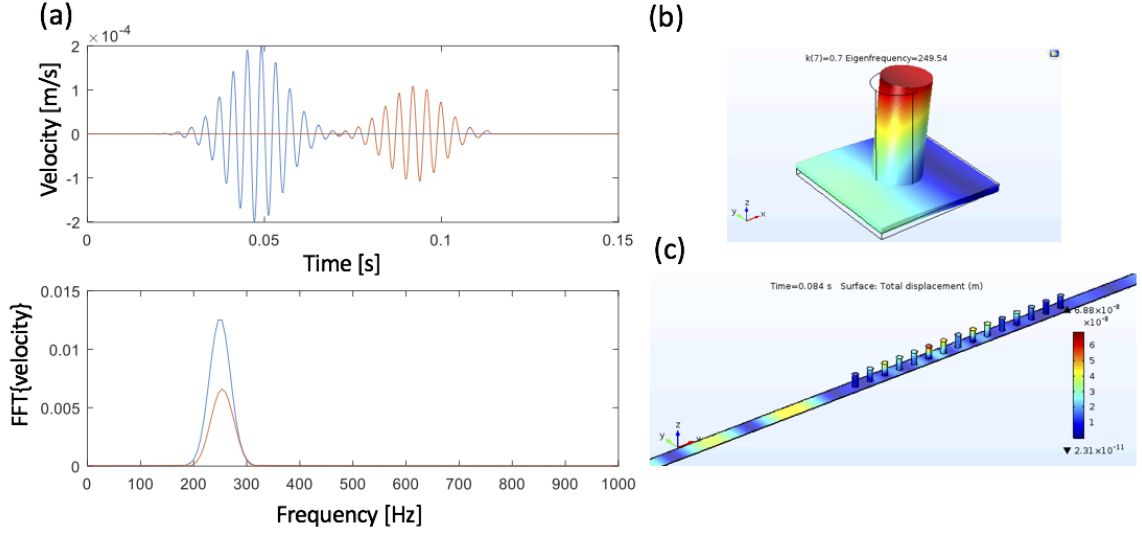
Figure 62: (a) Wave reflection from the LR unit cell array under excitations at 250 Hz center frequency and its frequency content; (b) Unit cell deformation at 250 Hz and (c) instantaneous wave propagation in the aluminum waveguide.
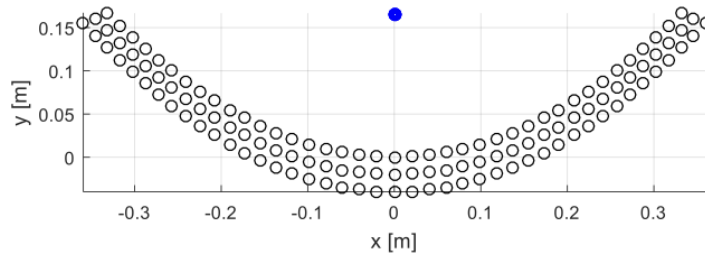
Figure 63: Bangap-based mirror design with 3 rows of LR unit cells.

5.3.2 Numerical Simulations

After finalizing the design, finite element simulations were performed. The aluminum plate was excited by a line source which acts as a boundary load with 10 cycles of sine burst with a Gaussian pulse window at a center frequency of 350 Hz. Low reflection boundary condition is applied at the sides. The RMS wave field calculated from the out-of-plane velocity response shown in Figure 64 shows wave focusing in the bandgap-based mirror clearly. In addition, the focus of the elastic mirror is in perfect agreement with the design.
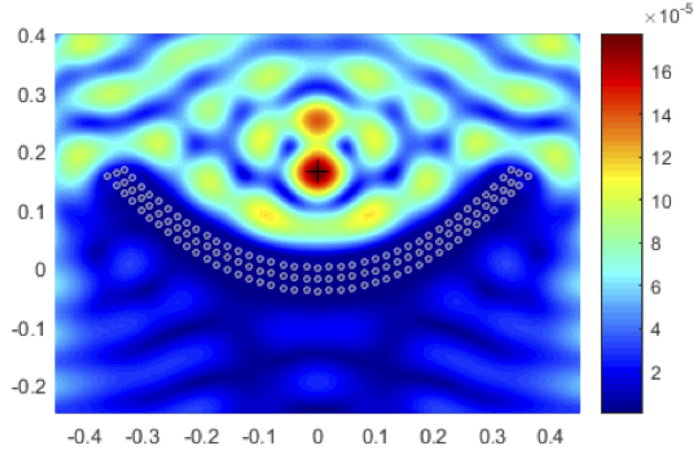
Figure 64: RMS wave field of the three rows mirror domain under plane wave excitation with a center frequency at 350 Hz.

Furthermore, mirror design is also investigated by employing a single row of LR unit cells. Wave focusing is again clearly seen in the RMS wave field shown in Figure 65. From the reflection analysis through one dimensional wave simulations with a single unit cell, the reflection coefficient is calculated as 0.93 (similar analysis as shown in Figure 61). It is seen that the single resonator creates a large impedance mismatch around the resonance frequency resulting in high reflection coefficient. Hence, the reflection analysis supports the wave focusing behavior in the mirror domain with a single row of local resonators.

5.3.3 Conclusions

In conclusion, a novel elastic mirror targeting low frequency wave focusing is designed and numerically tested. The mirror design is based on the LR unit cells and utilizes the bangap property of the unit cells resulting in high wave reflection hence good focusing performance. With these LR unit cells it is also shown that the reflection coefficient decreases below the bandgap frequencies. With the parabolic mirror design with 3 rows of LR arrays, A_0 mode Lamb wave focusing is achieved at the focus of the mirror. Furthermore, due to the locally resonating behavior of the mirror elements, a single row configuration also shown to focus waves in the mirror domain. Especially, locally resonant elastic mirror concept is important for enabling wave focusing in low frequency regime (under kHz values) which is beneficial

towards energy harvesting applications in various engineering systems.
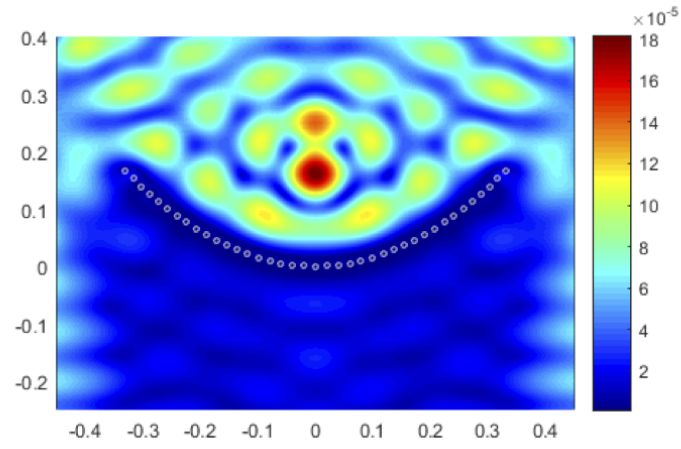
Figure 65: RMS wave field of the single row mirror domain under plane wave excitation with a center frequency at 350 Hz.

Chapter VI

CONCLUSIONS, CONTRIBUTIONS, AND FUTURE WORK

6.1 Summary and Conclusions

This research studies the harvesting of structure-borne elastic waves via piezoelectric transduction and enhancing the harvested elastic wave energy through metamaterial concepts. Overall this research provides electroelastic models and novel approaches to efficient elastic wave energy harvesting in one-dimensional and two-dimensional structures. Beyond enhanced energy harvesting, ramifications of this work range from MEMS implementation to 3D printed platforms for structural integration in sensing applications and nondestructive testing.

6.1.1 Structure-Borne Propagating Wave Energy Harvesting

An analytical framework is provided for the harvesting of one-dimensional bending waves propagating in infinite and semi-infinite beams. The electroelastic model is developed which accounts for piezoelectric structure and complex electrical load and is based on the wave equation solution and the piezoelectric constitutive relations coupled in the equilibrium and compatibility conditions at the harvester boundaries and the electrical circuit equation. Both electrical to mechanical and mechanical to electrical coupling problems are simultaneously solved yielding the amplitudes of the traveling waves and the voltage response of the harvester. Hence, with this model incident wave energy is transformed into usable electricity while minimizing the traveling waves reflected and transmitted from the harvester domain. The model is used to obtain the time averaged power flow in the beam and the time-averaged electrical power flowing to the harvester as well as the efficiency of the harvester.

Three case studies are presented to explore wavelength matching, resistive and resistive-inductive circuits, and performance enhancement. In a basic harvesting implementation with resistive only loading the maximum efficiency is obtained as 4.5% when the piezoelectric

83

patch length is $\sim \lambda/2$. At higher frequencies where the patch length is larger than the wavelength, only the mechanical energy in the last $\lambda/2$ length of the patch is efficiently converted to electrical domain, similar to the reduced coupling coefficient in higher order modes of piezoelectric resonators [42]. Hence, once the frequency range for harvesting is determined, harvester dimensions can be chosen to work efficiently at those frequencies as long as the resistor value is also chosen optimally. On the other hand, under optimal resistive-inductive loading, patch length becomes independent of the frequency, which means that high conversion efficiencies can be obtained with small piezo patches by adjusting electrical load except for a narrow region around patch length$\sim \lambda$ due to phase cancellation. A substantial performance enhancement is observed in ideal conditions by resistive-inductive loading as compared to the resistive loading case with 4.5% to 50% improvement in the maximum efficiency over a wide frequency range. It is noted that this maximum conversion efficiency is limited to 50%, as expected from a passive, reciprocal 3-port device with one conjugate matched port [65]. In the harvesting problem, the impedance matched port is the piezoelectric patch terminals and the mechanical port terminations are symmetrical. A simple analysis of the scattering matrix for this case reveals that the rest of the mechanical power incident from the left side of the beam is equally reflected back (25%) and transmitted (25%) to the other side of the patch. In order to enhance harvesting further, lumped obstacles are introduced in the transmitted wave domain creating a standing wave pattern. In the case of power enhancement method with spatially localization of a lumped obstacle, the harvested power is almost doubled by properly locating the obstacle with respect to the harvester and the maximum efficiency of 95% is obtained under resistive-inductive loading. Additionally, a multifunctional piezoelectric energy harvester anechoic boundary condition is proposed, in which nearly all the energy in a propagating bending wave can be extracted using piezoelectric patches at the free end of a beam.

The validity and application of the proposed model and the performance enhancement methods are demonstrated with several experimental studies by using piezoelectric patches bonded to a long slender beam. The experimental and theoretical results are compared through transient and power analyses and an excellent agreement is observed when the

losses in the system (i.e. internal resistance of the inductance box, mechanical loss in the system and the dielectric losses in the harvester) are included in the electroelastic model. In contrast with the ideal simulation case results leading to ideal harvester efficiencies, lower figures are obtained due to losses in real structure. Harvester efficiency decreases to 26% for resistive-inductive loading and 45% efficiency is obtained with the lumped mass addition. On the other hand, in the anechoic boundary condition experiments, a 6% power reflection ratio is obtained, resulting in quasi-anechoic behavior, which is very promising for achieving an energy-harvesting boundary condition that minimizes the reflections. It should be noted that these enhancement methods are most effective and practical when piezoelectric patch lengths and obstacle to patch distances are $\sim > \lambda/4$, where evanescent fields become insignificant, while the model can readily accommodate the presence of evanescent waves for arbitrary patch lengths.

6.1.2 Enhanced Elastic Wave Harvesting Through Wave Focusing Concepts

6.1.2.1 A SEM-based Piezoelectric Harvester

In order to enhance elastic wave energy in two-dimensional structures, i.e. plates, this study provides novel concepts for spatial localization or focusing wave energy by tailoring the reflective and refractive properties of elastic plates. To this extend, first, flat elastic mirrors (a.k.a. SEM) are explored with structurally-embedded reflectors which are formed by inserting metallic spheres (e.g. tungsten, lead, steel) into blind holes in a flat aluminum plate domain. The basic relationship between the mirror geometry and wavelength of the lowest asymmetric Lamb wave mode (A_0 mode) in a plate is unveiled with respect to formation and minimization of the near side lobes observed in earlier work [9, 10, 11]. The design criterion is proposed such that the ideal elastic wave mirror with the minimal (or negligible) side lobes should have $d \sim \lambda$ (roughly $d = \lambda \pm 0.1\lambda$) where d is the distance between the focus and edge of the mirror. It is tested and supported by simulations on both elliptical and parabolic mirrors designed with a range of d values. This criterion has a direct impact on the harvester design as a smaller piezoelectric patch with a single electrode can be used instead of a larger transducer with a complex harvester/electrode pattern and wiring [11]. Next, the

dynamics of the structurally-embedded reflectors are investigated in detail through finite-element simulations with a focus on the frequency dependence of reflection coefficient for spherical inclusions of tungsten, lead, and steel in aluminum. It is observed that, at very low frequencies, the reflection coefficient is very low since the wavelength is much larger than the inclusion size and the trends in the reflection coefficient with increased frequency is not monotonic with almost zero reflection (or perfect wave transmission compatible with the flexural nature of the A_0 mode Lamb wave) at the transmission resonances of the inclusions. Avoiding transmission resonances for SEM implementation as the mirror reflection is poor, design frequency is set where the reflection coefficient is highest (dominated by mass effect of inclusions). Through time-dependent simulations on geometrically identical SEM configurations made from spherical tungsten, lead, and steel inclusions, it is observed that the peak amplitude at focus scales linearly with the mass density of the inclusion, which in turn is proportional to the reflection coefficient at the design frequency (50 kHz). Then, simulations are validated with experiments performed on an elliptical SEM using tungsten inclusions. The energy harvesting performance enhancement associated with the SEM concept is explored by identical half-wavelength piezoelectric energy harvester disks bonded at the focus of the SEM and also in a baseline setting at the same distance from the excitation source in the uniform plate region. Under the same excitation applied to both harvesters, the harvested power is increased by an order of magnitude (∼11 times) by focusing the elastic waves in the SEM domain as compared to the baseline case of harvesting incident plane waves using an identical piezoelectric disk. The order of magnitude increase in the power output via SEM is also confirmed numerically by comparing RMS wave intensity in the respective SEM finite-element simulation with the wave field simulation for the baseline flat plate at the same distance from the source. The square of the RMS wave intensity at the harvester location is found to be ∼11 times that of the baseline case, in excellent agreement with the results of energy harvesting experiments. Finally, an intriguing mirror concept is addressed with a perforated mirror scenario (mass subtraction rather than inclusion) via through holes resulting in a low-frequency wave focusing (15 kHz). However, the reflection coefficient resulting from the through hole is rather low; as a result, a perforated mirror

made using through holes yields much lower intensity (at the focus point). It is concluded that there will always be a gain in the presence of a properly designed mirror setting (as compared to the baseline case of a flat plate); however, the gain strongly depends on the reflection coefficient of the inclusion. Therefore, it is suggested that a more plausible way to enable low-frequency mirrors could be to exploit bandgap formation via locally resonant metamaterials which is also discussed in this work.

6.1.2.2   PC-lens-based Piezoelectric Harvesters

As an alternative to wave focusing and enhanced energy harvesting with elastic mirrors, elastic lenses can be implemented to focus the plane wave energy at a desired spot by tailoring wave propagation characteristics. These lenses are based on a gradient distribution of the refractive index of the unit cells forming the lens domain. In this context, a Gradient-Index Phononic Crystal Lens (GRIN-PCL), a 3D printed GRIN-PCL, and an omnidirectional Luneburg lens are studied with the PC unit cells. First, the GRIN-PCL is designed with a blind hole square unit cell structure which can be more advantageous as compared to complete perforation and external stubs in practical applications since mass addition (GRIN-PCLs with stub attachments) is avoided while structural integrity (perforated GRIN-PCLs with through holes) is better preserved. The orientation and the hole sizes in the unit cells are tailored according to the hyperbolic secant gradient distribution which results in plane waves travelling faster at the edges and slower in the center, hence converging at the focal point of the GRIN-PCL. Focusing of the A_0 Lamb wave mode in an aluminum plate is numerically shown with finite element simulations which agrees well with the phenomena expected for GRIN-PCL. In addition, the focal points agree with the beam trajectory results obtained from the analytical solution of the ray trajectory in a waveguide. Experimental measurements from the fabricated GRIN-PCL structure reveals and excellent agreement with the beam trajectory predictions and the numerical elastic wave simulations at the target frequency. Also, Furthermore, broadband behavior of the GRIN-PCL is tested under different excitation frequencies. While the GRIN-PCL demonstrates a good broadband focusing capability, it is observed that the focusing neck becomes

longer and the focal points shift away from the source as the excitation frequency decreases due to the sensitivity of the gradient coefficient to frequency. It is shown that the gradient coefficient decreases/increases for frequencies lower/higher than the designed one resulting in a larger/smaller focal distance. Then, the GRIN-PCL is coupled with a half-wavelength piezoelectric disc for performance enhancement in structure-borne elastic energy harvesting from the A_0 mode Lamb waves originating from a line source. Since the reflections from the GRIN-PCL domain are very small (7%) the incident field is focused to the harvester without significant loss. As compared with a baseline case of harvesting incident plane waves using an identical piezoelectric disk as the harvester on the pure plate domain, under the same excitation applied to both harvesters, the efficiency is dramatically increased by 13 times by focusing the elastic waves in the GRIN-PCL.

In the second GRIN-PCL concept, 3D printing is utilized to make more practical lens designs avoiding major structural changes in the host plate while providing cost effective solutions to wave focusing hence enhanced energy harvesting. A bilayer unit cell design consisting of an aluminum plate layer and 3D printed stubbed layer is employed and the gradient distribution is obtained by different stub heights. Through numerical simulations flexural wave focusing is achieved with a focal point at 20.6a, which is slightly larger than the beam trajectory results at 17.6a which can be due to the diffraction effects not completely modeled by analytical ray tracing. With the 3D printed GRIN-PCL the RMS intensity of the sum of the velocity field centered in the focal point within a half-wavelength sized circular region is calculated to be 1.7 times larger than the RMS intensity of the sum of the incident wave velocity in a similar area on the pure plate domain. Furthermore, different lens designs are explored in terms of controlling the focal distance and aperture size at the same design frequency (using the same materials) and their effect on the wave focusing performance of the GRIN-PCL are examined. When the lens aperture is kept constant it is observed that the focusing neck and thickness increases as the focal depth increases while similar wave focusing amplitudes are obtained in terms of the RMS wave field comparisons. In another case study, two GRIN-PCLs with different aperture sizes (11 and 15 unit cells wide) are designed while keeping the same gradient coefficient hence same focal depth.

The focusing intensity increases as the as the aperture size increases. Due to the larger aperture, the focus neck and thickness decreases which results in a better agreement in terms of predicting the focal depth with the analytical beam solution. Hence, it is concluded that in order to have short focus necks and better wave focusing performance, the wider lenses should be preferred. Then, 3D printed lens layer is fabricated and bonded to the aluminum host structure with vacuum curing technique. In the experiments, wave focusing is clearly observed in the lens domain, however the experimental wave field obtained at 40 kHz (design frequency) does not exactly match with the finite element simulations at that frequency (it rather agrees with 55 kHz) which is attributed due to the imperfections in the experimental setup including the fabrication errors such as material, resolution, minimum layer thickness, epoxy bonding layer, etc. Through resistive sweep experiments, 3D printed GRIN-PCL integrated with piezoelectric energy harvester results in enhanced structure-borne wave energy harvesting by boosting the harvested power nearly 3 times as compared to a baseline harvester.

Although, the GRIN-PC lenses is an extremely effective design for focusing propagating flexural waves (A0 mode Lamb wave), its performance is very susceptible and sensitive to the orientation of the incident plane wave. In the final PC lens concept, a Luneburg lens is designed, fabricated and numerically and experimentally validated to alleviate the directivity issue with its omnidirectional wave focusing capability. Hexagonal blind-holed unit cell design is chosen due to its uniform distribution in the circular lens domain. An axisymmetric gradient index distribution is employed in the Luneburg lens design by varying the hole size. Under plane wave excitation from line sources at 0° and 30° incident angles, wave focusing is observed at the opposite border of the lens with respect to the incoming wave direction in the numerical simulation. In addition, similar focusing performance is achieved even for the worst incidence angle (considered as 30°representing incidence from the corner of the hexagonal cells), demonstrating that the desired omnidirectional characteristics is achieved. Then, omnidirectionality of the Luneburg lens is tested and validated under the excitation of two plane wave sources at 0° and 30° incident angles which shows an excellent agreement between the wavefields from the simulations and experiments. Finally,

Luneburg lens-based elastic wave energy harvesters are tested and 13.1 times increase in the efficiency is obtained by focusing the elastic waves in the Luneburg lens as compared the baseline case of harvesting. In addition, the 30° harvester yields comparable power levels to the 0° harvester experimentally validating the omnidirectional plane wave energy harvesting concept. Hence, it is concluded that the omnidirectional focusing capability of the Luneburg lens can potentially alleviate the directional sensitivity of existing focusing concepts for enhanced elastic wave energy harvesting by locating multiple energy harvesters over the periphery of the lens domain with separately processed and rectified outputs.

6.1.2.3 LR-based Elastic Lens and Mirror

The GRIN lenses designed with the PC unit cells presented in this work targets flexural wave focusing at 50 kHz merely to demonstrate and validate the concept using a GRIN-PCL setup with compact dimensions and is not intended for a specific application. As is common practice in energy harvesting, the design frequency (and therefore the resulting GRIN-PCL dimensions) would be dictated by the given excitation spectrum. For instance, in low frequency energy harvesting applications (less than kHz) the PC-based designs would yield very high dimensions due to the frequency dependency of the PC unit cells. On the other hand, LR structures provides the ability to engineer their operation frequency by tuning the resonance of the structural features of the LR unit cells. Hence, novel lens designs with LR structures are explored to potentially eliminate the need to scale up the whole structure (as compared to PC structures). With the LR approach, the dispersion characteristics (and thereby the phase velocity distribution) is altered at much lower frequencies ($\sim hundreds Hz$) right below the local resonance frequency. The stiffness and mass of the resonators are varied proportionally, so that the bandgap formation is obtained around the same target frequency for all unit cells. Hence, the desired refractive index profile and flexural wave focusing is achieved at 400 Hz through numerical simulations. In other words, this work demonstrates wave focusing within the LR lens composed of subwavelength ($\sim \lambda/9$) periodic LR structures. Then, the bandgap formation of the LR unit cells are coupled with the elastic mirror concept to make a low-frequency LR mirror that operates in the bandgap

for plane wave focusing. LR unit cells are arranged in the form of a parabola by applying the geometry-wavelength criterion proposed in this work and the LR mirror is numerically simulated. With three rows of LR cells having a very high reflection coefficient value of 0.94, plane wave focusing is successfully demonstrated at 350 Hz. On the other hand, a single row of parabolic mirror is also able to focus elastic waves due to the impedance mismatch.

6.2   Contributions

The following highlights from this dissertation summarize the major contributions to the state of art:

- Development of fully coupled electoelastic models based on wave propagation approach to energy harvesting problem which enables the possibility of extracting the maximum electrical power in propagating wave scenarios including transient excitations and offers an insight that is otherwise not easily available in standing wave or modal vibration methods (Chapter 2);

- Exploration of wavelength matching, resistive and resistive-inductive circuits, and performance enhancement with spatially localized obstacles in one-dimensional bending wave energy harvesting problem (Chapter 2);

- Creation of a multi-functional energy harvester at the free end boundary of the beam resulting in an anechoic boundary condition (i.e. an energy-harvesting boundary condition that minimizes the reflections) (Chapter 2);

- Development and experimental validation of elastic mirror-based energy harvesters beyond heuristic designs that avoid substantial modification of the host structure and complex segmented harvesters hence enabling harvester design as a smaller piezoelectric patch with a single electrode (Chapter 3);

- Rigorous effort in understanding of the elastic wave focusing performance of the mirror geometry as well as the dynamics of the structurally-embedded reflectors from reflection point of view (Chapter 3);

- An elastic mirror design methodology unveiling the relation between the wavelength and geometry with respect to formation and minimization of the side lobes which is applicable to both parabolic and elastic mirrors (Chapter 3);

- Demonstration of a low frequency (compared to SEM) wave focusing concept using perforated mirrors with through holes (mass subtraction rather than inclusion) (Chapter 3);

- Design, fabrication, numerical and experimental validation of PC-based gradient index lenses (GRIN-PCL, 3D printed GRIN-PCL and Luneburg lens) for focusing plane waves in the form of lowest asymmetric (A_0 mode) Lamb waves and enhancement of energy harvesting with the first PC lens-based piezoelectric harvesters (Chapter 4);

- Experimental proof-of-concept of the broadband wave focusing in the GRIN-PCL domain and its theoretical roots (Chapter 4);

- Low reflection GRIN-PCL with a novel blind-hole unit cell design resulting in high focusing and an order of magnitude increase in harvested power (Chapter 4);

- A 3D printed GRIN-PCL for the ease of wave focusing and harvesting applications (Chapter 4);

- Exploration of the effect of aperture size and focal distance on the performance of GRIN-PCL wave focusing (Chapter 4);

- An omnidirectional lens (a.k.a. the Luneburg lens) for achieving the direction independent wave focusing enabling omnidirectional enhanced energy harvesting (Chapter 4);

- Design methodology and numerical proof-of-concept for GRIN lenses with LR unit cells towards enabling low frequency energy harvesting ($\sim hundredHz$) (Chapter 5);

- Demonstration of wave focusing within the LR lens composed of subwavelength($\sim \lambda/9$) LR periodic structures (Chapter 5);

- Envisioned fabrication of the LR lens with the pillar-mass type unit cells through 3D printing and mass addition (Chapter 5);

- Numerical proof-of-concept of the low frequency wave focusing through bandgap-based elastic mirrors formed by an array of LR structures (Chapter 5).

6.3 Future Work

The present study for harvesting of structure-borne propagating waves explored electroelastic dynamics of bending waves in an infinite and semi-infinite beams shunted to an AC circuit with linear resistive and reactive components for linear impedance matching. Future work may investigate nonlinear energy harvesting circuits with standard AC-DC conversion, switching circuits for boosted power output in case of weak electromechanical coupling, as well as nonlinear impedance matching circuits. In addition, the end boundary harvesting can be further studied for realizing anechoic boundary condition in wave propagation experiments where the boundary reflections are usually undesired. Furthermore, one-dimensional bending wave harvesting can be explored in a metamaterial setting and the bandgap generation can be exploited along with energy harvesting. Finally, extension of this electroelastic model to two-dimensional structures would be a decent effort to fill this gap in literature which have often been overlooked.

This study implements concepts inspired from optics (GRIN lenses) and antenna (mirrors) theory in elastic wave focusing for enhancing the harvested power from structure-borne propagating waves. Other than the structurally-embedded reflectors (Chapter 3), different designs can be developed yielding a better reflection coefficient hence better focusing performance. Although a design methodology is provided for reduced side lobes, the effect of geometrical parameters (such as aperture size, mirror depth) can be further investigated for optimized elastic mirrors at desired frequencies.

In terms of PC-based lenses a solid understanding is required for optimization of the performance in addition to an uncertainty quantification for the fabrication errors in the geometry and the orientation of the PC structures. Also, investigation of mode conversion on the focusing performance can be another aspect of a future work. Furthermore, with a high

precision 3D fabrication process (and different materials), the 3D GRIN-PCL performance can be enhanced and a piezoelectric energy harvester can be integrated within the lens itself.

As presented in Chapter 4 omnidirectional focusing capability of the Luneburg lens can potentially alleviate the directional sensitivity of existing focusing concepts for enhanced elastic wave energy harvesting. This can be further investigated by locating multiple energy harvesters over the periphery of the lens domain with separately processed and rectified outputs. In addition, the broadband focusing and harvesting capability of the Luneburg lens can be explored.

In order to enable low frequency flexural wave harvesting, LR-based lens concepts proposed in this work can be experimentally validated with the design parameters provided in Chapter 5.

Appendix A

EQUIVALENT REPRESENTATION OF THE SERIES CONNECTION OF PIEZOCERAMIC LAYERS FOR ONE-DIMENSIONAL BENDING WAVE HARVESTING
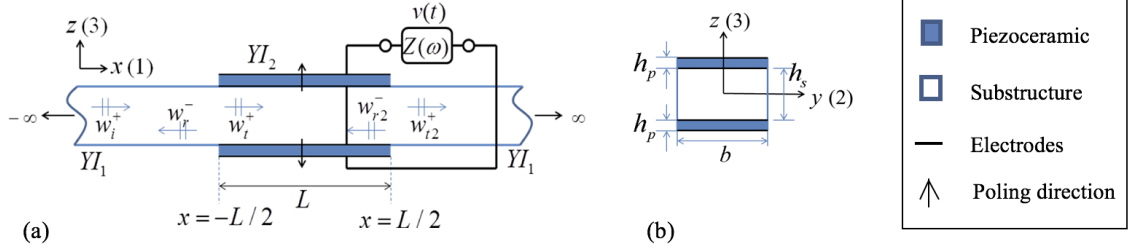
Figure 66: Incident, reflected, and transmitted waves at discontinuities: (a) Series connection and (b) composite cross-section in the harvester region.

In the series connection case, the voltage across the electrodes of each piezoceramic layer is $v(t)/2$ [25]. And due to opposite poling in the series connection, the instantaneous electric fields are in the same direction (i.e., $E_3(t) = -v(t)/2h_p$ for both layers). Substituting Equations 7 into Equation 6, the backward coupling term in Equation 26 is obtained.

$$\chi = \frac{b\bar{e}_{31}}{2h_p}\left[\left(hp + \frac{h_s}{2}\right)^2 - \left(\frac{hs}{2}\right)^2\right] = b\bar{e}_{31}h_{pc} \tag{26}$$

The equivalent capacitance of two identical capacitors $(\bar{\varepsilon}_{33}^S bL/h_p)$ connected in series is

$$C_p^{eq} = \bar{\varepsilon}_{33}^S bL/2h_p \tag{27}$$

Then, it is substituted into the electrical circuit equation given in Equation 12. The expression of the dependent current source for the series connection is

$$i_p(t) = I_p e^{j\omega t} = -\bar{e}_{31}h_{pc}b \int_{-L/2}^{L/2} \frac{\partial^3 w_2(x,t)}{\partial x^2 \partial t} dx \tag{28}$$

and the amplitude of the current in Equation 28 can be obtained as $I_p = -j\omega\kappa$ with κ

95

being the forward coupling term, which is

$$\kappa = 2k_{b2}\bar{e}_{31}h_{pc}b\left[-(C_1 + D_1)sin\left(k_{b2}\frac{L}{2}\right) + (C_2 + D_2)sinh\left(k_{b2}\frac{L}{2}\right)\right] \qquad (29)$$

Note that, series connection is preferred for large voltage output, whereas parallel connection is preferred for large current output [25]. Both series and parallel connection configurations yield the same power output levels under optimal loading conditions which differ due to different equivalent capacitances of the two configurations. In this study, the focus is on the harvested power and the piezoelectric patches are connected in parallel in the experiments. However, we provide both configurations for the completeness of the study.

REFERENCES

[1] AKAYDIN, H., ELVIN, N., and ANDREOPOULOS, Y., "Wake of a cylinder: a paradigm for energy harvesting with piezoelectric materials," *Experiments in Fluids*, vol. 49, no. 1, pp. 291–304, 2010.

[2] ALLEN, J. and SMITS, A., "Energy harvesting eel," *Journal of fluids and structures*, vol. 15, no. 3-4, pp. 629–640, 2001.

[3] ANTON, S., ERTURK, A., and INMAN, D., "Multifunctional self-charging structures using piezoceramics and thin-film batteries," *Smart materials and Structures*, vol. 19, no. 11, p. 115021, 2010.

[4] ANTON, S. R. and SODANO, H. A., "A review of power harvesting using piezoelectric materials (2003–2006)," *Smart materials and Structures*, vol. 16, no. 3, p. R1, 2007.

[5] AULD, B. A., *Acoustic fields and waves in solids.* , 1973.

[6] AURELI, M., PRINCE, C., PORFIRI, M., and PETERSON, S. D., "Energy harvesting from base excitation of ionic polymer metal composites in fluid environments," *Smart materials and Structures*, vol. 19, no. 1, p. 015003, 2009.

[7] BIBO, A. and DAQAQ, M. F., "Energy harvesting under combined aerodynamic and base excitations," *Journal of sound and vibration*, vol. 332, no. 20, pp. 5086–5102, 2013.

[8] BRYANT, M. and GARCIA, E., "Modeling and testing of a novel aeroelastic flutter energy harvester," *Journal of vibration and acoustics*, vol. 133, no. 1, p. 011010, 2011.

[9] CARRARA, M., CACAN, M., LEAMY, M., RUZZENE, M., and ERTURK, A., "Dramatic enhancement of structure-borne wave energy harvesting using an elliptical acoustic mirror," *Applied Physics Letters*, vol. 100, no. 20, p. 204105, 2012.

[10] CARRARA, M., CACAN, M., TOUSSAINT, J., LEAMY, M., RUZZENE, M., and ERTURK, A., "Metamaterial-inspired structures and concepts for elastoacoustic wave energy harvesting," *Smart Materials and Structures*, vol. 22, no. 6, p. 065004, 2013.

[11] CARRARA, M., KULPE, J., LEADENHAM, S., LEAMY, M., and ERTURK, A., "Fourier transform-based design of a patterned piezoelectric energy harvester integrated with an elastoacoustic mirror," *Applied Physics Letters*, vol. 106, no. 1, p. 013907, 2015.

[12] CHEN, Z., GUO, B., YANG, Y., and CHENG, C., "Metamaterials-based enhanced energy harvesting: A review," *Physica B: Condensed Matter*, vol. 438, pp. 1–8, 2014.

[13] CHEN, Z., YANG, Y., LU, Z., and LUO, Y., "Broadband characteristics of vibration energy harvesting using one-dimensional phononic piezoelectric cantilever beams," *Physica B: Condensed Matter*, vol. 410, pp. 5–12, 2013.

[14] CHIU, W., GALEA, S., KOSS, L., and RAJIC, N., "Damage detection in bonded repairs using piezoceramics," *Smart materials and Structures*, vol. 9, no. 4, p. 466, 2000.

[15] CLIMENTE, A., TORRENT, D., and SÁNCHEZ-DEHESA, J., "Gradient index lenses for flexural waves based on thickness variations," *Applied Physics Letters*, vol. 105, no. 6, p. 064101, 2014.

[16] COOK-CHENNAULT, K., THAMBI, N., and SASTRY, A., "Powering mems portable devicesa review of non-regenerative and regenerative power supply systems with special emphasis on piezoelectric energy harvesting systems," *Smart Materials and Structures*, vol. 17, no. 4, p. 043001, 2008.

[17] DE MARQUI, C., VIEIRA, W. G., ERTURK, A., and INMAN, D. J., "Modeling and analysis of piezoelectric energy harvesting from aeroelastic vibrations using the doublet-lattice method," *Journal of Vibration and Acoustics*, vol. 133, no. 1, p. 011003, 2011.

[18] DEYMIER, P. A., *Acoustic metamaterials and phononic crystals*, vol. 173. Springer Science & Business Media, 2013.

[19] DOARÉ, O. and MICHELIN, S., "Piezoelectric coupling in energy-harvesting fluttering flexible plates: linear stability analysis and conversion efficiency," *Journal of Fluids and Structures*, vol. 27, no. 8, pp. 1357–1375, 2011.

[20] DUNNMON, J., STANTON, S., MANN, B., and DOWELL, E., "Power extraction from aeroelastic limit cycle oscillations," *Journal of Fluids and Structures*, vol. 27, no. 8, pp. 1182–1198, 2011.

[21] ELVIN, N. and ERTURK, A., *Advances in energy harvesting methods*. Springer Science & Business Media, 2013.

[22] ERTURK, A. and INMAN, D. J., "An experimentally validated bimorph cantilever model for piezoelectric energy harvesting from base excitations," *Smart materials and structures*, vol. 18, no. 2, p. 025009, 2009.

[23] ERTURK, A. and INMAN, D., "Broadband piezoelectric power generation on high-energy orbits of the bistable duffing oscillator with electromechanical coupling," *Journal of Sound and Vibration*, vol. 330, no. 10, pp. 2339–2353, 2011.

[24] ERTURK, A. and DELPORTE, G., "Underwater thrust and power generation using flexible piezoelectric composites: an experimental investigation toward self-powered swimmer-sensor platforms," *Smart materials and Structures*, vol. 20, no. 12, p. 125013, 2011.

[25] ERTURK, A. and INMAN, D. J., *Piezoelectric energy harvesting*. John Wiley & Sons, 2011.

[26] ERTURK, A., VIEIRA, W., DE MARQUI JR, C., and INMAN, D., "On the energy harvesting potential of piezoaeroelastic systems," *Applied Physics Letters*, vol. 96, no. 18, p. 184103, 2010.

[27] FAHY, F. J. and GARDONIO, P., *Sound and structural vibration: radiation, transmission and response.* Academic press, 2007.

[28] GIURGIUTIU, V., "Tuned lamb wave excitation and detection with piezoelectric wafer active sensors for structural health monitoring," *Journal of intelligent material systems and structures*, vol. 16, no. 4, pp. 291–305, 2005.

[29] GIURGIUTIU, V., *Structural health monitoring: with piezoelectric wafer active sensors.* Academic Press, 2007.

[30] GIURGIUTIU, V. and ROGERS, C. A., "Recent advancements in the electromechanical (e/m) impedance method for structural health monitoring and nde," in *5th Annual International Symposium on Smart Structures and Materials*, pp. 536–547, International Society for Optics and Photonics, 1998.

[31] GIURGIUTIU, V. and ZAGRAI, A. N., "Characterization of piezoelectric wafer active sensors," *Journal of Intelligent Material Systems and Structures*, vol. 11, no. 12, pp. 959–976, 2000.

[32] GLYNNE-JONES, P., TUDOR, M. J., BEEBY, S. P., and WHITE, N. M., "An electromagnetic, vibration-powered generator for intelligent sensor systems," *Sensors and Actuators A: Physical*, vol. 110, no. 1, pp. 344–349, 2004.

[33] GONELLA, S., TO, A. C., and LIU, W. K., "Interplay between phononic bandgaps and piezoelectric microstructures for energy harvesting," *Journal of the Mechanics and Physics of Solids*, vol. 57, no. 3, pp. 621–633, 2009.

[34] GRAFF, K. F., *Wave motion in elastic solids.* Courier Corporation, 2012.

[35] GUYOMAR, D., BADEL, A., LEFEUVRE, E., and RICHARD, C., "Toward energy harvesting using active materials and conversion improvement by nonlinear processing," *IEEE transactions on ultrasonics, ferroelectrics, and frequency control*, vol. 52, no. 4, pp. 584–595, 2005.

[36] HAGOOD, N. W. and VON FLOTOW, A., "Damping of structural vibrations with piezoelectric materials and passive electrical networks," *Journal of Sound and Vibration*, vol. 146, no. 2, pp. 243–268, 1991.

[37] HOROWITZ, S. B., SHEPLAK, M., CATTAFESTA III, L. N., and NISHIDA, T., "A mems acoustic energy harvester," *Journal of Micromechanics and Microengineering*, vol. 16, no. 9, p. S174, 2006.

[38] HSU, J.-C. and WU, T.-T., "Lamb waves in binary locally resonant phononic plates with two-dimensional lattices," *Applied physics letters*, vol. 90, no. 20, p. 201904, 2007.

[39] JIANG, S., LI, X., GUO, S., HU, Y., YANG, J., and JIANG, Q., "Performance of a piezoelectric bimorph for scavenging vibration energy," *Smart Materials and Structures*, vol. 14, no. 4, p. 769, 2005.

[40] JIN, Y., TORRENT, D., PENNEC, Y., PAN, Y., and DJAFARI-ROUHANI, B., "Simultaneous control of the s0 and a0 lamb modes by graded phononic crystal plates," *Journal of Applied Physics*, vol. 117, no. 24, p. 244904, 2015.

[41] KHELIF, A. and ADIBI, A., *Phononic Crystals: Fundamentals and Applications.* Springer, 2015.

[42] KINO, G. S., *Acoustic waves: devices, imaging, and analog signal processing.* Prentice Hall, 1987.

[43] KONG, N., HA, D. S., ERTURK, A., and INMAN, D. J., "Resistive impedance matching circuit for piezoelectric energy harvesting," *Journal of Intelligent Material Systems and Structures*, vol. 21, no. 13, pp. 1293–1302, 2010.

[44] KURT, H. and CITRIN, D. S., "Graded index photonic crystals," *Optics express*, vol. 15, no. 3, pp. 1240–1253, 2007.

[45] KWUIMY, C., LITAK, G., BOROWIEC, M., and NATARAJ, C., "Performance of a piezoelectric energy harvester driven by air flow," *Applied Physics Letters*, vol. 100, no. 2, p. 024103, 2012.

[46] LAUDE, V., *Phononic Crystals: Artificial Crystals for Sonic, Acoustic, and Elastic Waves*, vol. 26. Walter de Gruyter GmbH & Co KG, 2015.

[47] LI, B., LAVIAGE, A. J., YOU, J. H., and KIM, Y.-J., "Harvesting low-frequency acoustic energy using quarter-wavelength straight-tube acoustic resonator," *Applied Acoustics*, vol. 74, no. 11, pp. 1271–1278, 2013.

[48] LIANG, C., SUN, F., and ROGERS, C. A., "Electro-mechanical impedance modeling of active material systems," *Smart Materials and Structures*, vol. 5, no. 2, p. 171, 1996.

[49] LIN, S.-C. S., HUANG, T. J., SUN, J.-H., and WU, T.-T., "Gradient-index phononic crystals," *Physical Review B*, vol. 79, no. 9, p. 094302, 2009.

[50] LITAK, G., FRISWELL, M., and ADHIKARI, S., "Magnetopiezoelastic energy harvesting driven by random excitations," *Applied Physics Letters*, vol. 96, no. 21, p. 214103, 2010.

[51] LIU, F., PHIPPS, A., HOROWITZ, S., NGO, K., CATTAFESTA, L., NISHIDA, T., and SHEPLAK, M., "Acoustic energy harvesting using an electromechanical helmholtz resonator," *The Journal of the Acoustical Society of America*, vol. 123, no. 4, pp. 1983–1990, 2008.

[52] LIU, Z., ZHANG, X., MAO, Y., ZHU, Y., YANG, Z., CHAN, C. T., and SHENG, P., "Locally resonant sonic materials," *science*, vol. 289, no. 5485, pp. 1734–1736, 2000.

[53] LU, M.-H., FENG, L., and CHEN, Y.-F., "Phononic crystals and acoustic metamaterials," *Materials Today*, vol. 12, no. 12, pp. 34–42, 2009.

[54] LV, H., TIAN, X., WANG, M. Y., and LI, D., "Vibration energy harvesting using a phononic crystal with point defect states," *Applied Physics Letters*, vol. 102, no. 3, p. 034103, 2013.

[55] MACE, B., "Wave reflection and transmission in beams," *Journal of sound and vibration*, vol. 97, no. 2, pp. 237–246, 1984.

[56] MACE, B., "Power flow between two continuous one-dimensional subsystems: a wave solution," *Journal of Sound and Vibration*, vol. 154, no. 2, pp. 289–319, 1992.

[57] MARTINEZSALA, R., SANCHO, J., SÁNCHEZ, J. V., GÓMEZ, V., LLINARES, J., MESEGUER, F., and OTHERS, "Sound-attenuation by sculpture," *nature*, vol. 378, no. 6554, pp. 241–241, 1995.

[58] MIKOSHIBA, K., MANIMALA, J. M., and SUN, C., "Energy harvesting using an array of multifunctional resonators," *Journal of Intelligent Material Systems and Structures*, vol. 24, no. 2, pp. 168–179, 2013.

[59] MILLER, D. W. and VON FLOTOW, A., "A travelling wave approach to power flow in structural networks," *Journal of Sound and Vibration*, vol. 128, no. 1, pp. 145–162, 1989.

[60] MITCHESON, P. D., MIAO, P., STARK, B. H., YEATMAN, E., HOLMES, A., and GREEN, T., "Mems electrostatic micropower generator for low frequency operation," *Sensors and Actuators A: Physical*, vol. 115, no. 2, pp. 523–529, 2004.

[61] PAGE, J. H., SHENG, P., SCHRIEMER, H. P., JONES, I., and OTHERS, "Group velocity in strongly scattering media," *Science*, vol. 271, no. 5249, p. 634, 1996.

[62] PARK, G., FARRAR, C. R., DI SCALEA, F. L., and COCCIA, S., "Performance assessment and validation of piezoelectric active-sensors in structural health monitoring," *Smart Materials and Structures*, vol. 15, no. 6, p. 1673, 2006.

[63] PARK, G., SOHN, H., FARRAR, C. R., and INMAN, D. J., "Overview of piezoelectric impedance-based health monitoring and path forward," *Shock and Vibration Digest*, vol. 35, no. 6, pp. 451–463, 2003.

[64] POBERING, S., EBERMEYER, S., and SCHWESINGER, N., "Generation of electrical energy using short piezoelectric cantilevers in flowing media," in *SPIE Smart Structures and Materials+ Nondestructive Evaluation and Health Monitoring*, pp. 728807–728807, International Society for Optics and Photonics, 2009.

[65] POZAR, D. M., *Microwave engineering.* John Wiley & Sons, 2009.

[66] QI, S., OUDICH, M., LI, Y., and ASSOUAR, B., "Acoustic energy harvesting based on a planar acoustic metamaterial," *Applied Physics Letters*, vol. 108, no. 26, p. 263501, 2016.

[67] RAGHAVAN, A. and CESNIK, C. E., "Finite-dimensional piezoelectric transducer modeling for guided wave based structural health monitoring," *Smart materials and structures*, vol. 14, no. 6, p. 1448, 2005.

[68] RAMLAN, R., BRENNAN, M. J., MACE, B. R., and BURROW, S. G., "On the performance of a dual-mode non-linear vibration energy harvesting device," *Journal of intelligent material systems and structures*, vol. 23, no. 13, pp. 1423–1432, 2012.

[69] RAMLAN, R., BRENNAN, M., MACE, B., and KOVACIC, I., "Potential benefits of a non-linear stiffness in an energy harvesting device," *Nonlinear Dynamics*, vol. 59, no. 4, pp. 545–558, 2010.

[70] REINO, C. G., PÉREZ, M. V., and BAO, C., *Gradient-Index Optics: Fundamentals and Applicatioins*. Springer, 2002.

[71] RENNO, J. M., DAQAQ, M. F., and INMAN, D. J., "On the optimal energy harvesting from a vibration source," *Journal of sound and vibration*, vol. 320, no. 1, pp. 386–405, 2009.

[72] ROES, M. G., DUARTE, J. L., HENDRIX, M. A., and LOMONOVA, E. A., "Acoustic energy transfer: A review," *IEEE Transactions on Industrial Electronics*, vol. 60, no. 1, pp. 242–248, 2013.

[73] ROUNDY, S., WRIGHT, P. K., and RABAEY, J. M., *Energy scavenging for wireless sensor networks*. Springer, 2003.

[74] RUPP, C. J., DUNN, M. L., and MAUTE, K., "Switchable phononic wave filtering, guiding, harvesting, and actuating in polarization-patterned piezoelectric solids," *Applied Physics Letters*, vol. 96, no. 11, p. 111902, 2010.

[75] SÁNCHEZ-PÉREZ, J., CABALLERO, D., MARTINEZ-SALA, R., RUBIO, C., SÁNCHEZ-DEHESA, J., MESEGUER, F., LLINARES, J., and GÁLVEZ, F., "Sound attenuation by a two-dimensional array of rigid cylinders," *Physical Review Letters*, vol. 80, no. 24, p. 5325, 1998.

[76] SHAHAB, S., GRAY, M., and ERTURK, A., "Ultrasonic power transfer from a spherical acoustic wave source to a free-free piezoelectric receiver: Modeling and experiment," *Journal of Applied Physics*, vol. 117, no. 10, p. 104903, 2015.

[77] SHU, Y. and LIEN, I., "Analysis of power output for piezoelectric energy harvesting systems," *Smart materials and structures*, vol. 15, no. 6, p. 1499, 2006.

[78] SHU, Y., LIEN, I., and WU, W., "An improved analysis of the sshi interface in piezoelectric energy harvesting," *Smart Materials and Structures*, vol. 16, no. 6, p. 2253, 2007.

[79] SIGALAS, M. M. and ECONOMOU, E. N., "Elastic and acoustic wave band structure," *Journal of sound and vibration*, vol. 158, no. 2, pp. 377–382, 1992.

[80] SONG, H., LIM, H., and SOHN, H., "Electromechanical impedance measurement from large structures using a dual piezoelectric transducer," *Journal of Sound and Vibration*, vol. 332, no. 25, pp. 6580–6595, 2013.

[81] STANTON, S. C., MCGEHEE, C. C., and MANN, B. P., "Reversible hysteresis for broadband magnetopiezoelastic energy harvesting," *Applied Physics Letters*, vol. 95, no. 17, p. 174103, 2009.

[82] SUGINO, C., LEADENHAM, S., RUZZENE, M., and ERTURK, A., "On the mechanism of bandgap formation in locally resonant finite elastic metamaterials," *Journal of Applied Physics*, vol. 120, no. 13, p. 134501, 2016.

[83] SUKHOVICH, A., MERHEB, B., MURALIDHARAN, K., VASSEUR, J., PENNEC, Y., DEYMIER, P., and PAGE, J., "Experimental and theoretical evidence for sub-wavelength imaging in phononic crystals," *Physical review letters*, vol. 102, no. 15, p. 154301, 2009.

[84] TIWARI, R., KIM, K. J., and KIM, S.-M., "Ionic polymer-metal composite as energy harvesters," *Smart Structures and Systems*, vol. 4, no. 5, pp. 549–563, 2008.

[85] TOL, S., DEGERTEKIN, F., and ERTURK, A., "Modeling and enhancement of piezoelectric power extraction from one-dimensional bending waves," in *SPIE Smart Structures and Materials+ Nondestructive Evaluation and Health Monitoring*, pp. 90571C–90571C, International Society for Optics and Photonics, 2014.

[86] TOL, S., DEGERTEKIN, F., and ERTURK, A., "Gradient-index phononic crystal lens-based enhancement of elastic wave energy harvesting," *Applied Physics Letters*, vol. 109, no. 6, p. 063902, 2016.

[87] TOL, S., DEGERTEKIN, F., and ERTURK, A., "Piezoelectric power extraction from bending waves: Electroelastic modeling, experimental validation, and performance enhancement," *Wave Motion*, vol. 60, pp. 20–34, 2016.

[88] TOL, S., DEGERTEKIN, F., and ERTURK, A., "Omni-directional lens for structure-borne wave focusing and energy harvesting," in *SPIE Smart Structures and Materials+ Nondestructive Evaluation and Health Monitoring*, pp. 101641V–101641V, International Society for Optics and Photonics, 2017.

[89] TOL, S., XIA, Y., RUZZENE, M., and ERTURK, A., "Self-bending elastic waves and obstacle circumventing in wireless power transfer," *Applied Physics Letters*, vol. 110, no. 16, p. 163505, 2017.

[90] TOL, S., DEGERTEKIN, F. L., and ERTURK, A., "Harvesting of bending waves in one-dimensional infinite beams using resistive-reactive circuits," in *ASME 2013 Conference on Smart Materials, Adaptive Structures and Intelligent Systems*, pp. V002T07A015–V002T07A015, American Society of Mechanical Engineers, 2013.

[91] TOL, S., DEGERTEKIN, F. L., and ERTURK, A., "Dramatic enhancement of elastic wave energy harvesting using a gradient-index phononic crystal lens," in *ASME 2016 Conference on Smart Materials, Adaptive Structures and Intelligent Systems*, pp. V002T07A013–V002T07A013, American Society of Mechanical Engineers, 2016.

[92] TOL, S., DEGERTEKIN, F. L., and ERTURK, A., "3d-printed lens for structure-borne wave focusing and energy harvesting," in *SPIE Smart Structures and Materials+ Nondestructive Evaluation and Health Monitoring*, pp. 101641M–101641M, International Society for Optics and Photonics, 2017.

[93] TOL, S., VORA, F. T., DEGERTEKIN, F. L., and ERTURK, A., "Embedded elastic wave mirrors for enhanced energy harvesting," in *SENSORS, 2016 IEEE*, pp. 1–3, IEEE, 2016.

[94] TVEDT, L. G. W., NGUYEN, D. S., and HALVORSEN, E., "Nonlinear behavior of an electrostatic energy harvester under wide-and narrowband excitation," *Journal of Microelectromechanical systems*, vol. 19, no. 2, pp. 305–316, 2010.

[95] WANG, L. and YUAN, F., "Vibration energy harvesting by magnetostrictive material," *Smart Materials and Structures*, vol. 17, no. 4, p. 045009, 2008.

[96] WANG, W.-C., WU, L.-Y., CHEN, L.-W., and LIU, C.-M., "Acoustic energy harvesting by piezoelectric curved beams in the cavity of a sonic crystal," *Smart Materials and Structures*, vol. 19, no. 4, p. 045016, 2010.

[97] WILLIAMS, C. and YATES, R. B., "Analysis of a micro-electric generator for microsystems," *Sensors and Actuators A: Physical*, vol. 52, no. 1-3, pp. 8–11, 1996.

[98] WU, L.-Y., CHEN, L.-W., and LIU, C.-M., "Acoustic energy harvesting using resonant cavity of a sonic crystal," *Applied Physics Letters*, vol. 95, no. 1, p. 013506, 2009.

[99] WU, T.-T., CHEN, Y.-T., SUN, J.-H., LIN, S.-C. S., and HUANG, T. J., "Focusing of the lowest antisymmetric lamb wave in a gradient-index phononic crystal plate," *Applied Physics Letters*, vol. 98, no. 17, p. 171911, 2011.

[100] WU, T.-T., CHIOU, M.-J., LIN, Y.-C., and ONO, T., "Design and fabrication of a gradient-index phononic quartz plate lens," in *SPIE OPTO*, pp. 89940G–89940G, International Society for Optics and Photonics, 2014.

[101] YAN, X., ZHU, R., HUANG, G., and YUAN, F.-G., "Focusing guided waves using surface bonded elastic metamaterials," *Applied Physics Letters*, vol. 103, no. 12, p. 121901, 2013.

[102] YANG, A., LI, P., WEN, Y., LU, C., PENG, X., ZHANG, J., and HE, W., "Enhanced acoustic energy harvesting using coupled resonance structure of sonic crystal and helmholtz resonator," *Applied Physics Express*, vol. 6, no. 12, p. 127101, 2013.

[103] ZHAO, J., MARCHAL, R., BONELLO, B., and BOYKO, O., "Efficient focalization of antisymmetric lamb waves in gradient-index phononic crystal plates," *Applied Physics Letters*, vol. 101, no. 26, p. 261905, 2012.

[104] ZHU, J., CHRISTENSEN, J., JUNG, J., MARTIN-MORENO, L., YIN, X., FOK, L., ZHANG, X., and GARCIA-VIDAL, F., "A holey-structured metamaterial for acoustic deep-subwavelength imaging," *Nature physics*, vol. 7, no. 1, pp. 52–55, 2011.